Synthesis, Characterization and Application of Two-Dimensional Layered Metal Hydroxides for Environmental RemediationPurposes

Cleopas Machingauta
Marquette University

Recommended Citation

Machingauta, Cleopas, "Synthesis, Characterization and Application of Two-Dimensional Layered Metal Hydroxides for Environmental RemediationPurposes" (2013). *Dissertations (2009 -).* Paper 305.
http://epublications.marquette.edu/dissertations_mu/305

SYNTHESIS, CHARACTERIZATION AND APPLICATION OF TWO-DIMENSIONAL LAYERED METAL HYDROXIDES FOR ENVIRONMENTAL REMEDIATION PURPOSES.

by

Cleopas Machingauta

BSc (Hons) Chemistry, University of Zimbabwe, 2005

A Dissertation submitted to the Faculty of the Graduate School,

Marquette University,

In Partial Fulfillment of the Requirement for

the Degree of Doctor of Philosophy.

Milwaukee, Wisconsin

December, 2013

ABSTRACT
SYNTHESIS, CHARACTERIZATION AND APPLICATION OF TWO-DIMENSIONAL LAYERED METAL HYDROXIDES FOR ENVIRONMENTAL REMEDIATION PURPOSES.

Cleopas Machingauta, BSc Hons Chemistry.

Marquette University, 2013

Two-dimensional layered nano composites, which include layered double hydroxides (LDHs), hydroxy double salts (HDSs) and layered hydroxide salts (LHSs) are able to intercalate different molecular species within their gallery space. These materials have a tunable structural composition which has made them applicable as fire retardants, adsorbents, catalysts, catalyst support materials, and ion exchangers. Thermal treatment of these materials results in destruction of the layers and formation of mixed metal oxides (MMOs) and spinels. MMOs have the ability to adsorb anions from solution and may also regenerate layered structures through a phenomenon known as "memory effect".

Zinc-nickel hydroxy nitrate was used for the uptake of a series of halogenated acetates (HAs).HAs are pollutants introduced into water systems as by-products of water chlorination and pesticide degradation; their sequestration from water is thus crucial. Optimization of layered materials for controlled uptake requires an understanding of their ion-exchange kinetics and thermodynamics. Exchange kinetics of these anions was monitored using ex-situ PXRD, UV-vis, HPLC and FTIR. It was revealed that exchange rates and uptake efficiencies are related to electronic spatial extents and the charge on carboxyl-oxygen atoms.

In addition, acetate and nitrate-based HDSs were used to explore how altering the hydroxide layer affects uptake of acetate/nitrate ions. Changing the metal identities affects the interaction of the anions with the layers. From FTIR, we observed that nitrates coordinate in a D_3h and Cs/C_2v symmetry; the nitrates in D_3h symmetry were easily exchangeable. Interlayer hydrogen bonding was also revealed to be dependent on metal identity. Substituting divalent cations with trivalent cations produces materials with a higher charge density than HDSs and LHSs. A comparison of the uptake efficiency of zinc-aluminum, zinc-gallium and zinc-nickel hydroxy nitrates was performed using trichloro acetic acid as target anion. Uptake efficiency was better for LDHs than HDS, and between the LDHs, zinc-aluminum hydroxy nitrate was the best material for the uptake of tClAc.

Calcined LDHs were applied for the uptake of methyl-orange, model azo-dye. The ability to regenerate the layered structures was helpful for improving adsorption efficiency. It has been reveal that calcined LDHs are also better adsorbents than calcined HDSs.

ACKNOWLEDGEMENTS

Cleopas Machingauta, BSc Hons Chemistry

My sincere gratitude goes to my advisor, Prof Jeanne M. Hossenlopp, for her continuous support throughout this whole study. I will be forever grateful for the amount of time she sacrificed and the work she had to go through in order to make this work possible. Her scientific guidance and motivation is very much appreciated. I will also thank Prof. James Gardinier (dissertation committee member), for the time he served in my previous annual meetings and research meeting. He was helpful even after my defense; he treated me like his own student. Keep it up Dr. I also thank Prof. Chieu Tran, for the suggestions he gave during our meetings that helped shape this dissertation.

I would like to thank Prof. Charles Wilkie, who allowed me to freely use his thermal analysis instruments; the instruments were very crucial for all of my projects. My previous group members, Dr. Stephen Majoni, Ning Wang and Dr. Darlington Mlambo, helped a lot to make this work a success; we discussed our projects and we shared ideas. I will not forget a special former group member, Dr. Allen Chaparadza, for extra contributions he made towards my research and for his advice in science and social life.

This work has been made possible through the financial assistance we received from the National of Science Foundation. Lastly, I am grateful for my parents, who will not be there to see their dream come true. They showed me the way to go and I will forever be grateful.

TABLE OF CONTENTS

List of Tables

List of Figures

1. Layered 2-dimensional nano-composites: Synthesis, Application and Kinetic Modeling.

1.1 Introduction

Layered metal hydroxides have been known since the discovery of the mineral hydrotalcite (HT), more than 150 years ago.[1,2] The main structural features of HT($Mg_6Al_2(OH)_{16}CO_3.4H_2O$), were understood in the 1960s, after Allmann[3] and Taylor[4] carried out the pioneering single crystal X-ray diffraction (XRD) studies on the mineral. However, the finer details of the structure such as the extent of ordering of metal cations within the layers, the stacking arrangement of layers, the range of possible compositions and stoichiometry, anion arrangement and water molecules in the interlayer galleries are not well known and have been subject to some controversy in the literature.[5]

1.2 Basic structure and reactivity

Layered metal hydroxides have been classified, according to their structure, into layered double hydroxides (LDH), hydroxy double salts (HDS) and layered hydroxy salts (LHS). The basic structure of LDHs is related to that of brucite [$Mg(OH)_2$] which is of the CdI_2 type. This brucite structure consists of Mg cations located in the centre of edge sharing hydroxyl octahedra, forming infinite two dimensional layer structures (see Figure 1.1). The hydroxy groups are perpendicular to the plane of the layers and they lie on a triangular lattice.[6,7]The actual local geometry around the metal and the packing of hydroxyl anions are distorted away from the idealized spatial arrangement. The octahedra

are compressed along the stacking axis, making the geometry at the metal center D_{3d}

rather than the simplified O_h. The nature of forces holding the layers together has been

attributed to dispersion forces and hydrogen bonding.[8,9]
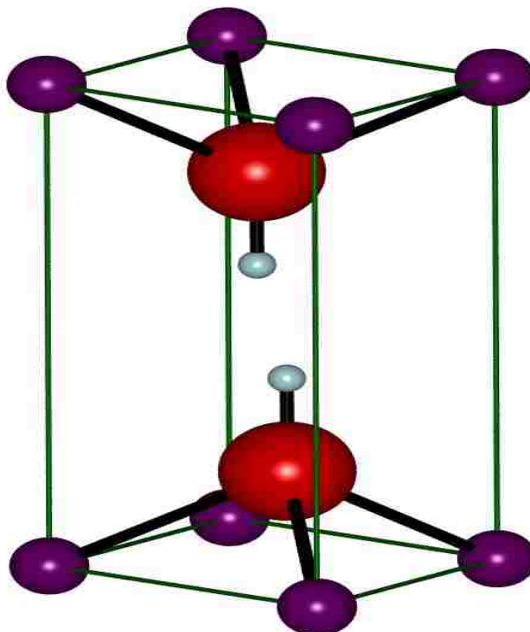
**Figure 1.1 A unit cell of brucite, with the smaller darker purple spheres being the
magnesium cations and the larger red spheres being the oxygen.**
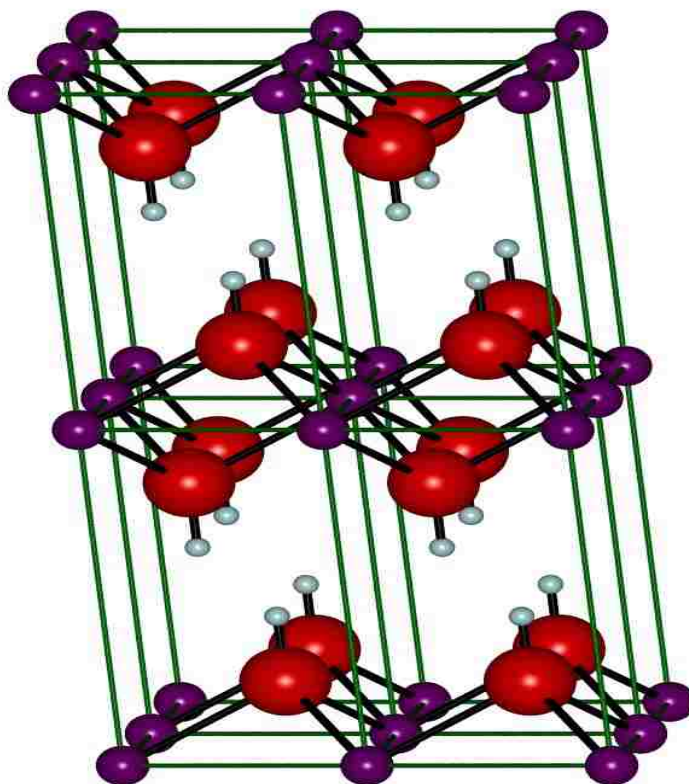
Figure 1.2. Eight edge sharing brucite crystal units.

Brucite layers are form when unit cells are joined together and shown above.
Hydroxyl groups, shown by the red and grey spheres, are perpendicularly above and
below the plane of the layers. In the structure shown above, one Mg atom that is shared
by all the unit cells but is octahedrally coordinated with 6 hydroxyl groups.

LHSs are composed of one divalent metal cation, hydroxyl groups and an anion;
they have a general formula $M(OH)_{2-y}A_y \cdot nH_2O$, where M can be Ni, Co, Cu and Zn.[10,11]
The structures of HDSs and LHSs have been classified into two structural types basing on

the structure of copper hydroxy nitrate ($Cu_2(OH)_3NO_3.H_2O$) and zinc hydroxy nitrate ($Zn_5(OH)_8(NO_3)_2.2H_2O$).
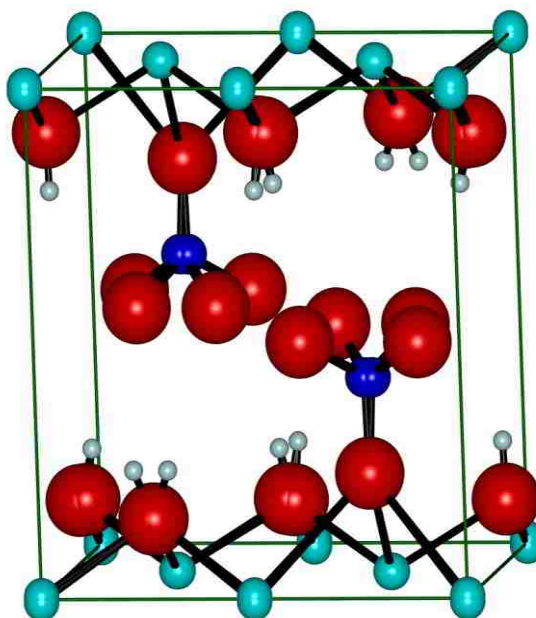
Figure 1.3. Two adjacent unit cells of $Cu_2(OH)_3NO_3$. The red spheres are O atoms, green spheres are copper atoms and the small grey spheres are hydrogen atoms.

Figure 1.3 shows the two adjacent unit cells of$Cu_2(OH)_3(NO_3)$.This structure is also similar to that of $Ni_2(OH)_3(NO_3)$ and $Mg_2(OH)_3NO_3$. In these compounds, the layers are not positively charged, instead, 25 % of the hydroxyl ions of the $M(OH)_2$ layers are replaced by NO_3^- ions that are coordinated to the metal centres.[12,13]The figure below is an enlarged part of figure 1.3.It can be observed that the N-O bond is conically shaped, instead of being cylindrical, which is characteristic of objects bound on one end while revolving around an axis. Because of this motion, the software used to process these

structures sees two extra oxygen atoms per nitrate. Two of the oxygen atoms are going

into the plane of the paper while the other two are coming out of the paper.
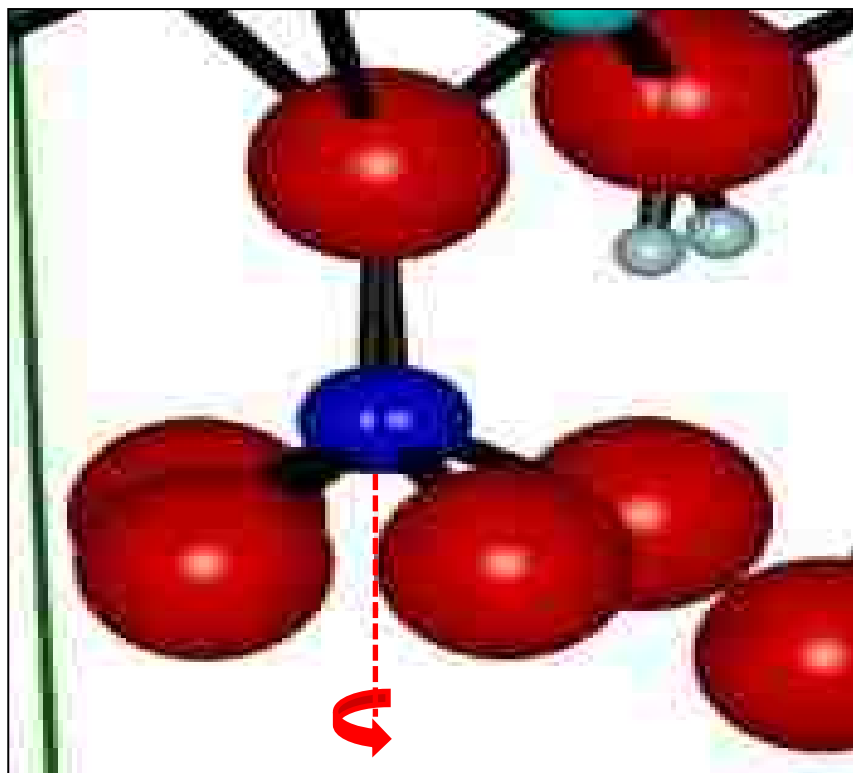
Figure 1.4. A nitrate revolving around an axis (shown by the red dashed line).

Cu^{2+} ions in CuHN, have been reported to be occupying two distinct

crystallographic sites (Cu1 and Cu2).[14]Cu1 ions are coordinated to four hydroxide ions in

equatorial positions and two nitrate ions in axial positions, while Cu2 ions are

coordinated to five hydroxide ions and a nitrate ion. The intralayer oxygen atoms are

tetrahedrally coordinated and they bind to three copper ions (μ_3-OH) and a hydrogen atom. The nitrate ions are also bound to three copper ions (μ_3-ONO$_2$)and are orientated perpendicular to the brucitic layers.[15]The CuHN layers are clearly represented in figure below.
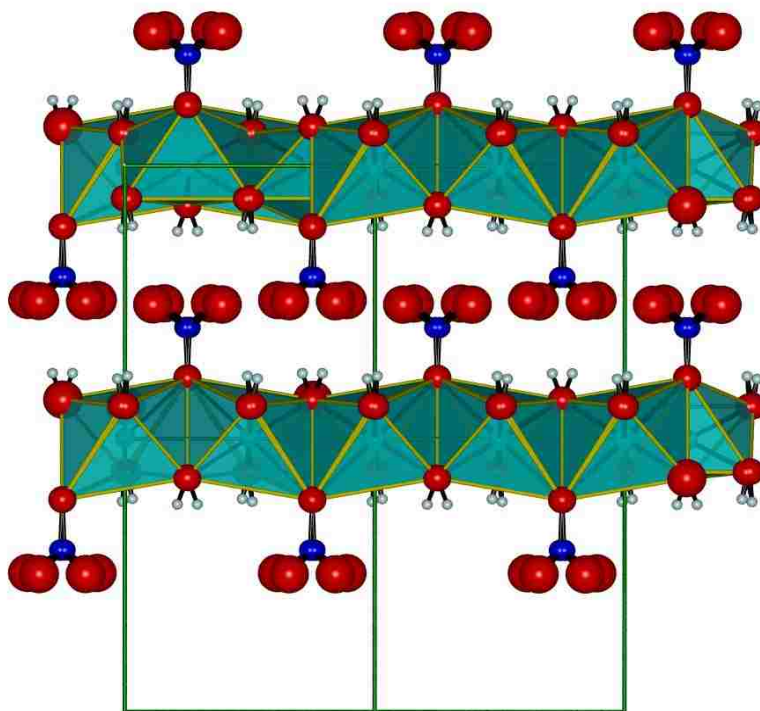
Figure 1.5. Two layers of CuHN, showing the polyhedral around copper atoms. As noted in the text, there is an artifact in the structure due to rotation around the N-O bound to the metal layer, leading to the appearance of having two additional oxygen atom positions in the nitrate group.

In $Zn_5(OH)_8(NO_3)_2.2H_2O$, one quarter of the octahedral sites are vacant and zinc cations occupy the tetrahedral sites above and below these vacant octahedral sites

resulting in layers positively charged.[16] The tetrahedral coordination of zinc cations is satisfied by three OH ions of the brucite layers and a water molecule. This net positive charge is compensated for by the incorporation of anions, in this case nitrates.[17] The structure of $Zn_5(OH)_8(NO_3)_2.2H_2O$ is related to zinc nickel-HDSs (zinc nickel hydroxy acetate and zinc nickel hydroxy nitrate) studied in this work.

The HDSs formula can be generalized as $[(Me^{II}_{1-x} M^{II}_{1+x})(OH)_{3(1-y)/n}] A^{n-}_{(1+3y)/n}.mH_2O$, where Me^{II} and M^{II} are different divalent metals, and A^{n-} is the counter ion.[18] The divalent metal ions can be Co, Cu, Zn, Mn, Ni, Mg, Cd and Fe while the anions, A^{n-}, can either be monovalent, for example, Cl^-, NO_3^-, or CH_3COO^-, or divalent. It was initially believed that the difference in ionic radii of the two metal cations which make up an HDS will be within 0.05 Å.[19] However, HDSs containing Cd^{2+} and Cu^{2+}, whose radii difference is about 0.22 Å, have been successfully prepared.[6] The relative composition of the ions in the metal hydroxide layers has been reported to be dependent on the method of synthesis and the nature of the metal ions.

Choy et al.[10] studied the intra- and inter-layer structures of zinc nickel hydroxy acetate (ZnNiHAc) prepared using hydrothermal and coprecipitation methods. They observed that upon drying, for ZnNiHAc prepared using the hydrothermal process, the orientation of the acetates change from chelating type to unidentate while no such changes were observed for coprecipitated ZnNiHAc.
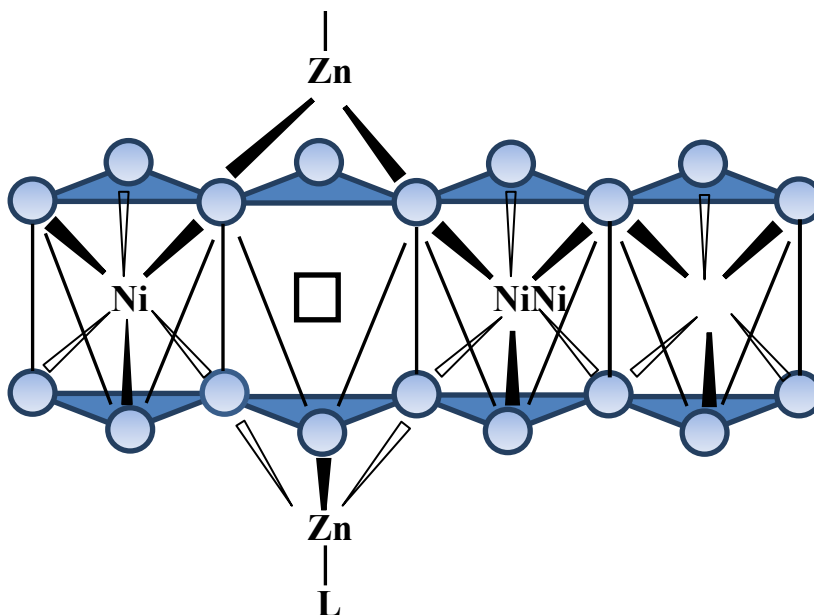
Figure 1.6. Representation of the intralayer structure of nickel and zinc hydroxy double salt. The rectangle (□) represents the vacant octahedral site and L is the anion.

Arulraj and coworkers[22] reported that Zn^{2+} occupies the tetrahedral sites while Ni^{2+} occupies the octahedral sites. In HDSs the existence of potentially exchangeable anions may be created by two mechanisms. In the first, a surplus layer charge is created by the occurrence of octahedral vacant sites that are capped above and below by two tetrahedrally coordinated divalent cations[23]. In the second, whilst there is complete occupancy of octahedral cationic positions, part of the framework hydroxyl groups are substituted by structure forming anions (e.g. NO_3^-)[24]. HDSs generally contain a certain amount of water between the layers, which can be driven out by heating[25]. According to Meyn and coworkers[26], Zinc nickel hydroxy nitrate (ZnNiHN) changed from 9.8 Å to 8.9 Å after drying, due to loss of water.

HDSs have also been characterized as rigid. As a result of their high layer rigidity and structural anisotropy, they exhibit a number of physical properties and structural phenomena of both fundamental and practical interest. Furthermore, this layer rigidity has made it possible to synthesize pillared layered compounds.[20] In pillared clays, robust widely spaced polyatomic guest ions prop them apart, creating larger areas of empty intra-gallery space available for catalytic activity and molecular sieving. The intralayer rigidity makes it easy for the layers to be delaminated into single sheets.[27;28]

Partial isomorphous substitution of trivalent cations for divalent ones results in a net positive charge on the layers. The acquired positive charge is balanced by the intercalation of anions between the layers. It is the possibility to vary identity and composition of the both the cations (di and trivalent) and anions that gave rise to a variety LDHs having a general formula $[M^{II}_{1-x} M^{III}_x(OH)_2]^{+x} (A^{-n})_{x/n} \cdot yH_2O$, where M^{II} and M^{III} are the divalent and trivalent metal cations, while A is the anion. although the general formulae show only two cations, other ternary LDHs, involving mixtures of different M^{II} and M^{III} cations, have been prepared.[21] Quaternary LDHs and those containing monovalent lithium ions of the type $[LiAl_2(OH)_6]^+[A^n]_{1/n} \cdot yH_2O$ are also known to have similar structures.[22–24] It has been reported that pure LDH phases can only be formed for stoichiometries in the range $0.20 <x> 0.33$, i.e. M^{II}/M^{III} ratios in the range 2-4. Ratios greater than 0.33 have been reported to result cause the formation of M^{III}-O-M^{III} linkages, which are unfavorable, due to charge repulsion or the so-called cation avoidance rule.[25] However, LDHs with stoichiometries outside the range 0.20-0.33 have also been synthesized, e.g. Mg/Ga-CO$_3$ with x as low as 0.07 and x as high as 0.50 for Fe^{II}/Fe^{III} LDHs.[26,27]

Structural studies on LDHs have indicated that the metal-oxygen octahedra are compressed, as in Brucite, along the *c*-axis with the O-M-O bond angles distorted from an ideal octahedral arrangement. Gutmann and Muller, in their work with $[Zn_7Cr_4(OH)_{22}](CO_3)_2 \cdot (CH_2O)$, observed broadening of d-d transitions of Cr^{III} which they suggested to be associated with the distorting of O_h to D_3d symmetery.[28] in Brucite, the unit cell parameter a_o (= 0.3142 nm) is equivalent to the mean distance between adjacent metal centers in the close packed sheets and the value for the corresponding parameter in LDHs can be correlated with the average radii of the metal cations in the layers. lack of correlation between a_0 and the apparent LDH composition has been reported to be due to the presence of other non-LDH phases.[29]

The basal spacing of an LDH, which is defined as the distance from the center of one of the layers to that in the adjacent layer, is larger than that in Brucite ($c_o = 0.4766$ nm) due to the lack of water molecules and anions in the later.[30] There is some correlation between the basal spacing of LDHs with the composition of the layers, although anion size and degree of hydration will have a major influence. Mg_nAl-CO_3 LDHs have been reported to have a basal spacing which decrease form 0.7928 nm for $n = 5$ to 0.7591 nm for $n = 24$.[9] Layer charge density on the other hand has also been reported to increase with a decreasing n leading to stronger electrostatic bonding with interlayer anions and stronger H-bonding with interlayer water molecules. $Ni_{6-x}Mg_xFe_2(OH)_{16}CO_3.4H_2O$ basal space has been reported to increase from 0.778 nm (for x = 0) to 0.791 nm (for x = 6) while the overall cationic charge remained constant.[31] Such behavior was interpreted as indicating that hydroxyl groups bonded to Ni are strongly

polarized than those bonded to Mg resulting in the formation of stronger H-bonds with interlayer carbonate anions.

The interlayer galleries of LDHs have a complex network of hydrogen bonds in a continuous state of flux which is caused by the interlayer water molecules, anions and the hydroxyl groups.[2] Hydroxyl groups bonded to the trivalent cations are reported to be strongly polarized than those bonded to divalent cations, and are said to be the ones which interact with interlayer anions.[32]

1.3   Applications

The physical and chemical properties of layered metal hydroxides allow them to be used for wide variety of applications; applications such as, selective exchange of anions,[33] topotactic incorporation of divalent cations,[34] metal oxide precursors,[35] nanosheets,[36] templates for metal nanoparticles.[37] From these materials or applications, other potential uses arise. Some of the applications are described in the following sections.

1.3.1   Selective exchange of anions

Layered metal hydroxides have been shown to exhibit selectivity towards exchange of ions.[38] For example, zinc hydroxy nitrate has been reported to selectively uptake 2-naftoic acid from a mixture of 1-naftoic acid and 2-naftoic acid.[33] Copper hydroxy nitrate has also been used to separate 2-naftonic acid from 2,7-naftoic acid.[34] Using these examples, it has been inferred that the two hydroxides exhibit the capacity

for molecular recognition and have thus been used for the separation of a mixture of isomers. It was shown that the selective exchange is not only dependent on charge density but also on the three-dimensional structure of the guest anions.

1.3.2 Topotactic incorporation of divalent cations

It has been shown that when zinc hydroxy nitrate, $Zn_5(OH)_8(NO_3)_2$, is added to metal chloride solutions such as MCl_2 ($M^{2+}=Co^{2+}$, Ni^{2+}or Zn^{2+}), a compound with general formula $(Zn, M)_5(OH)_8Cl_2$ is formed.[34] This reaction shows that LHSs can also replace cations located in their main hydroxide layers, a process called "diadochy".[40]This phenomenon has also been described for LDHs such as $Mg_6Al(OH)_6^+[NO_3.2H_2O]^-$ and $[Mg_6Al_2(OH)_{16}]^{2+}[CO_3.4H_2O]^{2-}$. In these LDHs a solution with $5x10^{-4}$ $molL^{-1}$ of Cu, Ni, Co and Zn in the presence of NaCl was able to replace Mg^{2+} from the hydroxide layers.[21]A diadochy reaction is also selective; attempts to incorporated Mn^{2+} (from $MnCl_2$) resulted only in anion exchange.[20]This highly selective uptake of cations allows for these materials to be applied in soil or water treatment.

1.3.3 Metal oxide precursors.

Metal oxide or mixed metal oxides have been applied in diverse fields of science and technology. They have been applied in solar cells, optoelectronic devices, photocatalysis, gas sensors, oxidation and hydrogenation of hydrocarbons.[41,42]Metal oxides are synthesized after thermal decomposition of layered metal hydroxides. It has been reported that the properties of these oxides are dependent on the type of the precursor material.[43]The oxide morphology has been reported to be affected by the speed,

and mechanism of decomposition and also on the distribution of the cations. Temperature is another factor determining the composition of the oxides. For instance, after a copper-cobalt LDH, $Cu_yCo_{2-y}(OH)_3NO_3$ was heated at different temperatures, it was observed that at lower temperatures (295 °C) a hetero-metal oxide ($Cu_xCo_{3-x}O_4$) is formed, but at higher temperature(422 °C);CuO is the predominant phase formed, mixed with some cobalt oxide spinels and also copper metal.[44]Zinc-copper oxides, formed after calcination of zinc-copper HDSs, have also been used for the synthesis of methanol from carbon dioxide and hydrogen.[45] All these examples demonstrate the versatility of the layered metal hydroxides to be applied catalysis. Layered metal hydroxides have also been used as catalyst supports. One example is that of the CdS system which has been synthesized onto the surface of cobalt LHS.[46]

1.3.4   Nanosheets

It has also been shown in literature that layered metal hydroxides can be delaminated into single highly anisotropic nanosheets.[47] These nanosheets can be utilized as building units for the construction of a wide range of functional nanocomposites, such as the synthesis of (i) polymer/LDH nanocomposites, (ii) core-shell multifunctional materials,[48] (iii) thin films,[49] (iv) bioinorganic hybrid materials,[50] (v) electrode materials,[51] (vi) catalysts,[52] and (vii) hybrid magnets.[53,54]

1.3.5   Templates for metal nanoparticles

The possibility of synthesizing metal oxides in the presence of other oxides has been demonstrated in literature. For example, Fe-Al, Co-Al LDHs embedded in gibbsite $Al(OH)_3$ have been calcined to produce nanoparticles of cobalt and iron in an alumina matrix.[37] LDHs can also incorporate compounds such as $Ni(edta)^{2-}$, $Co(edta)^{2-}$, $Cu(edta)^{2-}$ or $Fe(CN)_6^{3-}$ as interlayer anions. Calcination of these materials under vacuum produces transition metal nanoparticles protected from oxidation.[55]

1.4   Preparation techniques

A variety of synthesis routes have been reported in literature; it has been observed that some routes are only feasible for a specific class of compounds. It has also been shown that it is possible to synthesize some compounds using a multiple of methods. Zinc hydroxy nitrate is one material that has been prepared using a variety of methods; it has been synthesized using (i) thermal decomposition of zinc nitrate,[56](ii) reaction of zinc oxide and zinc nitrate[16] and (iii) reaction of zinc nitrate and sodium hydroxide.[57] However, the some physical and chemical properties of the resultant layered material are dependent on the route taken. Some of these properties are crystallite sizes, stability in different pH environments, interaction between anions and the positively charged layers, etc. All these properties will have an effect on the overall reactivity of these compounds, hence one should have knowledge of possible synthesis routes and the effects they have on the final product. Some of the methods that have been reported in literature are detailed below:

(i)   **Salt-oxide reactions**. The hydrolysis of metal oxides and salts is a common route

for HDS synthesis; it consists of the hydrolysis of divalent metal salts, e.g. nickel nitrate,

in the presence of a metal oxide such as zinc oxide.[58] This method has also been used in

the preparation of LHS, such as zinc hydroxy nitrate and copper hydroxy nitrate.[16,59] The

reaction can be represented in an chemical equation, as below.

$$MA_z + MeO + H_2O \rightarrow M_{1-y}Me_y(OH)_{2-x}(A^{m-})_{x/m} \qquad \textbf{Equation 1.1}$$
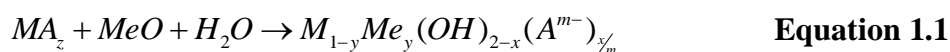
(ii)   **Urea hydrolysis or isocyanate hydrolysis**. Stahlin et al. synthesized well-formed

single crystals of zinc hydroxy nitrate by reacting urea and a zinc nitrate solution.[16] The

hydroxide groups for this reaction come from the urea hydrolysis. The decomposition

process of urea in acidic or neutral solutions produces ammonia and carbon dioxide,

which will further produce ammonium cations and increase the hydroxide concentration.

This procedure has been largely applied for the synthesis of LHS, where only one metal

cation is present. The reaction steps mentioned above are shown below;

$$CO(NH_2)_2 \rightarrow NH_3 + HNCO \qquad \textbf{Equation 1.2}$$

$$HNCO + 2H_2O \rightarrow NH_4OH + CO_2 \qquad \textbf{Equation 1.3}$$

$$NH_3 + H^+ \rightarrow NH_4^+ \qquad \textbf{Equation 1.4}$$

$$M^{+2}A_y + (2-x)OH^- \rightarrow M(OH)_{2-x}(A^{m-})_{x/m} + (y-x)A^{m-} \qquad \textbf{Equation 1.5}$$
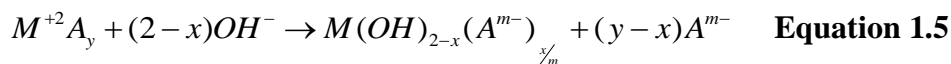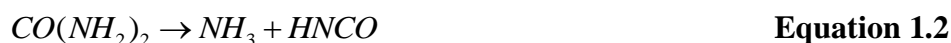
However, compounds synthesized using the method may be contaminated with carbonate

ions, which can also act as a counter-ion.[60,61]

(iii)   **Salt-alkali method**. LHSs and LDHs have also been prepared by a controlled

addition of an alkali solution (usually NaOH) to a solution of metal salt(s). Solution pH

or the OH^-/M^{2+} mole ratio, are the important factors to be controlled. Higher pHs have

resulted in the hydrolysis of the layered structures, formation of metal oxides or the solubilization of the precipitates.[62–64]

(iv)   **Solid state reactions**. This method is related to the urea method described above, but for this reaction, the amount of water required in minimal, enough to just form a paste. The paste is then heated at a specific temperature for a specified amount of time. After cooling, the solid is ground, washed and dried again. This type of reaction has been reported to be highly selective, and it eliminates the separation or purification stages. Cobalt hydroxy nitrate is one compound which was formed using this method.[65–67]

(v)   **Hydrothermal reaction**s. These reactions are usually done in an autoclave, where the reagents are subjected to high pressure and temperatures above boiling point of water. High temperatures result in the reduction of water viscosity and dielectric constant and as well increase the dissociation constant.[68] These all favor electrostatic interactions and result in an increased ripening of the crystals. This method produces materials of high crystallinity than those obtained from precipitation using alkaline solutions.[69] Hydrothermal methods have been used to produce compounds that are stable under acidic conditions, e.g. nickel hydroxy sulphate, which cannot be prepared at room temperature. Magnesium hydroxy nitrate (MgHN) also is another material synthesized under hydrothermal conditions; attempts to synthesis MgHN at room temperature results in the formation of magnesium hydroxide.[70,71]Some authors have also applied microwave heating; they reported improved crystal quality and speed of crystal formation.[72] Zinc nickel hydroxy acetate is one of the materials synthesized using the microwave heating method. It has been reported that the crystals formed using microwave methods grew two times faster than those synthesized using conventional heating, in a furnace. The degree

of crystallinity was reported to be dependent on the power of the microwave; crystals improved with increasing microwave power.[73,74]

(vi)   **Polyol hydrolysis.** This method has been reported for the synthesis of zinc, cobalt and nickel hydroxy acetates. The method involves dissolving metal acetates in diethyleneglycol, 1,2-propanediol or ethanol, forming alkoxyacetates. Alkoxyacetates are then hydrolyzed by the addition of water. The desired compound is formed by controlling the ratio of hydrolysis, nH$_2$O/nM (M=Ni, Zn or Co). Unlike in LDHs and LHS no carbonate contamination is detected using this method of synthesis. However, the method produces materials with a low crystallinity and results in co-intercalation of the polyols.[7,75]

(vii)   **Ion-exchange method.** The method is useful when coprecipitation methods are inapplicable, especially when divalent/trivalent metal cations or the anions involved are unstable in alkaline solutions. In this method, guest anions are exchanged with host anions to produce a new material with different chemical or physical properties. Ion exchange in layered metal hydroxides depends on the electrostatic interaction between the positively charged layers and the guest anions. A number of factors have been reported to affect the extent of reaction in these layered materials: (i) affinity of guest anion, (ii) exchange medium, (iii) pH value and the chemical composition of the layers.[76,77]

1.5   Kinetic Modeling

Ion exchange and adsorption reactions can be understood with the aid of kinetic analysis, which can be utilized for the synthesis of efficient ion-exchangers or adsorbents. Chemical kinetics involves the study of reaction rates. The two main reasons why rates of chemical reactions are quantified are;(i) by parameterizing the reaction rates as a function of temperature and concentration, the rate of reaction can be predicted for any set of conditions, even for reactions that were not measured under those conditions. The accuracy of the predictions depends on the form of the derived function used for parameterization and how close the set of conditions are to those used for determining the parameter. (ii) From kinetics studies details about reaction mechanisms can be revealed. One of the fundamental dogmas of chemical kinetics is that reaction mechanisms cannot be solely proved on the basis of kinetic data alone; at best, one can only demonstrate that a given mechanism is consistent with the obtained kinetic data.[78–81] The basic kinetic constructs such as reaction order, activation energy, reaction rate and rate constants had been developed by the end of the 19th century.[82] These afore-mentioned kinetic concepts were generalization of empirical knowledge about homogeneous reactions. Hence, their application to the results from heterogeneous reactions should not be expected to be accurate. This is because the factors that affect diffusion of matter to and from a reaction site, in heterogeneous systems, are different that those in homogeneous systems. Properties of the solid such as particle size and/or the possibility of phase transformations occurring during reaction may have an effect on overall reaction mechanism.

The mechanistic interpretations in solid state reactions are based on the concepts of a single-step reaction, and can be represented by the general expression below.

$$\frac{d\alpha}{dt} = Ae^{-(E_a/RT)}f(\alpha) \qquad \textbf{Equation 1.6}$$

where, $f(\alpha)$ is the reaction model representing a certain solid-state mechanism, α is the extent of reaction at time t, $E_a(Jmol^{-1})$ is the activation energy, R $(Jmol^{-1}K^{-1})$ is the gas constant and A (s^{-1}) is the pre-exponential (frequency) factor. The idea of the reaction model suggests that the reaction mechanisms give rise to characteristic α versus t or $d\alpha/dt$ v t plots or mathematical functions (i.e. $f(\alpha)$). Experimental data is compared against known reaction models; the model that accurately reproduces the data is chosen. The table below is a collection of some of the models that have been widely applied.

Table 1.1. Rate and integral expressions for some of the models commonly used for kinetic analysis of solid-state reactions.

Model	Differential form $f(\alpha)=1/k\ d\alpha/dt$	Integral form $g(\alpha)=kt$
Avrami-Erofe'ev A1	$(1-\alpha)$	$-\ln(1-\alpha)$
Avrami-Erofe'ev A2	$2(1-\alpha)(-\ln(1-))^{1/2}$	$(-\ln(1-\alpha))^{1/2}$
Avrami-Erofe'ev A3	$3(1-\alpha)(-\ln(1-))^{2/3}$	$(-\ln(1-\alpha))\alpha^{1/3}$
Prout-Tompkins	$\alpha(1-\alpha)$	$\ln(\alpha/(1-\alpha))+c^a$
1-D diffusion D1	$1/(2\alpha)$	α^2
2-D diffusion D2	$-(1/\ln(1-\alpha))$	$((1-\alpha)\ln(1-\alpha)+\alpha$
3-D diffusion D3	$(3(1-\alpha)^{2/3})/(2(1-(1-\alpha)^{1/3}))$	$((1-\alpha)\ln(1-\alpha)+\alpha$
Ginstling-Broushtein D4	$3/(2((1-\alpha)^{-1/3}-1))$	$1-(2/3)\ \alpha-(1-\alpha)^{-2/3})$
Second order	$(1-\alpha)^2$	$(1/(1-\alpha))-1$
third order	$(1-\alpha)^3$	$(1/2)((1-\alpha)^{-2}-1)$
Power law (P2)	$2\ \alpha^{1/2}$	$\alpha^{1/2}$
Power law (P3)	$3\ \alpha^{2/3}$	$\alpha^{1/3}$

The integral form of the isothermal rate law is shown below;

$$g(\alpha) = Ae^{-(E_a/RT)}t$$

Equation 1.7

where, $g(\alpha)$ is the integral reaction model, given by

$$g(\alpha) = \int_0^\alpha \frac{d\alpha}{f(\alpha)}$$

Equation 1.8

Reaction mechanisms in solid state reactions are often too complicated to be characterized by a simple kinetic model.[83] The solid state transformations which take place tend to involve several steps with different activation energies. The contribution of each step to the overall process may vary with both temperature and extent of reaction. Application of model-fitting methods for analysis of such reactions will result in extraction of a single value of the activation energy. The obtained value is an average that will not reveal the changes in the reaction mechanism and kinetics as a function of T and α. Kinetic analysis, be it isothermal or nonisothermal, has been performed using either model-fitting or model-free methods. Model-free (isoconversional) methods are often used to describe the kinetics of systems which might have activation energies that vary as a function of T and α. With isoconversional methods it is possible to calculate activation energy values for each extent of reaction without any modelistic assumptions. Linearization of equations 1.6 and 1.7 is done by taking the natural logarithms of the two expressions, giving equation 1.9 and 1.10, respectively.

$$\ln(\frac{d\alpha}{dt}) = \ln Af(\alpha) - \frac{E_a}{RT}$$

Equation 1.9

$$\ln t = \ln \frac{g(\alpha)}{A} + \frac{E_a}{RT} \qquad \textbf{Equation 1.10}$$

A plot of ln(dα/dt) or ln t against 1/(RT) will yield E_a.[84–86]

The most widely utilized approach for evaluating intercalation kinetics has been the Avrami-Erofe'ev nucleation-growth model.[87,88]This model has been successfully applied to a variety of reactions which includes phase transformations in glass, hydrogenation of metal alloys,[89] polymer degradation,[90]and intercalation reactions.[81]The model plots α against t, and is expressed below.

$$\alpha(t) = 1 - e^{(-(kt)^m)} \qquad \textbf{Equation 1.11}$$

Rearranging equation 1.11 and taking natural logarithms twice gives a new equation:

$$\ln\left[-\ln(1-\alpha)\right] = m\ln(t) + m\ln(k) \qquad \textbf{Equation 1.12}$$

The equation resembles the equation of a straight line; with m being the slope and $m\ln(k)$ the intercept. The magnitude of m gives information about the mechanism of the reaction, whether the reaction is diffusion controlled ($m<0.5$), nucleation controlled or both ($0.5<m<1$).[92–94]The double-logarithm plots (equation 1.12) have been used for evaluation of rate constants since the 1950s, but they were made popular by Sharp and Hancock in 1972.[95] Hence, they are often popularly known as Sharp-Hancock plots. Other reaction models used for the exploration of various ion exchange reactions are described below;

First order rate model. This model has been applied to ion exchange reactions and can be expressed as;

$$\ln(\frac{C_t}{C_0}) = -k_d t \qquad\qquad \textbf{Equation 1.13}$$

which can be expressed as;

$$\ln(\alpha) = -k_d t \text{ ,} \qquad\qquad \textbf{Equation 1.14}$$

where α is equal to C_t/C_o, k_d is the apparent rate constant, C_t is concentration at time t while C_o is the initial concentration[96].

Parabolic diffusion. The model is based on the assumption of a diffusion-controlled rate-limiting process in media with homogeneous particle sizes[97].

$$\left(1 - \frac{c_t}{c_0}\right)\frac{1}{t} = k_d t^{-0.5} + a \text{ ,} \qquad\qquad \textbf{Equation 1.15}$$

where k_d is the apparent uptake rate constant. The model plots $\left(1 - \frac{c_t}{c_0}\right)\frac{1}{t}$ against $t^{-0.5}$. The ratio of C_t: C_0 can also be expressed as the extent of reaction (α).

Modified-Freundlich. The model is expressed as;

$$C_0 - C_t = k_d C_0 t^a \text{ ,} \qquad\qquad \textbf{Equation 1.16}$$

where k_d is the uptake rate coefficient and *a* is a constant. This model has been widely applied in ion exchange and adsorption with clay materials. Rearrangement of the equation yields the form below[98];

$$\log(1 - \frac{C_t}{C_0}) = a\log(t) + \log k_d \qquad \textbf{Equation 1.17}$$

1.6 Motivation of Study

Layered metal hydroxides structural composition can be altered by changing the identity of the anions or the metal cations, resulting in nanodimensional structures with tunable physical and chemical properties. Anion identity has been changed using ion exchange methods. Depending on the size of the guest anions, ion exchange in layered metal hydroxides results either in expansion or contraction of the inter-layer space. In terms of crystal dimensions, only the *c* parameter is affected, while *a* and *b* are constant, a behavior termed *topotactic*.[99,100] On the other hand, varying the metal identity will affect *a* and *b* parameters, which will in turn affect the thickness of the layers and also the overall positive charge of the layers. This ability to vary the intralayer metal composition as well as the interlayer anion identity makes these materials attractive for a variety of applications including use as catalysts,[1,101] catalyst precursors,[102] catalyst support materials,[103] adsorbents,[104] and ion exchangers.[105–107]Our work focused mainly on anion exchange and adsorption reactions. We examined how the metal and anion identity affected reaction rates during anion exchange or adsorption. The processes studied are described in the next section.

1.6.1 Uptake of halogenated acetates: effects of anion structure and hydroxide layer structure.

Halogenated acetates are environmental pollutants introduced into the water systems as by-products of water chlorination, pesticide degradation and atmospheric degradation of refrigerant compounds.[108]The acids have a high toxicity level, persistence, and potential carcinogenicity. Hence their disposal or removal from water systems has been a major environmental concern. There have been quite a number of techniques suggested for the remediation of drinking water containing these compounds, among which are biodegradation,[85]microwave,[111]photolysis assisted with ultrasound,[110] reductive processes using zero valent iron or iron-based bimetal.[112] The major drawback limiting the applicability of these methods is firstly their high expense and poor dechlorination efficiency. Electrochemical methods have also been applied; they have been reported to be more efficient than the methods mentioned before.[113] Electrochemical methods have been used for the destruction of carbon-halogen bonds. Oxidation processes resulted in the formation of undesired reactions due to the formation of reactive radicals on the electrode surface. Reductive halogenation of halogenated acetates (HAAs) which occurs at very negative potentials, where reduction of water may take place, leading to production of hydrogen and a reduction of current efficiency.[114–116]With all the promises and drawbacks associated with the aforementioned remedial methods, sequestration of HHAs using layered metal hydroxides will be more likely adopted for the treatment of drinking water containing HAAs. Layered metal hydroxides have got a number of advantages which would give them an edge over the other methods, among them being easy of synthesis, the ability to modify the hydroxide layer structure and selectivity

towards anion uptake. Modification of the layer structure is accomplished by changing the identity of the metal cations or counter-ions. With layer metal hydroxides a variety of materials can be made, with tunable chemical and physical properties, which can a play a positive part in the optimization of these materials.

In this study we focused on effects of changing nature or identity of the HAAs on exchange efficiency. This was done using acetate (Ac), chloro acetate (ClAc), dichloro acetate (dClAc) and tri chloroacetate (tClAc) as the target anions and zinc nickel hydroxy nitrate as the exchange material (ZnNiHN).In a related study, we investigated the effects varying the hydroxide layers on the uptake on anions. The materials utilized for this work initially had nitrates and/or acetates as counter-ions. Results obtained from the work described above revealed that ZnNiHN was better at sequestrating Ac and ClAc than dClAc and tClAc. In an effort to improve the uptake of tClAc we substituted Ni^{2+} with Al^{3+} and Ga^{3+} resulting in two materials, zinc aluminum hydroxy nitrate (ZAN) and zinc gallium hydroxy nitrate (ZGN). These trivalent cations were introduced as a way of increasing the overall hydroxide-layer charge, which might have an effect on the uptake of the acid. The tClAc uptake efficiency for ZAN, ZGN and ZNN will be explored using kinetic analysis and also equilibrium studies.

1.6.2   Adsorption of Methyl Orange using calcined oxides and mixed oxides.

Thermal treatment of LDHs (calcination) to up to about 200 °C induces dehydration. Treatment up to about 500 °C causes dehydroxylation and loss of vaporizable anions such carbonates, acetates and nitrates. Carbon dioxide and nitrogen dioxide can also be produced following decomposition of carbonates and nitrate.

Temperatures above 500 °C will result in the formation of mixed metal oxides, and in some cases, spinels.[117] For some compounds oxide formation can start at temperatures around 300 °C. It is interesting that the calcined LDH is able to regenerate the layered structure when it is exposed to moisture and anions.[107]Various terms have been used to describe this process among them being regeneration, restoration, reconstruction, calcination-rehydration process, "structural memory effect" or simple memory effect.[118–120]We were interested in exploiting this memory effect for the absorption of methyl orange, an azo-dye.

Azo dyes constitute about a half of global dye-stuff production (700 000 tons annually), from these, about 15 %find their way into water systems without proper treatment.[121] These organic dye pollutants are mainly produced from textile industries and they have received a great attention due their increasing environmental risks such as aesthetic problems, high biotoxicity, potential mutagenicity and carcinogenic effects.[122] Thus, the removal of dyes from water bodies has become a critical issue. A variety of methods have been applied for the treatment of wastewater including coagulation-flocculation,[123] membrane separation,[124] ozone treatment,[125]adsorption,[126] ion exchange, and biological treatment. Among these, adsorption has been found to be a reliable alternative, due to its high efficiency and ease of operation.[127] Various adsorbent materials including activated carbon,[128] mesoporous carbon, zeolites,[129] fly ash,[130] and polymers have been found to be capable of removing dyestuffs from wastewater.Considering the threats posed by these dyes and the need for cleaner and safer drinking water, it is still indispensable to exploit new adsorbent materials with high adsorption capacities and removal efficiencies and consequently leading to low

operational costs. In this study we compared the efficiency of calcined LDHs against uncalcined LDHs on adsorption/exchange of methyl orange. Just like ion-exchange of HAAs, we again exploited the effects of varying metal identity of the adsorbent material on uptake efficiency.

2.   Experimental

2.1   Instrumentation and Characterization

2.1.1   Powder X-ray Diffraction.

Powder X-ray diffraction (PXRD) is one of the primary tools of chemical analysis used in this work. It is a rapid analytical technique primarily used for phase identification of crystalline or amorphous materials. Since 1912, when Max von Laue discovered that crystalline substances act as three-dimensional diffraction gratings for X-ray of identical wavelengths to the spacing of planes in a crystal lattice[131], XRD has been a common tool for elucidating crystal structures and atomic spacing. This technique is based on constructive interference of monochromatic radiation and a crystalline sample. Diffraction of occurs when X-rays are scattered by a periodic array with long-range ordering, producing constructive interference at specific angles. Electrons in an atom coherently scatter the X-rays; the strength with which an atom scatters the X-rays is proportional to the number of electrons around the atom. X-rays constructively interfere when conditions satisfy the Bragg's Law ($n\lambda=2d\sin\theta$)[132], where λ is the wavelength of incident X-rays, θ is the angle between the incident ray and the scattering planes, while d is the d-spacing between the planes in the lattice. Conversion of diffraction peaks to d-spacing allows for the identification of different minerals since each mineral has a set of unique d-spacings. The experimental technique relies on three main components; the X-ray tube, sample holder, and X-ray detector. The instrument used in this study was a

Rigaku Miniflex II diffractometer with a CuK_α (1.54 Å) radiation source with a voltage of 30 kV and 15 mA. Crystallite size estimation was done using the Scherer equation below[133], after correcting for broadening using a silicon standard supplied by the manufacturer (Rigaku Corporation). For the silicon standard, the 111 peak is observed at 28.4°.

$$\tau = \frac{\kappa\lambda}{\beta\cos\theta} \qquad \textbf{Equation 2.1}$$

where τ is the crystallite size, K is a constant (0.9 for powders), β is the Full Width at Half Maximum (FWHW) of the diffraction peak at angle θ[134].

2.1.2 Fourier Transform Infrared Spectroscopy

Fourier Transform Infrared Spectroscopy (FTIR) is an important technique in both organic and inorganic chemistry. It is an easy way of identifying the presence of specific functional groups. Conventional transmission modes rely on the use on KBr pellets for samples preparation, but Attenuated Total Reflection (ATR) mode does not. With an ATR accessory, samples are undiluted, and measurements are done in a matter of seconds, giving this modern technique an advantage over its predecessor. The technique involves placing a sample on top of a crystal with a high refractive index and polished surface; zinc selenide (ZnSe) crystal was used in this study. An infrared beam enters the crystal at an angle of 45°, and is reflected internally in the crystal and back to the detector. The beam is not reflected directly by the crystal surface but by a virtual layer within the optically less dense sample, a phenomenon known as Goos-Hänchen effect[135].

The fraction of light entering the sample is known as evanescent wave, and its penetration depth is dependent on wavelength, refractive index of the crystal, the sample and the lights angle of incidence. The penetration depth is typically in order of a few microns. The after sample through the sample the evanescent wave is attenuated, and after several internal reflections, the beam exits the crystal and is directed towards the detector.
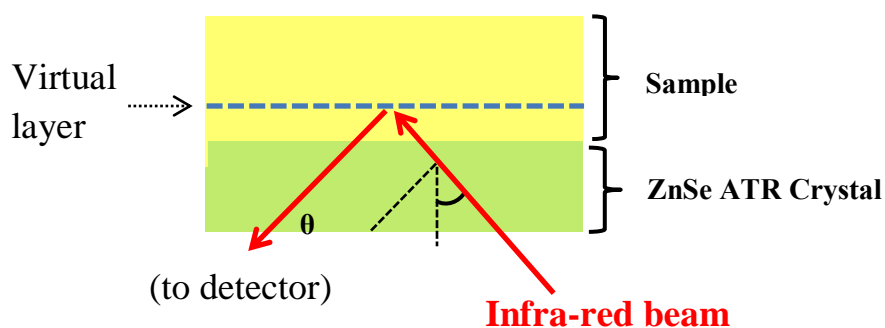
Figure 2.1. ATR effect. Showing an IR beam passing through a ZnSe crystal and getting reflected a few microns into the sample.

ZnSe crystal used in this study has a refractive index of 2.43, spectral range of 20,000-500 cm^{-1}. With this crystal a depth of 1.66 mm is achieved at 45° incident angle. Infrared spectral data reported in this study were collected using a Nicole Magna-IR spectrometer (Perkin Elmer Spectrum 100) using a single reflection ATR accessory.

2.1.3   Atomic Absorption Spectroscopy

Flame atomic absorption spectroscopy (AAS) was used for quantitative analysis of the metal in the layered materials. A known mass of the LHD/HDS was dissolved in an acid (hydrochloric acid or nitric acid) and then diluted to the appropriate concentration. Calibration curves were done for each individual metal cation, by dissolving a known mass of their corresponding pure metals in HCl or HNO_3 followed by a series of dilutions to make different concentrations. Aluminum, zinc, nickel and gallium Hollow Cathode lamps (**HCL**) were used for the quantitative analysis of the appropriate metals. An acetylene-air mixture was used again as fuel for the flame. Specific lamp currents and absorption wavelengths are presented in chapters that follow.
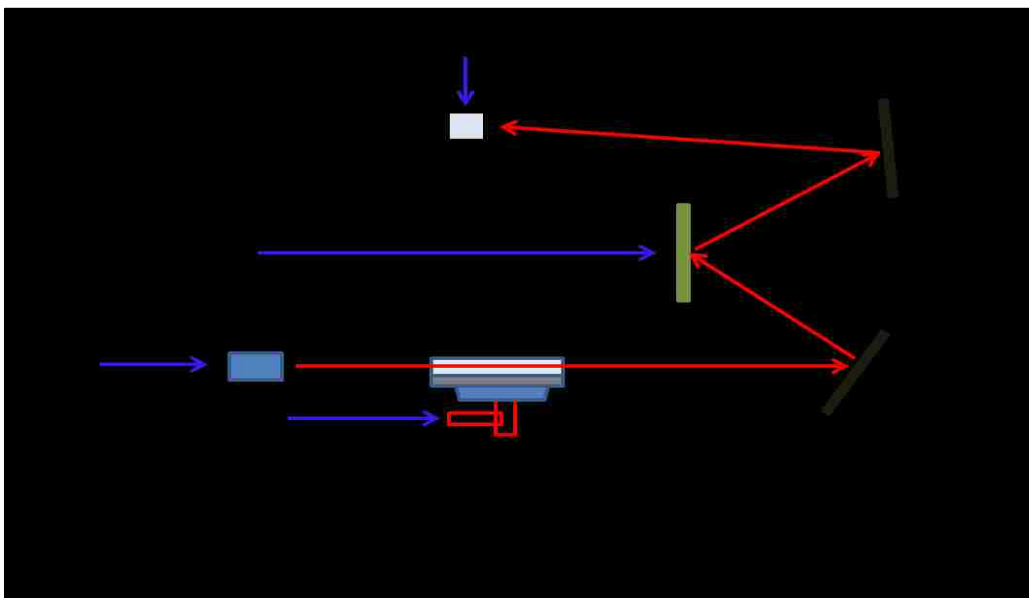
Figure 2.2   The basic system of a flame Atomic Absorption Spectrometer.

2.1.4   High Performance Liquid Chromatography

The HPLC instrument used in this study was a Shimadzu Prominence SPD-20A, with a Prominence Degasser DGU-20A5 and fitted with a UV/VIS detector. A Supelco, Discovery C18; 25 cm x 4 mm x 5 μm column was used for the quantitative analysis of trichloro acetic acid solution at 210 nm. Injection volumes of 10-20 μL and flow rates of 1 mL/min were used for all analytes. Double de-ionized water (>16 Ω) was used for preparing all mobile phases. Mobile phases were degassed by sonicating under vacuum. Separation was achieved using an isocratic isothermal method. The actual method and sample preparation details are presented in chapters 4.2.2 and 5.2.

2.1.5   Thermal Analysis

The thermal methods used in this study were Thermogravimetric analysis (TGA) coupled to Differential scanning Calorimetry (DSC) and Fourier transform infrared spectroscopy (FTIR) .DSC is a technique for measuring the energy required to establish a nearly-zero temperature difference between the sample and a reference material, while the two are subjected under identical temperature program. The temperature program can be at a linear heating rate (non-isothermal), constant heating rate (isothermal) or a combination of heating, cooling and isothermal stages. Thermal analysis has been applied in polymer chemistry, in order to determine polymer thermal stability and also for their characterization[136,137].

The machine used for TG-FTIR was a Netzsch TG 209 F1, instrument coupled to a Fourier Transform Infrared spectrometer. This equipment has the advantage of identifying gaseous compounds produced as the temperature increases. Ideally, low temperature weight loss arises from the loss of water molecules, while higher temperature weight reductions arise from material decomposition. Samples with masses ranging from 10-15 mg were placed in aluminum crucibles and then heated under nitrogen atmosphere starting from room temperature to 800 °C.

2.1.6   Computational calculations and Reitveld refinement

Dipole moments, electronic spatial extents and atomic charges of all the anions were calculated using Gaussian 03W program. The geometry optimization of the anions was carried out using B3LYP level of theory with 6-311G +basis set with a solvation model, integral equation-formalism polarizable continuum model (IEF-PCM).[138]

Reitveld refinement is a technique pioneered by Hugo Reitveld for use in the characterization of crystalline materials.[139] XRD and Neutron diffraction of powdered samples produces a characteristic pattern of reflections at certain positions. The technique relies on height, width and position of these reflections to determine specific aspects of the material structure. It then matches the theoretical profile to the experimental profile using the least squares approach. This is done by minimizing a function M by evaluating the difference between a calculated profile y^{cal} and the observed profile y^{obs}.

$$M = \sum_i W_i \left(y_i^{obs} - \frac{1}{c} y_i^{cal} \right)^2 \qquad \textbf{Equation 2.2}$$

where W_i is the statistical weight and c a scaling factor such that $y^{cal} = cy^{obs}$.

Rietveld refinement has been utilized in structure modeling of a variety of clay materials[140] and crystallizable organic macromolecules.[141] The Rietveld method requires;

- Accurate diffraction data,

- Identification of all phases within the sample,

- Standard phases which will be compared against those in the sample,

- A Rietveld refinement program.

Data accuracy is improved by calibrating the XRD instrument. After calibration, data collection has to be done at low scan speeds and for a wider 2 theta range. Scan speed of 1 °/min was used for the range 2.5 to 80 °. Standard phases are obtained from crystallographically data bases such as the crystallography open database (COD).[142] For materials with known phases, Rietveld analysis will be able to do a quantitative analysis of all the phases. The refinement program used in this work was the Material Analysis Using Diffraction (MAUD) refinement program. [143–145]

2.2 Anion exchange reactions

Ion exchange and adsorption reactions were conducted under isothermal conditions in a shaking water bath running at 300 rpm. Multiple reaction samples were prepared in 100 ml glass vials, by adding 0.10 g of the exchange material with 10 ml of the anion solution. Reactions were stopped after predetermined time periods and then filtered and washed for further analysis, using mainly PXRD, FTIR (solids) and UV-vis (solution). Solids were allowed to dry for 24 hrs before analysis, while solutions were analyzed immediately after filtration.

The change in anion concentration in solution was monitored by observing the change in absorption band maxima, of the anion of interest, as a function of time. Calibration curves were done determined in order to convert absorbance into concentration. For the nitrate the UV band maxima was at $\lambda = 300$ nm. Concentration change due to uptake of carboxylic acids was monitored using HPLC at $\lambda = 210$ nm. The ratio of anion concentration at time t (C_t) and at equilibrium (C_{eqm}) gives the parameter α, known as the extent of reaction (equation).

$$\alpha = \frac{C_t}{C_{eqm}}$$
　　　　　　　　　　　　　　　　　　Equation 2.3

Solid phase transformations were monitored using PXRD as described earlier. A peak characteristic of reactant or product phase was identified in the PXRD data; following baseline correction the peak was fit to a Lorentzian or Gaussian function[146]. From these fits, peak positions, width, height and FWHM were obtained. Ideally the most intense peak, usually indexed as the 001 reflection, is monitored for kinetic purposes. In exchange reaction, the 001 peak of the layered material will decay while a new peak of corresponding to the guest anion will increase. The change in intensity of these peaks as a function of time will yield α. As for the zinc nickel hydroxy nitrate –halogenated acetate system two phases of the host nitrate were observed upon intercalation of the dichloro acetic acid and trichloro acetic acid. These two peaks were summed up in order to calculate α, as illustrated in equation 2.4.

$$\alpha_{host} = \left[\frac{1 - \left(\dfrac{I_{h(t)}}{I_{g(t)} + I_{h(t)}}\right)}{1 - \left(\dfrac{I_{h(t)}}{I_{g(\infty)} + I_{h(\infty)}}\right)} \right]$$

Equation 2.4

where $I_{h(t)}$ is the sum of the two nitrate peaks at time t, $I_{h(\infty)}$ is sum of the two nitrate peaks at equilibrium, $I_{g(t)}$ is the guest anion peak intensity at time t, while $I_{g(\infty)}$ is the guest anion peak intensity at equilibrium[87]. For reactions which go to completion and with no peak splitting the above equation can be as simplified as below:

$$\alpha = \frac{I_{g(t)}}{I_{h(t)} + I_{g(t)}}$$

Equation 2.5

With this equation it can be seen that at $t = 0$, $I_{g(t)} = 0$ and $\alpha = 0$ while at $t = \infty$, $I_{h(\infty)} = 0$ and $\alpha = 1$, implying α values will range from 0 to 1.

3. **Anion release and uptake kinetics: Structural changes of layered 2-dimensional nanohybrids upon uptake of acetate and chlorinated acetate anions.**

3.1 Introduction

Haloacetic acids or halogenated acetates (HAAs) are environmental contaminants which have been detected in drinking water[147,148]. They are formed as by-products of water chlorination[149–151], and also as products of pesticide and refrigerant degradation[152]. These compounds have been shown to cause liver tumor in mice[153,154]. Various techniques have been applied for the treatment of drinking water containing HAAs, some of which include; photolysis assisted with ultrasound[155], microwave[111], biodegradation[109] and reductive processes using zero valent iron[156]. However, these methods are expensive and have poor dechlorination efficiencies[155].

These emerging environmental hazards of HAAs and the inefficiency of the current remediation techniques, has motivated us to investigate the possible use of layered metal hydroxides as HAAs sequestrating materials. Layered metal hydroxides are an emerging class of compounds that have recently attracted much attention in science and technology due to their brucite-like structure and consequent ion exchange and intercalation capabilities[30,57]. These materials have positively charged two dimensional nano layers and charge balancing inorganic/organic anions[6]. Their unique structural and physiochemical properties make them intriguing substrates for advanced materials design. They have also found use in catalysis[157,158], fire retardancy[159], magnetism and pharmacology[160]. The materials studied in this work are classified as hydroxy double

salts (HDSs)[161], with a general formula: $[(Me^{2+}_{1-x} M^{2+}_{2x})(OH)_2](A)_{2x}^{-} \cdot mH_2O$, where Me^{2+} and M^{2+} are divalent metals, and A^{n-} is the exchangeable counter anion[162]. The counter ions can be monovalent, for example, Cl^-, NO_3^-, or CH_3COO^-, or divalent, such as SO_4^{2-} or CO_3^{2-}, or many other organic and inorganic anions[163].

To understand the fundamental chemistry governing HAA removal from water using layered metal hydroxides, four structurally related anions: acetate (Ac), chloroacetate (ClAc), dichloroacetate (dClAc) and trichloroacetate (tClAc) were investigated. There have been quite a number of publications on the use of layered metal hydroxides for water purification purposes[164], however very little is still known about the relative importance of factors controlling the uptake or release rates of anions within the material d-spacing[163]. Release and uptake of anions is known to be affected by a number of parameters; the mode of binding of the anions to the positively charged layers[165], the charge and size of the anions, and the metal composition of these layered nanohybrids play an important role in the reactivity of these materials[163]. Anions have been shown to interact not only with the metal centers but also with the hydroxyl groups, water molecules and also with other anions[2]. All of these factors and interactions can affect the overall kinetics of the exchange reactions, making it difficult to systematically predict reactivity.

In this study, we report how anion sizes characterized by electronic spatial extents (ESE) and the overall charges on the oxygen atoms interacting with the metal centers correlate with exchange reactivity. ESEs are computed as the expectation value of electron density multiplied by the distance from the center of mass of a molecule[166,167]. ESEs are important due to their relationship to certain applications, such as determining

whether a molecule will fit in the active site of an enzyme, and also determination of the cavity size for solvation calculations, and they have also been used for to calculating spatial sizes of conformers[168].

Reaction kinetics in layered metal hydroxides have been studied by either monitoring solid phase or solution phase transformations, but very limited work has been conducted whereby a concurrent analysis of the two phases was done. We report here the kinetic data obtained from ex-situ analysis of the two phases. Analyzing both solid and solution phases reveals more information about ion exchange kinetics, since the information obtained from these two phases tends to complement each other. In layered metal hydroxides or other related materials, X-ray diffraction (XRD) has been the primary technique for monitoring temporal solid state transformations,[15] while UV-visible spectroscopy has been utilized for solutions.[103,169] In solids, quantitative kinetic data has been extracted by determining the integrated intensities of the Bragg reflections of the host and product phases.[94,170] The changing peak intensities from both phases are converted into a dimensionless quantity known as the extent of reaction (α). It is this α and time (t) that are used to fit data into various known kinetic models,[171] After fitting, rate constants (k) can then be evaluated.

The Arrhenius equation has been widely applied for the evaluation of activation energies in different systems involving solids, liquids or gases. With the Arrhenius equation, constant activation energy is usually anticipated, meaning that E will be independent of the reaction pathway. This assumption seems reasonable for gas phase reactions, where transformations are known to take place by a series of isolated binary collision of molecules[172]. Ion exchange in layered metal hydroxides and other

heterogeneous systems results is a variation of certain physical properties of the reaction medium which may cause E to vary as a function of reaction progress (α). Reaction mechanisms in heterogeneous condensed phases are often unknown or too complicated to be characterized by a single kinetic model[83]. The processes tend to occur in a series of steps which have different rates. To describe the kinetics of such systems , isoconversional (model-free) methods have often been applied[173–175]. This model-free approach has been utilized in thermal analysis to identify systems which cannot be fit to a single model[35].

The Avrami-Erofe'ev nucleation-growth model (Eq3.1), which is a form of a model-fitting approach, is one of the most widely utilized approach for evaluating intercalation or exchange kinetics within heterogeneous systems[94,95,176,177];

$$\alpha(t) = 1 - e^{(-(kt)^m)} \quad \textbf{Equation 3.1}$$

where α, t, m and k are the extent of reaction, time, the Avrami exponent and the rate constant respectively. The Avrami exponent is frequently used to provide insight into the reaction mechanism. This ability to describe the mechanism m is one of the reasons why this method is widely utilized. The change in activation energy may be explained by a change in reaction mechanism. Utilization of model based techniques will not reveal the dependency of E on α, since these approaches are based on the assumption that the reaction mechanism will remain constant. Therefore starting with a model free approach, such as the isothermal isoconversional approach used here, is useful to determine whether

model-based fitting is appropriate. To reveal this dependency of E on α, an integral form of the isothermal isoconversional analysis methods (equation 3.2) is used.

$$\ln t_\alpha = \ln \frac{g(\alpha)}{A} + \frac{E_{iso}}{RT} \qquad \textbf{Equation 3.2}$$

where E_{iso}, $g(\alpha)$, A, t_α, R and T are the activation energy, integral reaction model, pre-exponential factor, time to get to a specific conversion, gas constant and temperature, respectively. The gradient of the slope of plot of $\ln t_\alpha$ against 1/T gives the activation energy corresponding to a specific α.

The purpose of this study is to understand the kinetics and mechanisms involved during release of nitrate ions upon intercalation of halogenated acetates into the d-spacing of layered metal hydroxides. By revealing the parameters that govern the exchange of these anions, next-generation materials can be designed to efficiently remove pollutant anions from contaminated water systems.

3.2   Experimental

3.2.1 Materials

Zinc oxide (98+ %) was obtained from Sigma Aldrich Chemical. Nickel (II) nitrate hexahydrate (98+ %), chloro acetic acid (99+ %), dichloro acetic acid (99+ %) were obtained from Alfa Aesar Co. Acetic acid (99.9%) and trichloro acetic acid (99+%

were obtained from DBH. Sodium hydroxide (pellets, 99%) was obtained from J. T. Baker. All chemicals used were as obtained from the manufacturer.

3.2.2 Synthesis

The hydroxy double salt was prepared following a literature coprecipitation method[178] as follows: A volume of 60 mL of 1 M $Ni(NO_3)_2$ solution (= 0.06 mol) was added to 9.8 g of ZnO (0.12 mol) dispersed in a few milliliters of water. The dispersion was allowed to stand for 6 days at 65 °C. The solid was isolated, washed using warm deionized water, and dried at room temperature for 48 hrs.

The acids (Ac, ClAc, dClAc and tClAc) were reacted with an equimolar amount of NaOH in enough deionized water to produce 0.2 M solutions. Exchange reactions were investigated in the temperature range 24 to 50 °C. All the exchange reactions were performed in a shaking water bath with a temperature stability of ± 0.2 °C. Multiple 15 ml of solutions of each exchange solution were poured into 50 ml glass sample bottles. These solutions were left in the water bath for at least 5mins, allowing them to attain the reaction temperature. 0.15 g of the dried HDS was then added into the glass vials with the solutions; the samples were then agitated in a water bath at a speed of 300 strokes per min. The reactions were quenched by filtration after a specified time period. The solid samples were washed with distilled water and allowed to dry at room temperature.

3.3   Results and Discussion

3.3.1   Solid phase structural changes
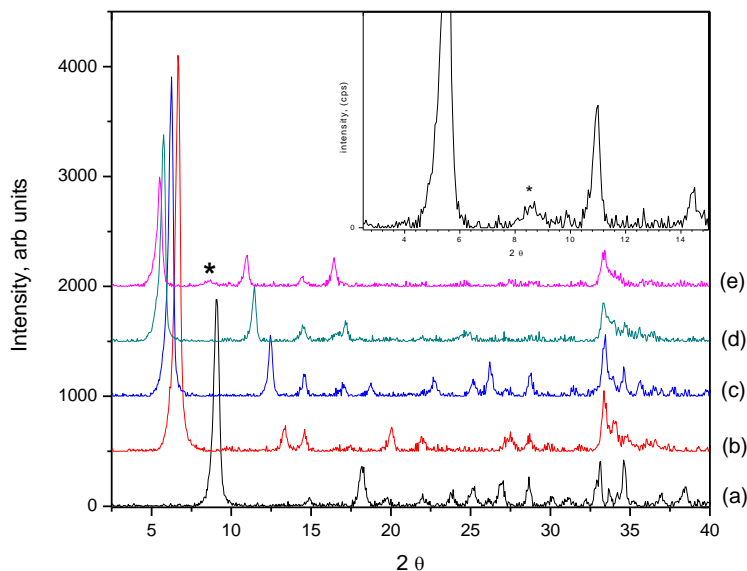
Figure 3.1. PXRD patterns for (a) ZnNiHN and exchanged products (b) ZnNiHAc (c) ZnNiH.ClAc (d) ZnNiH.dClAc (e) ZnNiH.tClAc. Insert is for an expanded part of (e), with the asterisk showing the nitrate peak.

Powder X-ray diffraction (PXRD) patterns shown in figure 3.1 are for the precursor ZnNiHN and its exchange products after reacting at 50 °C for 24 hrs (ZnNiHAc and ZnNiH.ClAc), 48 hrs for ZnNiH.dClAc and 54 hrs for ZnNiH.tClAc. The tClAc ions did not completely exchange with nitrates, even after 54 hrs of reaction at the same temperature, as indicated by the small residual peak marked by an asterisk (*) figure 3.1(e), and also as shown in figure 1(insert). All of the materials, precursor and its exchanged products, have intense symmetrical 00l Bragg reflections which are equally

spaced, indicating that the materials are layered and highly crystalline[87]. High range ordering going up to the third order has also been observed for all the materials. It should be noted that the labeling of basal planes used here, for all the materials, do not indicate assigned Miller indices since the single crystal structure analysis of ZnNi HDSs has not been carried out. The observed d-spacing spacing of ZnNiHN (9.7 Å) and ZnNiHAc (13.3 Å) are consistent with the respective literature values of 9.7 Å and 13.0 Å reported previously for these compounds[10,178]. The d-spacing increased from 9.7 Å to 13.0 Å when a NO_3^- is replaced by a larger Ac^-, showing that there been an exchange reaction resulting in an expansion of the d-space. The d-spacing also expanded to 14.4 Å, 15.7 Å and 16.0 Å when ClAc, dClAc and tClAc were intercalated, respectively. Changes in d-spacing due to ClAc, dClAc and tClAc intercalation have not been compared to any literature values because these materials have not been intercalated into any ZnNi HDSs. The observed full widths at half wavelengths (FWHWs) were used with the Scherrer equation[179], to obtain estimates of crystallite sizes of 19.6 ± 0.8 nm for ZnNiHN, 21.9 ± 0.4 nm for ZnNiHAc, 23.6 ± 1.6 nm for ZnNiH.ClAc, 24.2 ± 1.8 nm for ZnNiH.dClAc and 23.3 ± 1.7 nm for ZnNiH.tClAc. At lower temperatures, the exchange of chlorinated acetates, especially $dClAc^-$ and $tClAc^-$, exhibited a more complex behavior as evident from PXRD profiles (figure 3.2), from 8.0^0 to 10.0^0.
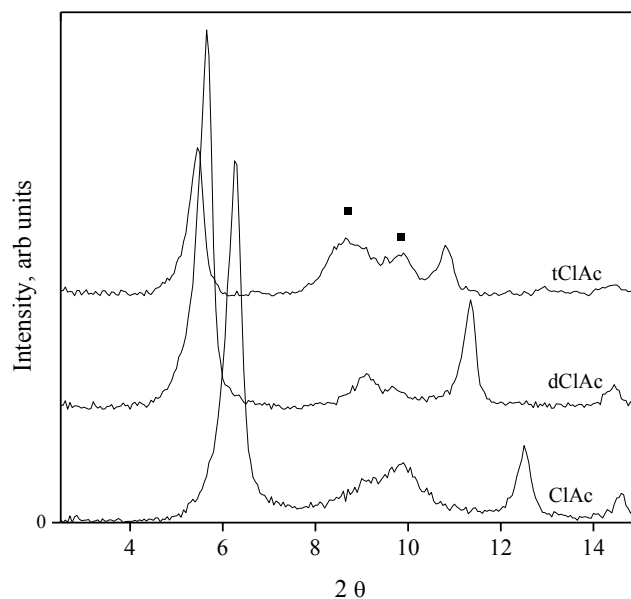
**Figure 3.2. Diffraction patterns for ZnNiH.ClAc, ZnNiH.dClAc and ZnNiH.tClAc.
(▪ refers to peaks due to nitrate diffraction). The materials were exchanged at
30 °C for 24 hrs.**

Deconvolution of these broad features revealed two peaks (figure 3.3), which we

have identified as two nitrate peaks resulting from different conformations. This behavior

implies the formation of two HDS phases. PXRD profiles in figure 3.4A and B, for tClAc

intercalation at 40 °C, reveal how the two nitrate peak intensities changed as a function of

time.
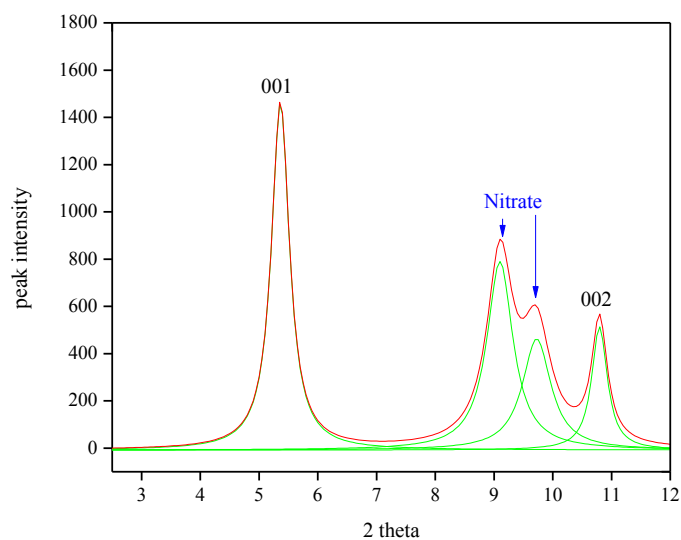
Figure 3.3. PXRD for ZnNiHN after a 5 hour exchange reaction with dClAc at 30 0C. The profile was fit to a Lorentzian function. The 00l peaks are for the dClAc phase.
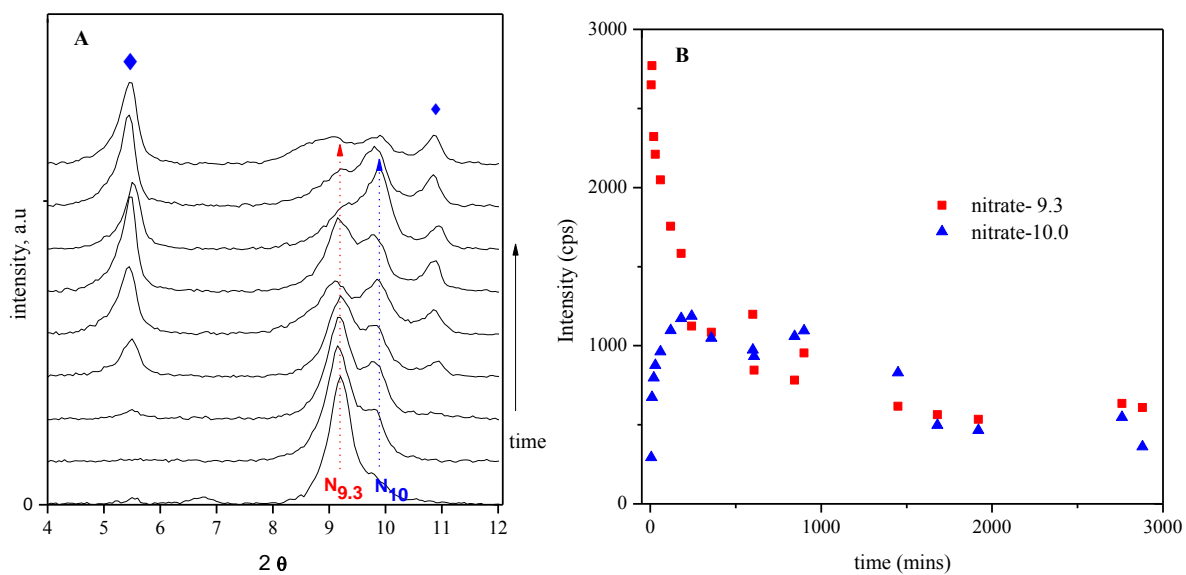
Figure 3.4. (A) Showing stacked PXRD profiles for tClAc intercalation at 40 °C and (B), showing the change in intensity (cps) of the two nitrate peaks at 9.3 and 10.0 °, as a function of time.

It can be observed that while the overall nitrate peak intensity was decreasing, the two peaks at first appeared to be undergoing some antagonistic action, whereby one peak grows while the other one decays. A similar trend was also observed during dClAc intercalation (appendix figure A1-3). From figure 3.4B, it can be concluded that the two nitrates are interacting differently with the metal centers. Two-phased layered metal hydroxides have been reported before, but they appear to be common in nickel based compounds having nitrates as the host anions. HDSs which have two host anion phases have been reported in literature. Rajamathi and Kamath[165], in their work with nickel hydroxy nitrate(NHN), observed that NHN has two isostructural forms; α-Ni(OH)$_2$ and β-Ni(OH)$_2$. The main difference between the two conformers has been reported to be the binding of the nitrates to the layers, which will in turn result in materials with two different interlayer spacings. They also showed that it is possible to transform from one form to the other. Similarly, Taibi and co-workers[7], in their work with nickel-cobalt hydroxy acetate (NiCoAc), observed that NiCoAc can have two different d-spacings, one 11.0 Å wide and the other 12.7 Å wide. They attributed this difference to the nature of acetate-metal bond, which will be different in these two cases. In one scenario, it was reported that, the anion binds to the octahedrally coordinated nickel center and in the other it binds to the tetrahedral coordinated cobalt center. The amount of cobalt in tetrahedral sites and the water molecule organization within the layers were reported to be the other factors influencing the formation of these two structural forms.

In our system, the formation of an additional ZnNiHN peak at 10 ° could be a result of the changing electronic environment within the d-spacing as guest anions are being introduced. The increasing presence of guest anions within the layers will result in

some of the loosely bound nitrates being tightly bound to the layers, while the other nitrates remain as loosely bound or are released into solution. The nitrates which become tightly bound will result in a material with a smaller d-spacing. The FTIR spectra of the ZnNiHN (figure 3.5i) show sharp peaks at 3589, 3581 and 3637 cm^{-1}, which may be attributed to stretching vibrations of the hydroxyl groups not involved in hydrogen bonding. The broad bands in the region 3200-3540 cm^{-1} can be assigned to hydroxyl groups involved in significant hydrogen bonding[180]. For the exchanged products, it is observed that the peaks within the range 3200-3600 cm^{-1} become increasingly broader going from ZnNiH.Ac to ZnNiH.tClAc (figure 3.5ii-v), showing that the extent of hydrogen-bonding is increasing from the Ac to tClAc intercalated compounds. The intense peak at 1352 cm^{-1} and the weak peaks at 1050 and 1450 cm^{-1} in figure 3.5(i) are assigned to nitrate vibrational modes.
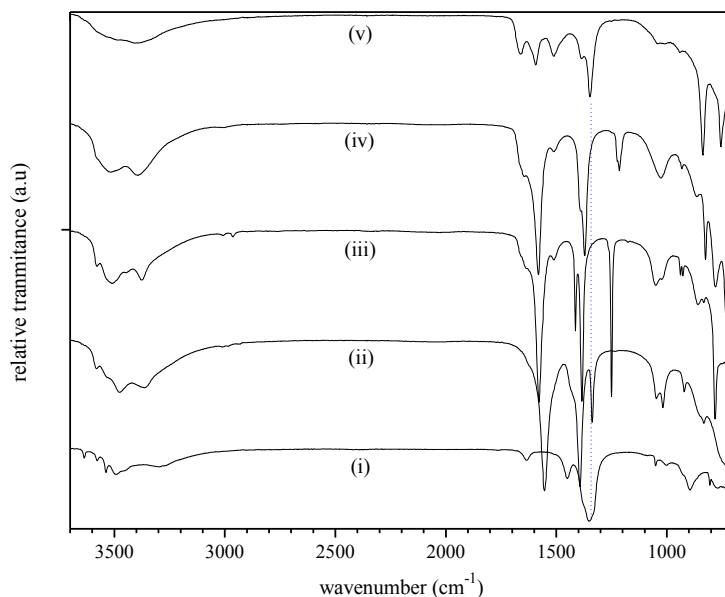
Figure 3.5. FTIR spectra of (i) ZnNiHN and its anion-exchange products; ZnNiH.Ac, ZnNiH.ClAc, ZnNiH.dClAc and ZnNiH.tClAc as (ii-v) respectively.

Vibrational modes of the nitrate ion are of interest because they reveal the symmetry of the ion within the layered structure. The presence of the peaks at 1050 and 1450 cm^{-1} reveals that the nitrate group is in the C_2v symmetry[181], while the weak peak at 1633 cm^{-1} is attributed to water molecules in between the d-spacing or adsorbed on the surface[57]. Nitrate bands disappeared while carboxylate bands emerge, confirming that exchange reactions have taken place, as was observed through PXRD results (figure 3.1). Nitrate bands were not observed for the completely exchanged products. However, in the case of ZnNiH.tClAc, the residual nitrate was observed indicating that it did not exchange to completion even after 54 hrs of reaction at 50 °C. The FTIR spectrum of this tClAc-exchanged product also had a peak at 1348 cm^{-1}, which is the position for the nitrate band. For the exchanged products, very weak peaks are observed within the region 2900 to 3040 cm^{-1}. These peaks indicate the presence of CH (symmetric and asymmetric) bands of Ac, ClAc and dClAc. As expected, CH peaks were not observed for tClAc exchanged product. Strong absorption bands in the region 1360 – 1600 cm^{-1} which are observed for the exchanged products may be assigned to the asymmetric and symmetric vibrations of the carboxylate groups from Ac, ClAc, dClAc and tClAc. The spectral assignments of the bands are presented in table 3.1.

Table 3.1. Wavenumbers of $\nu(CO_2)$ bands and CH bending modes for the exchanged compounds.

Compound	$\nu_{asym}(CO_2)$ /cm^{-1}	$\nu_{sym}(CO_2)$ /cm^{-1}	CH-bending mode /cm^{-1}
ZnNiH.Ac	1554	1391	1338
ZnNiH.ClAc	1579	1383	1250
ZnNiH.dClAc	1580	1373	1215
ZnNiH.tClAc	1594	1385	-

FTIR results confirm the results obtained using PXRD. The main structural differences among the products are observed in the positions of the carboxylate bands, which shifted as the anions changed. The presence of sharp IR peaks at 3585 and 3575 cm^{-1} for figure 3.5(ii and iii) confirms the presence of free hydroxy groups. Intercalation of dClAc and tClAc resulted in a products with intensive hydrogen bonding as evidenced by the presents of broad IR bands in the region starting from 3100-3640 cm^{-1} (figure 3.5 iii-iv). C-Cl bands in the region 700-800 cm^{-1} were observed for the ClAc, dClAc and tClAc products.

3.3.2 Anion release in solution

Reaction progress in the solution phase was monitored by observing the maxima of nitrate bands at 300 nm, which is due to n-π* transitions[182]. The release profiles for the 4 anions were detailed through plots of the percentage (%) nitrate release against time (mins). The (%) of nitrate was calculated by taking the ratio of actual nitrate

concentration at a given time period to the expected nitrate concentration after a complete exchange has taken place. The amount of nitrate released at equilibrium was higher for Ac and ClAc than for dClAc and tClAc. Figure 3.5 reveals that the almost all the nitrates were released from the layered material upon intercalation of Ac and ClAc, even at 24 °C and for very short times. By comparing the amount of nitrates released within 500 mins, it is observed that 96- 99 % nitrates were released when Ac was intercalated. Intercalation of ClAc resulted in a release of 92-99 % nitrates, while 63-85 % and 37-67 % nitrates were released upon intercalation of dClAc and tClAc, respectively. The amount of nitrates released increased as a function of temperature, as is normal for anion exchange reactions. The (%) nitrate released at equilibrium followed the trend: Ac ≈ ClAc > dClAc > tClAc, which is also consistent with the trends inferred from PXRD and FTIR analysis of the solid products. The reduction in amount of nitrates released when more the chlorinated anions were intercalated could be a result of the increasing hydrogen bond network, which might hinder the release of nitrates into solution. For ion exchange to occur, guest ions have to move into the gallery space and travel through this hydrogen bond network; this process will result in breaking and forming some of these hydrogen bonds. This interaction with the hydrogen bond network is expected to be increase as the anions become more chlorinated or larger, resulting in a slower movement and inefficient uptake of the larger anions.
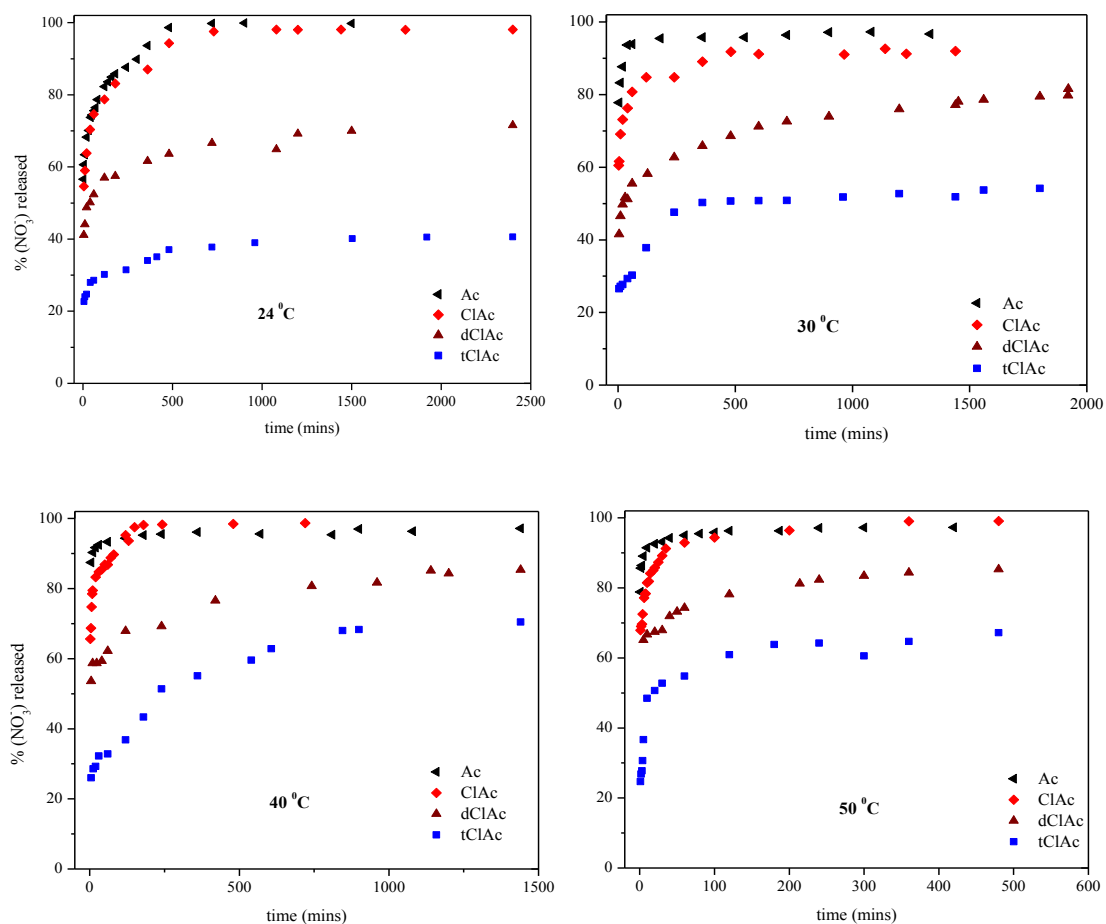
Figure 3.6. Percentage nitrate release upon intercalation of the guest anions at 24, 30, 40 and 50 °C.

Nitrate release profiles for dClAc and tClAc were also different from those of Ac and ClAc profiles. For times less than 300 mins, the nitrate release appears to occur in stages for dClAc and tClAc. At 24 °C, there was an initial release with the two most chlorinated anions which plateaued after about 300 mins and then a second rise was observed at longer times. The same trends were also observed for exchanges at 40 °C. At

50 °C, the same behavior was observed but within 50 mins. These changes occurring in the solution phase are also consistent with the solid phase transformations described previously, see figure 3.4.

3.3.3 Reaction Kinetics and Activation energy determination

In order to gain additional insight into the anion-dependent exchange profiles, kinetics analysis was performed. As was introduced earlier, ion exchange reactions of layered metal hydroxides and other related laminar compounds tend to occur in multiple steps which may give rise to significant dependencies of activation energy on extent of reaction (α)[172]. Isoconversional methods, described in chapter 3.1, were applied to show activation energy changed as a function the extent of reaction (α).
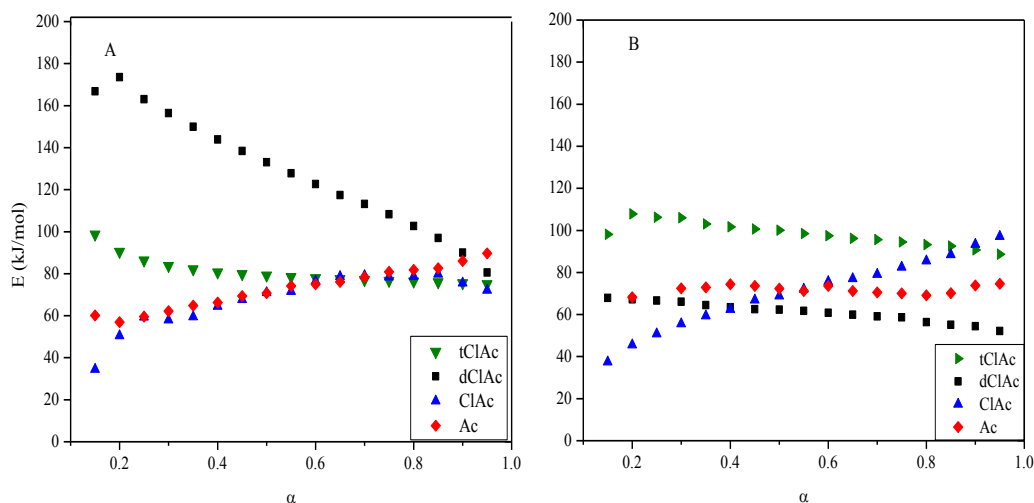
Figure 3.7. E_{iso} dependence on α for the solid (A) and solution (B) phase analyses.

For clarity, the data points in figure 3.7 were presented without their corresponding error bars. E vs α plots with error bars included are shown in the appendix (figure A6-7). The isoconversional activation energies corresponding to the solid phase transformation (figure 3.7A) ranged from 68-74 kJ/mol, 34-97 kJ/mol and 98-89 kJ/mol, for Ac, ClAc and tClAc intercalation, respectively. The corresponding solution phase data shown in figure 3.7B, range from 60-89 kJ/mol, 35-72 kJ/mol and 99-75 kJ/mol for Ac, ClAc and tClAc intercalation, respectively. However, within the experimental error, activation energies did not change significantly. This indicates that the three systems can be described as proceeding via a single mechanism, meaning that a single model, in this case the Avrami Erofev model, can be used to describe the reaction kinetics of these systems. For dClAc intercalation, activation energies ranged from 68to 54 kJ/mol and from 166 to 81 kJ/mol for solid and solution phase changes, respectively. These changes were significant relative to the experimental error, as also shown in the appendix (figure A6-7). This is an indication that the reaction does not proceed via a single mechanism, hence using a model based approach to describe the kinetics will be inappropriate. Activation energy values have been reported to decrease with the extent of reaction when there is a reduction in contribution from a step with the highest activation energy[173]. On the other hand if there is an increase in contribution from the step with the highest energy, activation energies will thus be expected to increase with the extent of reaction. Ion exchange in layered metal hydroxides has been reported to occur layer by layer. The complete replacement of host anions with guest anions within one layer has been reported to cause an increase in the rate of anion-exchange in the neighboring layers, thereby lowering the activation energies as the reaction progresses [87,183]. The high activation

energies observed for tClAc and dClAc systems are similar to those reported in literature in other mechanic studies of HDS exchange reactions[91]. High E_a averaging 60 kJ/mol has been reported for diffusion of ions through polymers[87]. The presence of acetates within the interlayer space creates a dense organic matrix resembling a polymer network consequently affecting E_a. Since the processes involve penetration and diffusion through this organic matter matrix, higher activation energies will thus be expected. Activation energies as high as 100 kJ/mol have been reported in some polymer systems[184]. According to Williams and co-workers[91], diffusion of new guest molecules becomes easier once the layers have been expanded. Since extending the d-space requires energy, it will be expected that larger molecules require more energy to initially separate the layers than smaller molecules[87].

The Avrami-Erofe'ev model has been extensively applied in heterogeneous systems. This model has the advantage of revealing the changes in mechanism as temperature changes. The model, represented in equation 3.1, plots the change in α against time t as shown in the appendix (figure A8-9). The coefficient m gives information about the mechanism and can be used to tell whether the reaction kinetics is governed by diffusion, nucleation or both. Equation 3.3 below is a linearized form of the Avrami Erofe'ev model.

$$\ln\left[-\ln\left(1-\alpha\right)\right] = m\ln\left(t\right) + m\ln\left(k\right) \qquad \textbf{Equation 3.3}$$

Plotting $\ln(-\ln(1-\alpha))$ against $\ln t$ gives a linear plot in which m will be obtained from the slope while k (rate constant) is obtained from the evaluation of the intercept

($m$ln(k). A summary of the dependence of kinetic parameters on anion dimensions and other physical properties are tabulated in table 3.2 and 3.3.

Table 3.2 Dependence of rate constants on anion type and temperature for the solid phase transformation.

Anion	solid phase	
Ac	k (x 10^{-3}s^{-1})	m
24 °C	7 ± 3	0.29 ± 0.02
30 °C	15 ± 5	0.31 ± 0.02
40 °C	26 ± 4	0.33 ± 0.02
50 °C	93 ± 6	0.33 ± 0.03
ClAc	k (x 10^{-3} s^{-1})	m
24 °C	1.0 ± 0.2	0.26 ± 0.06
30 °C	5 ± 1	0.23 ± 0.07
40 °C	11 ± 2	0.22 ± 0.05
50 °C	14 ± 2	0.32 ± 0.07
dClAc*	k (x 10^{-4}s^{-1})	m
24 °C	0.40 ± 0.04	0.32 ± 0.02
30 °C	1.7 ± 0.3	0.31 ± 0.03
40 °C	9 ± 2	0.25 ± 0.04
50 °C	20 ± 2	0.24 ± 0.03
tClAc	k (x 10^{-5}s^{-1})	m
24 °C	0.96 ± 0.04	0.81 ± 0.05
30 °C	4.0 ± 0.1	0.76 ± 0.03
40 °C	7.3 ± 0.2	0.72 ± 0.02
50 °C	14.0 ± 0.8	0.79 ± 0.04

* The α values used for the calculation of the rate constants in this system were from α=0.15-0.6.

Table 3.3.Dependence of rate constants on anion type and temperature for the solution phase.

Anion	solution phase	
Ac	k (x 10^{-3} s^{-1})	m
24 °C	7.7 ± 0.3	0.23 ± 0.01
30 °C	49 ± 3	0.24 ± 0.01
40 °C	54 ± 8	0.26 ± 0.04
50 °C	65 ± 7	0.35 ± 0.04
ClAc	k (x 10^{-3} s^{-1})	m
24 °C	2.0 ± 0.1	0.36 ± 0.08
30 °C	12 ± 1	0.27 ± 0.01
40 °C	30 ± 4	0.29 ± 0.01
50 °C	42 ± 2	0.29 ± 0.02
dClAc*	k (x 10^{-3} s^{-1})	m
24 °C	0.29 ± 0.01	0.31 ± 0.04
30 °C	0.33 ± 0.02	0.22 ± 0.03
40 °C	0.78 ± 0.02	0.28 ± 0.01
50 °C	2.1 ± 0.8	0.28 ± 0.01
tClAc	k (x 10^{-4} s^{-1})	m
24 °C	0.27 ± 0.01	0.20 ± 0.04
30 °C	1.36 ± 0.05	0.35 ± 0.02
40 °C	4.1 ± 0. 1	0.36 ± 0.04
50 °C	23 ± 0. 9	0.31 ± 0.01

* The α values used for the calculation of the rate constants in this system were from α=0.15-0.6.

The Avrami exponents (m) observed for all the anions except tClAc were less than 0.5, which is consistent with diffusion controlled reactions. For tClAc solid phase kinetics, m values were about 0.8, suggesting that there may be some contributions from both diffusion and nucleation processes[15,87]. There is a relation between the kinetic trends summarized in tables 2 and 3 with the computationally calculated physiochemical properties presented in table 4. The electronic spatial extents have an inverse relationship with the observed rate constants. The ratios of anion sizes, which are presented as ESEs are; 1 : 2 : 3 : 4, for Ac : ClAc : dClAc : tClAc, respectively. This ratio is consistent with what is well known in ion exchange processes; that ion size affects the rate exchange. Ions of smaller size have been reported to exchange faster than larger ones,[185,186] provided they are carrying an equal or lesser charge.

Table 3.4. Kinetic data and physical properties of anions involved in exchange at 24 °C.

Anion	ESE	Average oxygen charge	d-spacing (Å)	k (s^{-1}) solid[a]	k (s^{-1}) solution[a]
NO_3^-	205	-	9.5	-	-
$CH_3CO_2^-$	263	-0.67	13.0	$(7 \pm 3) \times 10^{-3}$	$(7.7 \pm 0.3) \times 10^{-3}$
$Cl\text{-}CH_2\text{-}CO_2^-$	596	-0.59	14.4	$(1.0 \pm 0.2) \times 10^{-3}$	$(2.0 \pm 0.1) \times 10^{-3}$
$Cl_2CH\text{-}CO_2^-$	887	-0.54	15.7	$(0.40 \pm 0.04) \times 10^{-4}$	$(0.29 \pm 0.01) \times 10^{-3}$
$Cl_3C\text{-}CO_2^-$	1187	-0.50	16.0	$(0.96 \pm 0.04) \times 10^{-5}$	$(0.27 \pm 0.01) \times 10^{-4}$

[a] only results obtained for exchanges occurring at 24 °C were used because the trends observed were the same for all the temperatures.

The halogen atoms attached to the carbon adjacent to the carboxyl group will pull the electron density away from the carboxyl group, thereby reducing the overall negative charge on the two oxygen atoms. Reducing the electron density from the carboxyl group reduces the overall negative charge on the O atoms. The more Cl atoms there are, the greater the electron-pull and the less negative the O atoms will be. Thus, tClAc with the three Cl atoms will experience the greatest electron withdrawing away from the carboxyl group than all the acids. Individual atomic charges and electronic spatial extents were obtained after optimization of all the structures, with a solvation model IEFPCM at the B3LYP/6-311G + level of theory. The average of the two charges on the oxygen atoms was used for relative comparison among all the acids. We also observed that the average oxygen charges decreased from Ac to tClAc. Since ion exchange reactions are due to electrostatic attractions between positively charged interlayers and negatively charged ions, any decrease in either charge will result in a reduced attraction between the two. The negative charge of the anions decreased from Ac to tClAc, while the positive charge of the layers remained constant. This would mean a weaker electrostatic attraction and possible explanation as to why the rate constants decreased as charges decreased.
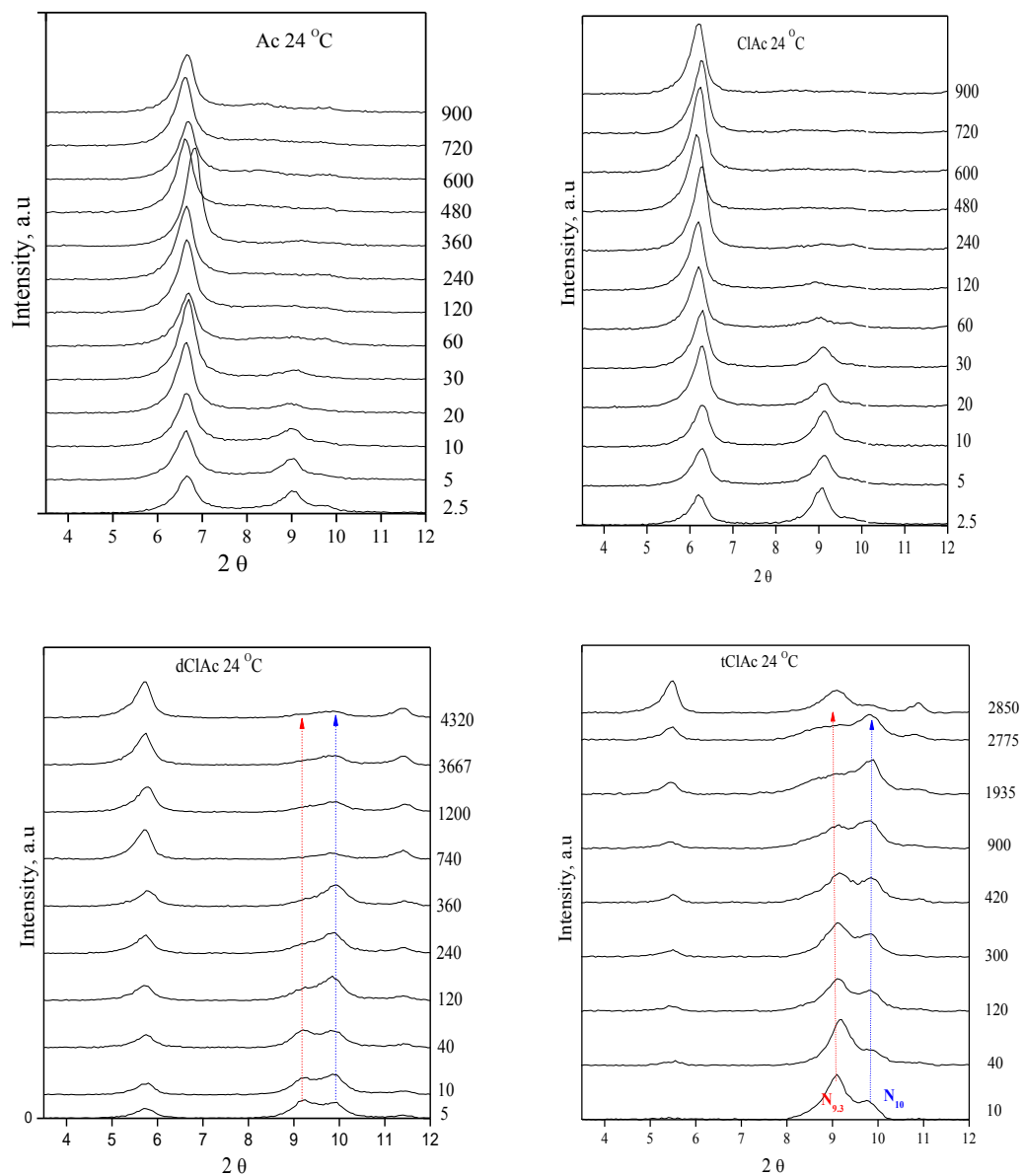
Figure 3.8. Stacked PXRD profiles for reactions at 24 °C for Ac, ClAc, dClAc and tClAc intercalation. Showing increasing reaction times (in minutes), from bottom to the top.
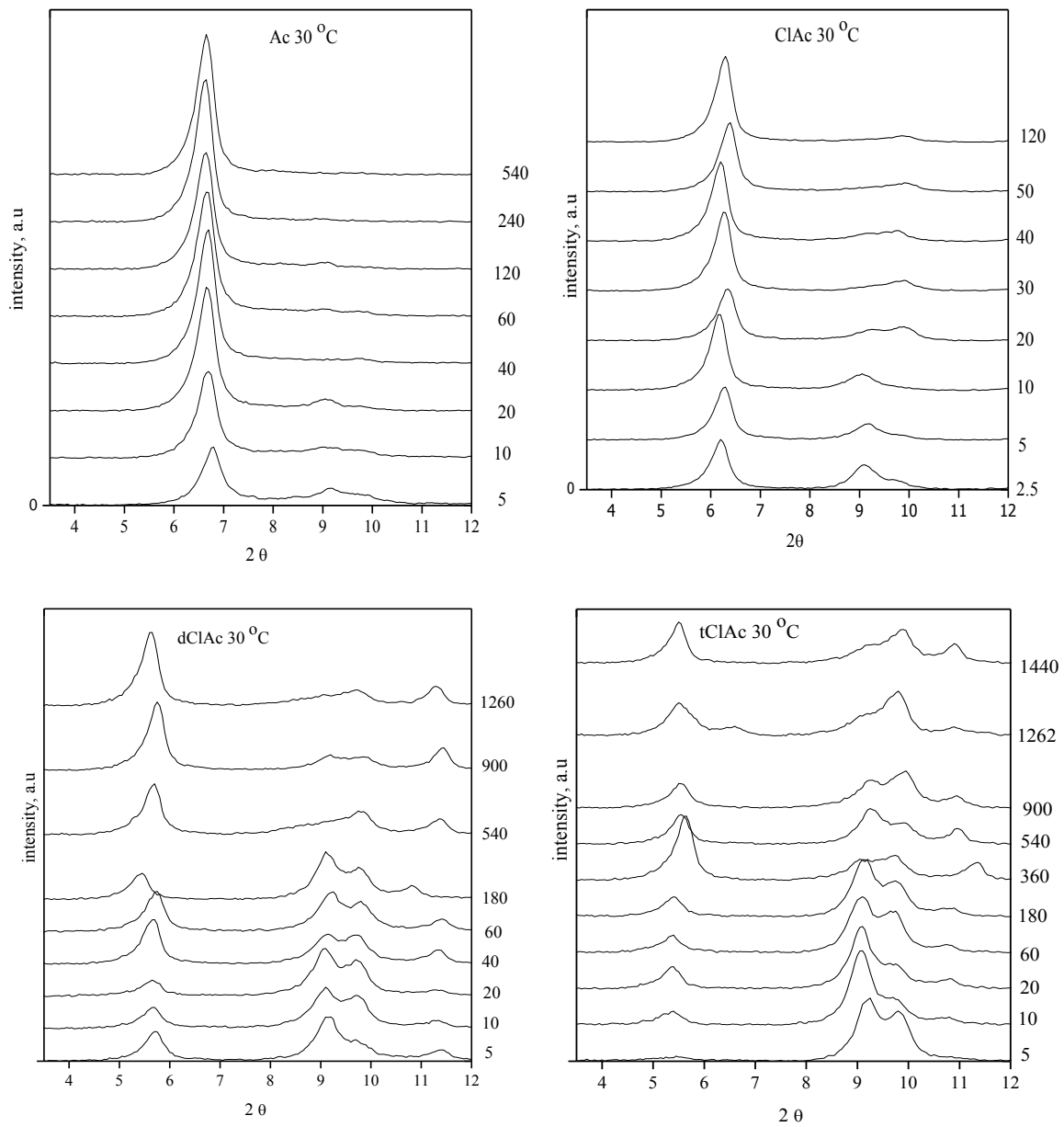
Figure 3.9. Stacked PXRD profiles for reactions at 30 °C for Ac, ClAc, dClAc and tClAc intercalation. Showing increasing reaction times (in minutes), from bottom to the top.
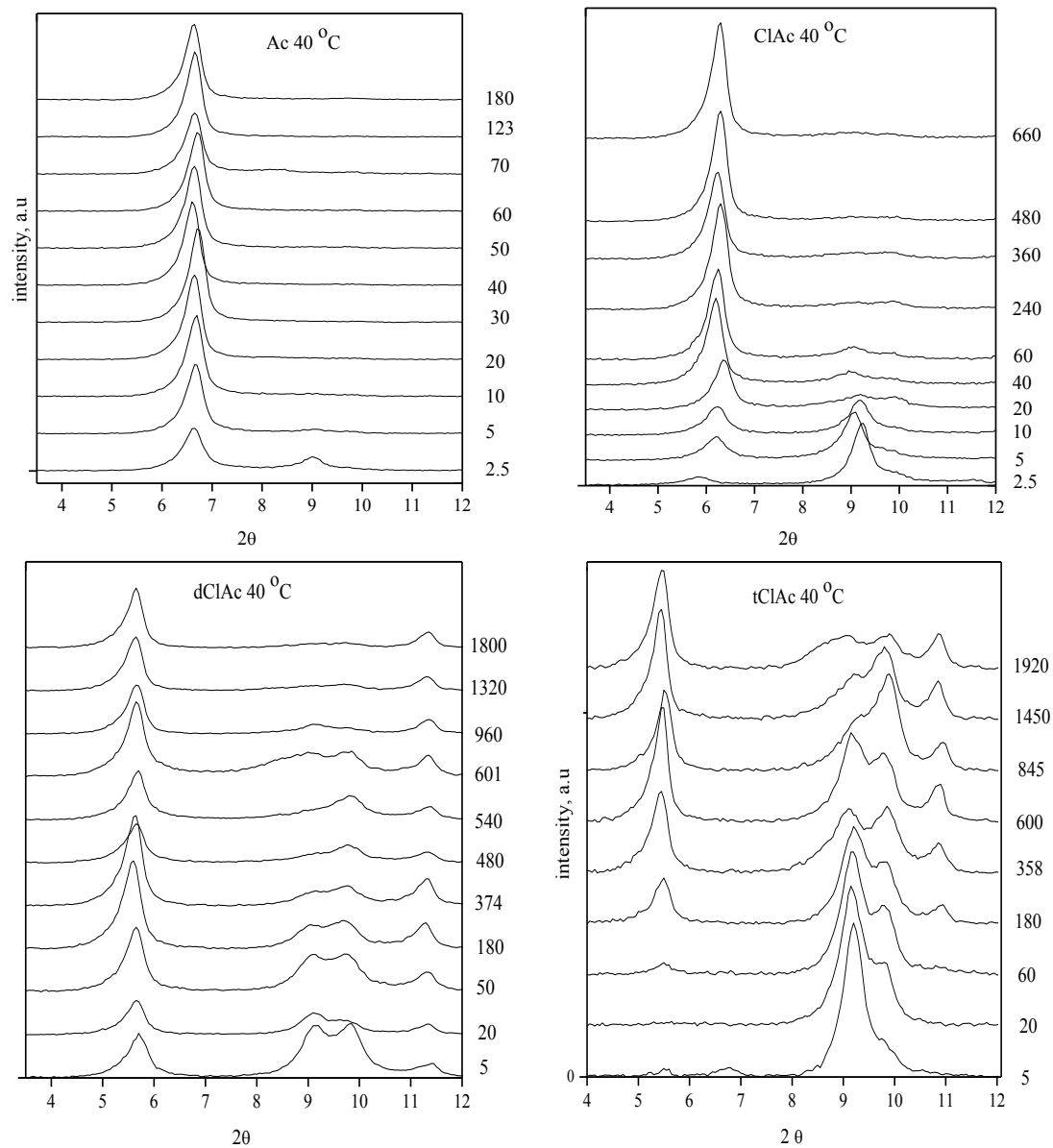
Figure 3.10. Stacked PXRD profiles for reactions at 40 °C for Ac, ClAc, dClAc and tClAc intercalation. Showing increasing reaction times (in minutes), from bottom to the top.
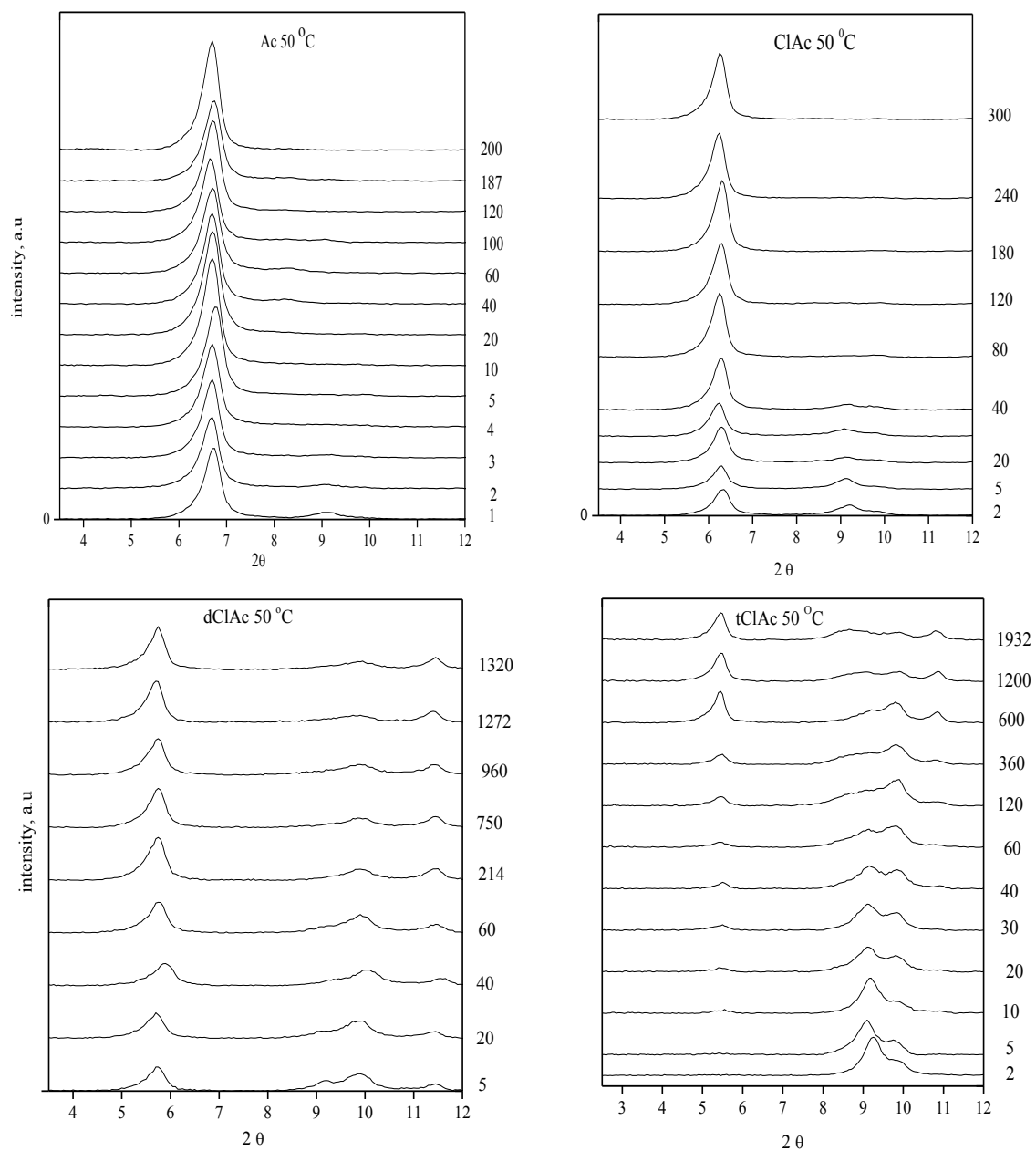
Figure 3.11. Stacked PXRD profiles for reactions at 50 °C for Ac, ClAc, dClAc and tClAc intercalation. Showing increasing reaction times (in minutes), from bottom to the top.

Figures3.8-3.11 shows the temporal solid phase transformations upon intercalation of Ac, ClAc, dClAc and tClAc anions at 24, 30, 40 and 50 ℃. The appearance of a new nitrate peak at higher 2θ values ($\approx 10°$), for dClAc and tClAc, can have an effect on the overall exchange kinetics. Instead of the host ions being immediately released as the guest ions approach; some of the nitrates at $9.3°$ ($N_{9.3}$) were transformed into nitrates at $10°$ (N_{10}). These transformations were more pronounced at 24 ℃ than at 30, 40 and 50 ℃. These two nitrate peaks were also more persistent as the ions became more chlorinated. The appearance of the additional nitrate peak would mean that it was more favorable for the new nitrate interaction to be formed than for complete nitrate release into the solution. The system acted as if it was readjusting itself after a perturbation in the electronic environment. This rearrangement will have an effect on the overall release rates. Since these rearrangements, leading to formation of the two nitrate interactions, persisted longer for tClAc than dClAc, ClAc and Ac, it would explain the reduction in nitrate release rates from tClAc to Ac, for both solid and liquid phases.

For all the anions, we observed that nitrate release into solution occurred faster than the appearance of solid phase products. Such trends are consistent with what has been reported in literature for related systems[87]. The difference between solution analysis and solid state transformations has been reported to be indicative of the loss of the host anion and a subsequent loss of coherent diffraction from the product phase[187]. In other words, the solid phase transformations lag behind the solution phase transformations. The delayed appearance of the guest peak has also been reported to be due to the fact that a certain number of layers have to be filled before any Bragg reflections can be observed[170].

Table 3.5.Arrhenius (E_a) and isoconversional energies (E_{iso}) for the solution and solid phase reactions.

Anion	Solid E_a (kJ/mol)	Liquid E_a (kJ/mol)	Solid phase E_{iso} (kJ/mol)	liquid phase E_{iso} (kJ/mol)
Ac	75 ± 9	55 ± 30	60-89	59 - 82
ClAc	76 ± 24	88 ± 26	34 - 80	38 - 97
dClAc	120 ± 16	63 ± 9	166-81	68 -52
tClAc	76 ± 17	129 ± 13	99-75	107-89

Temperature dependency of these reactions was also evaluated using the Arrhenius plots (appendix, figure A10). The results shown in table 3.5 indicate that the activation energies obtained using a model-fitting approach were comparable to activation energies extracted using a model-free approach. Although the model-fitting approach resulted in a single activation energy value, this value was within the range of energies observed using isoconversional analysis, for both solution and solid phases. Isoconversional approaches have been shown to be superior to model-fitting approaches, since the latter does not reveal the mechanistic changes as a function of the extent of reaction. Without the use of isoconversional analysis, the activation energy trend observed for dClAc systems would not have been revealed.

3.4   Conclusion

The organic guest molecules (Ac, ClAc, dClAc and tClAc) have been

successfully intercalated into the HDS. Complete exchanges have been observed for all

but tClAc. The use of PXRD revealed that the intercalation of the chlorinated acetates

resulted in the formation of two nitrate phases before a complete host anion release was

achieved. The formation of these two phases while guest ions were being intercalated,

instead of them being immediately released, slowed down the release rates. The two

phases persisted longer, the more chlorinated the host anion was. An inverse relationship

was observed between the calculated ESEs and the observed rate constants. The decrease

in rate constants from Ac to tClAc was also attributed to the decrease in the calculated

average oxygen charges, the most negative one exchanged faster. The use of

isoconversional analysis revealed that for all the anions except dClAc, there was no

significant change in activation energy change as a function of α. The average activation

energies for both solution and solid phase analyses were 117 and 103 kJ/mol for dClAc

and tClAc, respectively, while lower values were obtained for ClAc and Ac (36 and 60

kJ/mol, respectively). For dClAc systems a significant activation energy change against

the extent of reaction was observed, indicating that a single model (Avrami model) is

inadequate for modeling the reaction kinetics for the entire extent of reaction.

4.   Effects of metal ion substitution on uptake efficiency

4.1   Introduction

There has been considerable interest in the past decade to find "smart" materials with tunable physical and chemical properties. Hydroxy double salts (HDSs) are among an emerging class of nanostructured materials with potential for use in various applications[6] some of which include, ion exchange reactions,[91,178] as well as in drug and pesticides delivery systems,[163,188] to name but a few. Layered hydroxy salts and hydroxy double salts fall under the classification of anionic clays.[30] These are separated into two structural types, based on the structure of zinc hydroxy nitrate ($Zn_5(OH)_8(NO_3)_2.2H_2O$ or nickel hydroxy nitrate ($Ni_2(OH)_3NO_3.H_2O$).[13,17] A quarter of octahedral sites in the hydroxide layers of $Zn_5(OH)_8(NO_3)_2.2H_2O$ are vacant and the Zn^{2+} ions occupy the tetrahedral sites on either side of the vacant octahedral sites. The positive layers of $Zn_5(OH)_8(NO_3)_2.2H_2O$ can be represented with the composition $[Zn_3\square Zn\square_2(OH)_8]^{2+}$, where Zn is in octahedral site, $\square$ is a vacant octahedral site and $Zn\square$ is tetrahedrally coordinated.[16] The positive charge is compensated by incorporation of anions into the gallery space. In $Ni_2(OH)_3NO_3.H_2O$ a quarter of the hydroxide ions are replaced by nitrate ions which are coordinated directly to the metal matrix.[189]

Knowledge of the factors that govern these exchange reactions is crucial for tailoring materials targeted for specific applications. Ion exchange reactions in layered metal hydroxides have been widely studied,[190] but despite all these studies, very little is still known about the fundamental thermodynamic and kinetic properties of these

exchange processes[191]. Solid state exchange processes are heterogeneous in nature, but most of the investigations reported in literature focuses on either the solid phase transformations or the change in solution composition, with no reported concurrent *in sit* studies on both solution and solid phases to date.[87]

In this study we focused on *ex sit* analysis of both solution and solid phases, in an effort to unravel the factors controlling these exchange reactions. Powdered X-ray diffraction (PXRD) has been utilized to acquire ex-situ kinetic data on the solid phase transformations, while HPLC has been used for probing concentration changes in the solution. The data obtained from these two techniques provides a complementary view of the kinetics and helps provide insight into the potential reaction mechanisms. The Avrami-Erofe'ev model[87,94,192], described in section 1.4, was applied for data modeling. The kinetic parameters extracted from the double logarithmic plots were used for the comparison of the release reactions of the three materials[170].

The goal of this study was to determine the release and uptake kinetics of acetate/nitrate anions from a series of HDSs and LHSs. By analyzing ion exchange kinetic properties of a series of HDS and LHS compounds, we will be able to reveal the structural features of these compounds that affect uptake and release of anions. Differences in properties such as charge density of the cations, inter-layer hydrogen bonding, or the nature of interactions between anions and the hydroxide layers can also be explored and used for explaining the release and uptake behavior of these compounds. Ten compounds listed below were synthesized:

(i)   zinc-copper hydroxy acetate (ZnCuHAc)

(ii)   zinc-nickel hydroxy acetate (ZnNiHAc)

(iii)   zinc hydroxy acetate (ZnHAc)

(iv)   copper hydroxy acetate (CuHAc)

(v)   zinc cobalt hydroxy acetate (ZnCoHAc)

(vi)   zinc hydroxy nitrate (ZnHN)

(vii)   copper hydroxy nitrate (CuHN)

(viii)   zinc-nickel hydroxy nitrate (ZnNiHN)

(ix)   zinc-cobalt hydroxy nitrate (ZnCoHN)

(x)   zinc-copper hydroxy nitrate (ZnCuHN)

4.2   Experimental

4.2.1   Materials

Copper acetate monohydrate, (98 %) [$Cu(CH_3COO)_2.H_20$], zinc acetate, (99.9 %) [$Zn(CH_3COO)_2$], zinc oxide (+ 98%) [ZnO] were used as obtained from Sigma Aldrich Chemical Co. Sodium hydroxide pellets, (99 %) [$NaOH$] was obtained from J. T. Baker. Nickel nitrate hexahydrate, (+98 %) [$(Ni(NO_3)_2.6H_2O)$], zinc nitrate hexa-hydrate [$(Zn(NO_3)_2.6H_2O)$], copper nitrate, (98 %) [$(Cu(NO_3)_2)$ $2.5H_2O$], and cobalt nitrate hexa-hydrate, 98 % [$(Co(NO_3)_2.H_2O$] were obtained from Alfa Aesar Co. Acetic acid (99.9%) was obtained from DBH.

4.2.2 Synthesis

The precursor HDSs were prepared according to methods listed below.

(i)   ZnNiHAc was synthesized using the ion exchange method by reacting ZnNiHN

and 0.2 M NaAc at room temperature for 12 hrs. The product was washed using de-

ionized water and dried at room temperature for 24 hrs.

(ii)   ZnCuHAc was prepared by adding 0.41 g ZnO (5 mmol) to 1.00 g of copper

acetate monohydrate (5 mmol) in 10 ml of deionized water followed by vigorous shaking

for about 20 mins. The green suspension was allowed to stand for 24 hrs and then

filtered. The remaining solid was washed several times with deionized water and then

dried at room temperature for 24 hrs.

(iii)   ZnHAc was prepared by the titration method. 50 ml of a 0.75 $mol\,L^{-1}$ sodium

hydroxide was added dropwise to 20 ml of 3.5 $mol\,L^{-1}$ zinc acetate dihydrate aqueous

solution at room temperature. The white precipitate was filtered, washed several times

with deionized water and dried at room temperature for 24 hrs.

(iv)   CuHAc was synthesis by slowly adding equimolar amounts 0.10 $mol\,L^{-1}$ sodium

hydroxide solution and 0.10 $mol\,L^{-1}$ copper acetate monohydrate solution. The resultant

blue-green solid suspension was filtered, washed several times with deionized water and

ethanol and then dried at room temperature[193].

(v)   ZnCoHAc was synthesized using the ion exchange method by reacting ZnCoHN

and 0.2 M NaAc at 30 °C for 24 hrs. The product was washed using de-ionized water and

dried at room temperature for 24 hrs.

(vi) CuHN, 50g $Cu(NO_3)_2$ was dissolved in 0.5 L of distilled water followed by the addition of aqueous ammonia until the pH was equal to 8.0 ± 0.1. the precipitate was aged at room temperature for 24 hrs, then washed, filtered and dried at room temperature[194].

(vii) ZnCoHN, 60 ml of 1 M $Co(NO_3)_2$ solution (=0.06 mol) was added to 9.8 g of ZnO (=0.12 mol) dispersed in a few ml of water. The dispersion was allowed to stand for 6 days at 65 °C, followed by filtration, washing and drying at 65 °C.

(viii) ZnNiHN, 29.0 g $Ni(NO_3)_2.6H_2O$ were mixed with 16.8 g ZnO in 120 ml de-ionized water. The mixture vigorously was shaken for about 15 mins, and then allowed to stand in a water bath at 60 °C for 6 days. The resultant green precipitate was vacuum-filtered, washed using deionized water and then allowed to dry at room temperature for 24 hrs.

(ix) ZnHN, 18.94 g $Zn(NO_3)_2.6H_2O$ was dissolved in 100 ml de-ionized water followed by the addition of 8.1 g ZnO into the same solution. The white mixture was continuously stirred for 10 mins and allowed to stand for 24 hrs at room temperature. The white precipitate was filtered, washed and dried for another 24 hrs at room temperature.

(x) ZnCuHN, 9.8 g of ZnO was mixed with 100 ml of 1 M $Cu(NO_3)_2$ solution. The mixture was aged for 72 hrs at 65 °C. The mixture was decanted to retain only the solid, which was again added to a fresh solution of 30 ml 1 M $Cu(NO_3)_2$. After three more days, the solid was filtered and washed using de-ionized water. The solid was dried at 40 °C in air for 24 hrs[178].

4.2.3 Characterization

The released acetate concentration was measured using HPLC on a Shimadzu LC-20AT machine with an SPD 20A Prominence UV-VIS detector. A Supelco Discovery C_{18}; 25 cm x 4mm x 5 μm column was used for the separation. An 8 mmol L^{-1} Na_2SO_4: 1 mmol L^{-1} H_2SO_4 solution was used as the mobile phase at a flow rate of 1 ml/min. Sample injection volumes were 20 μL and the analysis was done at wavelength of 210 nm. The acetate calibration curve was determined in the presence of sodium nitrate concentrations identical to those used in the exchange reactions. The extent of reaction (α) was obtained from the concentration of acetate at time t, C_t, and at equilibrium, C_{eqm}.

$$\alpha = \frac{C_t}{C_{eqm}}$$ **Equation 4.1**

Solid phase reaction kinetics were followed using a Rigaku Miniflex II diffractometer using Cu Kα (λ= 1.54 Å) radiation source at 30 kV and 15 mA. The patterns were recorded from 2θ value of 2.0° to 40.0°. The diffractometer was calibrated using a silicon reference material (RSRP-43275G; provided by Rigaku Corporation) and the powder samples were pressed into the trough of glass sample holders for analysis. The intensity of Bragg reflections corresponding to the 001 peak of both the guest and host anions was used for the determination of α. The profiles were first baseline-corrected and then fit to a Gaussian function before intensities could be used in the determination of α, using equation 4.3 below.

$$\alpha_{g(t)} = \frac{I_{g(t)}}{I_{g(t)} + I_{h(t)}}$$

Equation 4.2

where $I_{g(t)}$ is the intensity of the guest peak while $I_{h(t)}$ is the intensity of the host peak.

FTIR spectra of the precursor and their exchanged products were obtained on a Perkin Elmer Spectrometer 100 FT-IR operating at a resolution of 2 cm^{-1} in the 4000-650 cm^{-1} spectral range. A single reflection ATR accessory with a ZnSe prism (PIKE MIRacle, from PIKE Technology) was used for recording the spectra. Thermogravimetric analysis was performed on a Netzsch TG 209 F1, TGA instrument. Aluminum oxide crucibles were used for containing the samples, and heating was done under a constant flow of nitrogen at a heating rate of 20 °C/min from 40 °C to 700 °C.

The elemental analysis was done in three parts. Metal analysis was performed using a Perkin Elmer A Analyst 100 Atomic Absorption Spectroscopy instrument. 0.25 g of each HDS were dissolved in 15 ml of 6 mol L^{-1} HCl and then diluted to 50 ml into a volumetric flask using deionized water. The stock solution used for making the calibration curve for copper concentration was obtained by dissolving pure copper powder in 6 mol L^{-1} HCl and then diluted using deionized water. The same procedure was used for the zinc calibration curve. Zinc quantification was done using a zinc hollow cathode operating at a current of 12 A, wavelength of 213.9 nm, width of 0.7 and an integration time of 2 seconds. Copper analysis was done using a copper hollow cathode at a current of 25 A, wavelength of 324.8 nm, width 0.7 and an integration time of 2 seconds. HPLC was used for acetate quantification from the same dissolved samples used above. The chromatographic method used was the same as described in section 2.2.1. Sodium acetate was diluted in 0.1 mol L^{-1} HCl was used as the stock solution for the

calibration curve. Hydroxide quantification was done using a dissolution titration. 0.25 g of the HDS was mixed with 25 ml of deionized water and mixed thoroughly into slurry which was then titrated with standardized 1 mol L^{-1} HCl solution. Since this dissolution titration gives both the hydroxide and acetate concentration in the compound, acetate concentration obtained from HPLC analysis was then subtracted from the titration obtained value to give the absolute hydroxide concentration. The waters of hydration were obtained from TGA analysis and the results are shown in the Appendix B2. The obtained formulae for ZnCuHAc, CuHAc and ZnHAc were:

$ZnCu_{2.8}(OH)_{5.4}(CH_3COO)_2.2.H_2O$, $Cu_{2.1}(OH)_{3.3}(CH_3COO). H_2O$ and

$Zn_{5.1}(OH)_8(CH_3COO)_2.4H_2O$ respectively. The formulae for the corresponding exchange products are $ZnCu_{2.8}(OH)_{5.7}(NO_3)1.9.H_2O$, $Cu_2(OH)_3(NO_3). H_2O$ and

$Zn_{2.5}(OH)_4(NO_3).3H_2O$. Calibration curves for the analyses are shown in Appendix B1.

4.2.4   Exchange reaction kinetics.

Acetate and nitrate based materials were reacted with sodium nitrate and sodium acetate solutions, respectively. Some materials reacted with the guest anions solutions while others did not. Kinetic studies were then conducted on materials that reacted. Release kinetics of the host anion was conducted on CuHAc, ZnCuHAc and ZnHAc. The reactions were conducted at 5 different temperatures; 30, 35, 40, 45 and 50 °C. The exchange reactions were performed in a shaking water bath at 300 strokes/min. Samples were prepared by adding 0.15 g of the precursor HDS to 15 ml of 0.035 M NaNO$_3$ in 50 ml glass vials. The suspensions were continuously stirred in the water bath at a constant

temperature and then quenched by filtration after a specific time period. The solid

samples were washed with deionized and allowed to dry at room temperature for 24 hrs.

4.3   Results and Discussion

Preliminary tests to ascertain the feasibility of the exchange reactions were

conducted by reacting 0.15 g of the HDSs with 0.035 M nitrate/acetate solution at room

temperature for 24 hrs. PXRD data of the pristine HDSs and their exchange products was

used to confirm the exchanges, the results are shown below.
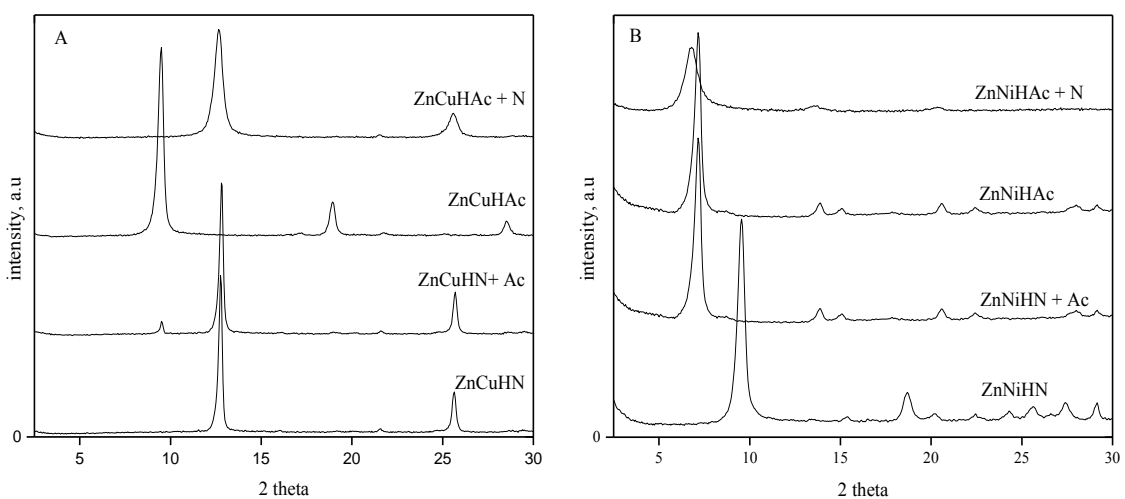
Figure 4.1.PXRD profiles for starting materials and the exchange products of (A) Zn-Cu and (B) Zn-Ni-HDSs.For both figures A and B, the profiles at the bottom (ZnCuHN and ZnNiHN) were reacted with Ac to produce the profiles second form the bottom ((ZnCuHN + Ac) and (ZnNiHN + Ac), respectively).The same is true for ZnCuHAc and ZnNiHAc (third and four profiles).
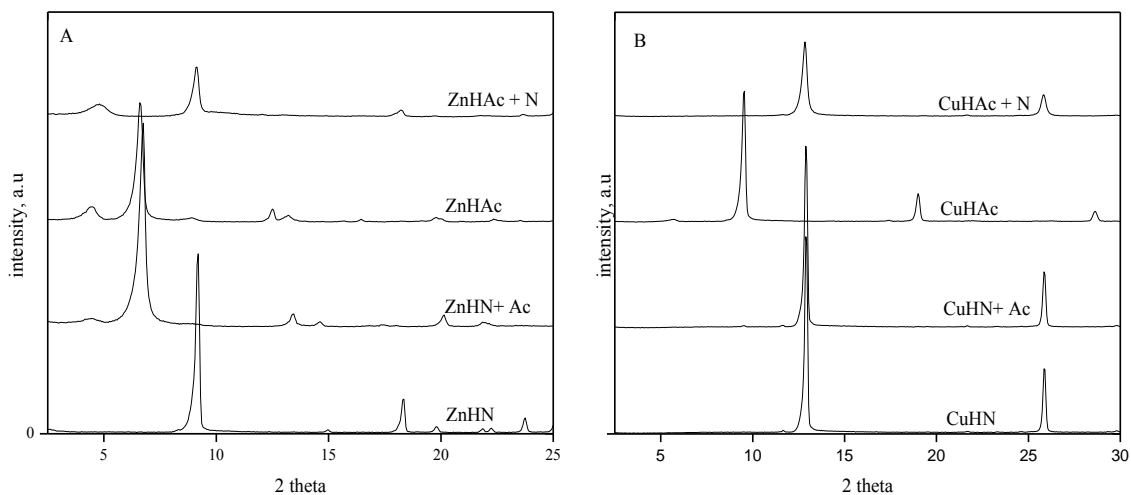
Figure 4.2. PXRD profiles for starting materials and the exchange products of (A) Zn and (B) Cu-HDSs.For both figures A and B, the profiles at the bottom (ZnHN and CuHN) were reacted with Ac to produce the profiles second form the bottom ((ZnHN + Ac) and (CuHN + Ac), respectively). The same is true for ZnHAc and CuHAc (third and four profiles).
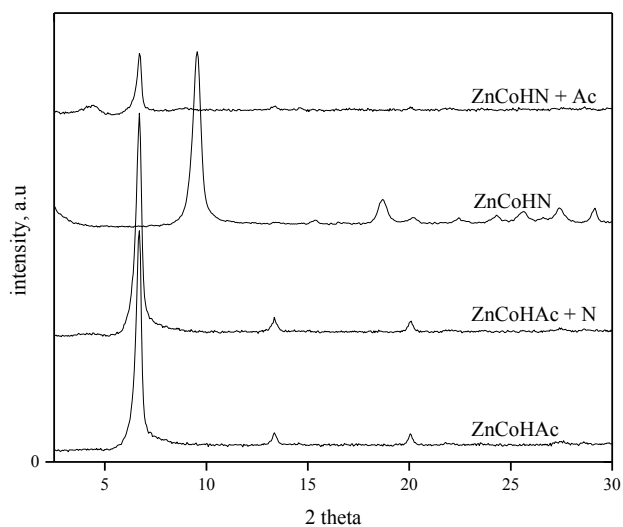
Figure 4.3.PXRD profiles for starting materials and the exchange products of Zn-Co-HDSs.

The results shown in Figure 4.1 to 4.3 are summarized in table 4.1 below. All the exchanges were done at 24 °C for 24 hrs, with continuous stirring. PXRD results of the precursor nitrate and acetate based compounds and their exchange products, shown in Figure 4.1, show features typical of ordered lamellar compounds, consistent with brucite-like layered compounds.[32,57,162] In all cases, the materials show intense 00l reflections which are equally spaced indicating layered structures and possess high range ordering, at least to the third order in the c axis direction. In order to explore ion-exchange properties of these compounds, preliminary reactions were conducted whereby acetate-based compounds were reacted with nitrate ions while nitrate based compounds were reacted with acetate ions for 24 hrs at 24 °C. For the reactive nitrate based compounds, there was a shift towards lower theta values, suggesting that an expansion of the d-spacing has occurred. Reactive acetate compounds resulted in the formation of compounds with smaller d-spacings, a change consistent with the intercalation of guest anions (NO_3^-) smaller than the host anions (Ac^-).

Table 4.1.Nitrate-based HDSs reactions with acetates (left) and the reverse reactions (right).

	HDS material	reaction with Acetate	HDS material	reaction with nitrate
1	ZnHN	reacted	ZnHAc	reacted
2	CuHN	no reaction	CuHAc	reacted
3	ZnCuHN	no reaction	ZnCuHAc	reacted
4	ZnNiHN	reacted	ZnNiHAc	no reaction
5	ZnCoHN	reacted	ZnCoHAc	no reaction

Table 4.2. Precursor materials and their d-spacing.

	HDS material	d-spacing[a]	
1	ZnHN	9.60	$(9.72)^{17}$
2	CuHN	6.85	$(6.93)^{56}$
3	ZnCuHN	6.94	$(6.96)^{178}$
4	ZnNiHN	9.21	$(9.21)^{100}$
5	ZnCoHN	9.25	$(9.68)^{178}$
6	ZnHAc	13.08	$(13.2)^{161}$
7	CuHAc	9.30	$(9.44)^{13}$
8	ZnCuHAc	9.30	$(9.44)^{189}$
9	ZnNiHAc	12.35	$(12.8)^{161}$
10	ZnCoHAc	13.18	$(13.1)^{161}$

[a]the values in parentheses are literature values for the same compounds.

From PXRD figures 4.1 to 4.3, and also table 4.1, it is revealed that only ZnHN, Zn-NiHN and Zn-CoHN (nitrate series) reacted with acetate anions, while CuHN and ZnCuHN were unreactive. The inter-layer spacings of all the materials are comparable to those reported in earlier studies as shown by the values in parentheses. For the acetate series, only ZnHAc, ZnCuHAc and CuHAc were reactive, while ZnNiHAc and ZnCoHAc were not. With the exception of ZnHN and ZnHAc, compounds which were reactive in the nitrate form were unreactive in the acetate form, and vice versa. The d-spacings shown in table 4.2 reveal that there are some significant structural differences among five nitrate-based compounds. ZnCuHN and CuHN have d-spacing equal to 6.9 Å, while the d-spacings for ZnHN, ZnNiHN and ZnCoHN are 9.6, 9.2 and 9.3 Å, respectively. The structure of $Cu_2(OH)_3NO_3.H_2O$ has been reported to be similar to that of $Ni_2(OH)_3NO_3.H_2O$ which has its nitrate ions grafted to the hydroxide layers,[189] resulting in a smaller d-spacing as compared to the other HDSs and LHSs of the $Zn_5(OH)_8(NO_3)_2.2H_2O$ type. Xue et al.[195] synthesized zinc-copper hydroxy sulphate

(ZnCuHS), and characterized it as being of similar structure to $Cu_2(OH)_3NO_3.H_2O$. The non-reactivity of CuHN and ZnCuHN is thus consistent with observed interlayer spacings; grafted or bound anions are expected to be difficult to exchange than unbound anions. It is also expected for materials with unbound anions to be having a wider interlayer space. The reaction of ZnCuHN with acetate anions (see Figure 4.1), reveals that the nitrates in this compound can be partially exchanged with acetates; a small peak corresponding to the acetate phase was observed at 9.5 °. Newman and Jones[17] observed that although nitrate groups are bound to the hydroxide matrix, the strength of their interaction with the layers vary from material to material. It was reported the nitrate groups in $Ni_2(OH)_3NO_3.H_2O$ interact strongly with hydroxide matrix than those in $Cu_2(OH)_3NO_3.H_2O$, hence under different reaction conditions $Cu_2(OH)_3NO_3.H_2O$ could be reactive.

The interlayer spacings of the acetate based compounds also indicate that there are two groups within this series; ZnHAc, ZnNiHAc and ZnCoHAc (with d-spacings equal to 13.08, 12.45 and 13.18 Å, respectively) are in one group, while CuHAc and ZnCuHAc (with d-spacings equal to 9.30 Å) are in the other. Preliminary exchange reactions revealed that only ZnNiHAc and ZnCoHAc were unreactive. The hydroxide layer is approximately 5.2 Å thick, while the length of the acetate anion may be estimated to be ca. 3.6 Å[180] (see Figure 4.4),giving an approximate d-spacing of around 9 Å. The observed d-spacings for ZnHAc, ZnNiHAc and ZnCoHAc, which are more than twice the size of the acetate anion, would suggest that the anions are arranged in a bilayer instead of a monolayer arrangement, as shown in Figure 4.5. The d-spacings observed for

CuHAc and ZnCuHAc are consistent with anions assembled in a monolayers

arrangement.
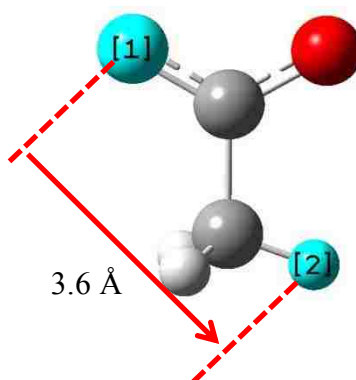
Figure 4.4. An optimized structure of the acetate anion, showing the distance between the one of the O atoms and the furthest H atom.
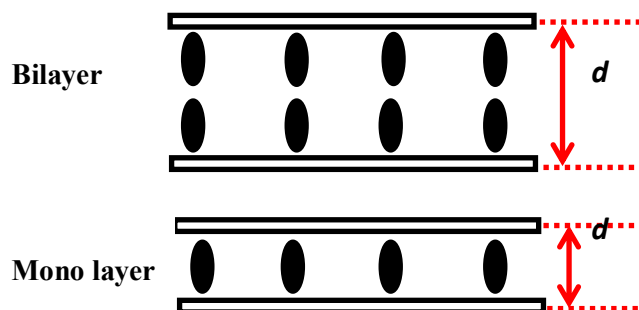
Figure 4.5. A representation of the monolayer and bilayer arrangement of anions within the d-spacing.

4.3.1 FTIR - Nitrate Compounds
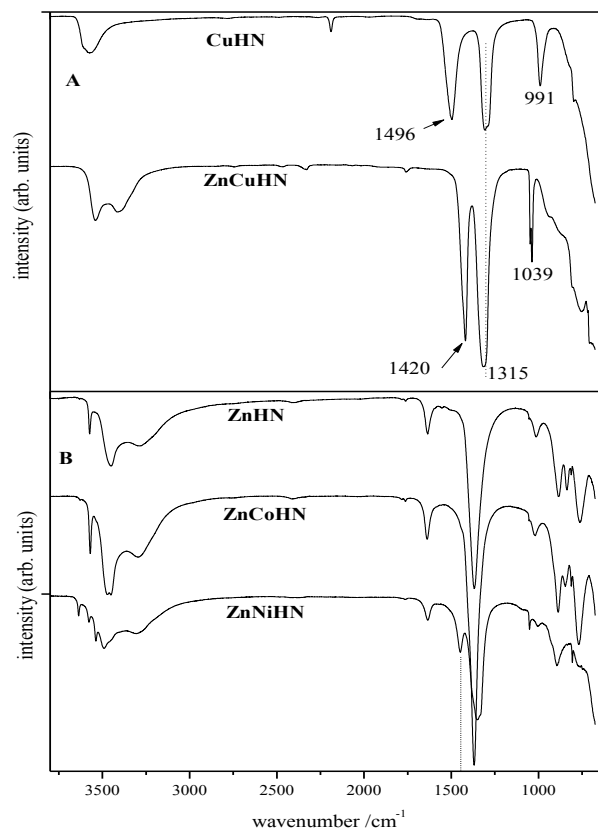
Figure 4.6. FTIR spectra of synthesized nitrate-based HDSs.

To explain some of the observed trends we collected the FTIR spectroscopy data of all the HDSs, and the results are depicted in Figure 4.6(A) and (B). From FTIR spectra, we separated the five nitrate-based compounds into two groups; the ones on top (Figure 4.6A), which did not react and the ones on the bottom (Figure 4.6B), which reacted. There are two regions of interest; (a) 1300-1500 cm^{-1} and (b) 2900-3600 cm^{-1}.

By first focusing on the region 1300 – 1500 cm^{-1}, it can be seen that the nitrates in these groups exhibit two different binding interactions. For the non-reactive compounds, two bands of comparable intensity are observed, which is consistent with bound nitrates, while the single intense peak in figure 4.5 B, at about 1362 cm^{-1}, is consistent with free or unbound nitrates. Free nitrates are known to have a D_3h point group symmetry,[77,190] while bound nitrates can either be in a C_2v or C_s symmetry.[196] It is however difficult, to separate structures exhibiting C_2v symmetry from those showing C_s symmetry using vibrational spectroscopy since the symmetry of the nitrate differs very little between the two.[197] X-ray crystallography can be applied to successfully differentiate between the two.[198] the C_2v or C_s symmetry observed for CuHN and ZnCuHN compounds confirms what has already been observed through PXRD data, that the nitrate ions are grafted into the hydroxide layers. Comparing the FTIR spectra for ZnCoHN, ZnHN and ZnNiHN it can be suggested that the three are related. However, the presence of a small peak (marked by a dotted line) at 1436 cm^{-1} would suggest that ZnNiHN is also, to small extent, related to CuHN and ZnCuHN. It would thus be suggested that ZnNiHN possesses both bound and unbound nitrates, but mostly the unbound nitrates. The region 2900-3600 cm^{-1} has information about CH and OH stretches and reveals the nature of binding interactions of hydroxyl groups.[100] Broad bands are observed for the non-reactive compounds while several sharp peaks are observed for the reactive materials. The broad peaks indicate that the hydroxy groups are experiencing intense hydrogen bonding,[87] while sharp peaks show that some of the hydroxyl groups are free. Broad bands are only observed for the CuHN and ZnCuHN compounds. Since CuHN and ZnCuHN have their nitrates grafted into the hydroxide layers, resulting in the layers coming closer together, it

would be expected that the nitrates which are now in close proximity to the hydroxyl groups will form stronger H-bonds with them. Also the monolayer arrangement of the anions in CuHN and ZnCuHN will force water molecules are anions to be closer to the layers than in a bilayer assembly, thus favoring stronger H-bond interaction. For exchange reactions to be successful, for CuHN and ZnCuHN, the guest anions will have to go through the intense H-bond network and displace grafted nitrate anions. The other compounds, ZnNiHN, ZnHN and ZnCoHN, had weaker H-bonding network and the nitrates appear unbound. Therefore, successful exchange of nitrate with acetate appears to be facilitated by the nature of the interaction of the host nitrate with the positive layers and also the extent hydrogen bonding within the entire system.

4.3.2   FTIR - Acetate compounds.
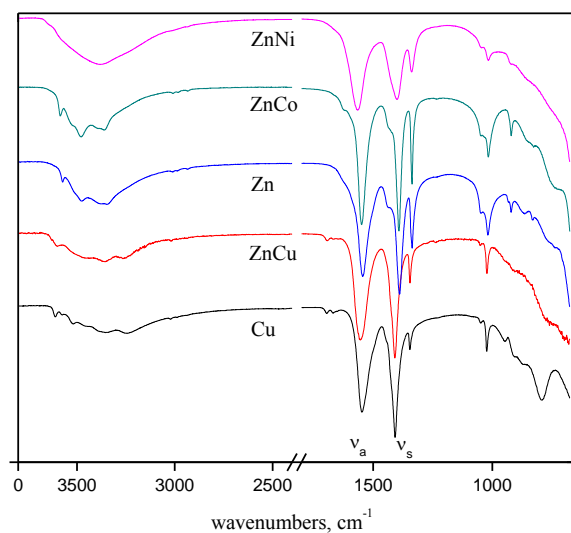
Figure 4.7. FTIR spectra for Cu, ZnCu, Zn, ZnCo and ZnNi-hydroxy acetate.

Unlike a nitrate, a carboxylate ion (RCO_2^-) has low symmetry and different types of carboxylate coordinations cannot be distinguished on the basis of the number of infrared vibrations. However, attempts have been on relating C-O stretching frequencies to the nature of the anions coordination.[75,199] In many cases, the proposed coordination or critical comments on them are based on a relatively small number of complexes, the structures of which have often not been determined crystallographically; hence a more definitive evaluation is needed. Carboxylate ions are known to coordinate to metal centers in the following modes[75]:

      i.   Unidentate complexes.

      ii.   Chelating (bidentate) complexes.

      iii.   Bridging complexes.

Using Nakamoto rules, unidentate complexes have been report to exhibit Δv values $[v_a(CO_2^-) - v_s(CO_2^-)]$ which are much greater than ionic complexes, while chelating complexes exhibit Δv values less than ionic values.[189,197] The Δv values for bridging complexes are greater than those of the bidentate complexes, but close to the ionic values. In this work we observed that Δv values had a general increasing trend, from CuHAc to ZnNiHAc, although there is a small difference in Δv values (± 3 cm^{-1}) for ZnNi, ZnCo and ZnHAc, which could also be due to different metal identities rather than changing carboxylate coordination. The FTIR data for the three materials is summarized in table 4.2. ZnNiHAc synthesized by Ricardo et al.[100] had a Δv equal to 166 cm^{-1}, of which they attributed to an acetate ion in monodentate coordination. The Δv values for CuHAc (140 cm^{-1}) and ZnCuHAc (145 cm^{-1}) differ significantly from the other three materials. The values FTIR spectra observed for CuHAc was similar to that obtained by Masciocchi et

al.[193] and also Jirnenez-Lopez et al.[200], who all reported a Δv value of 140 cm^{-1}. According to these two references, the observed Δv is characteristic of a bridging carboxylate ligand. ZnCuHAc synthesized by Rajamathi et al.[189] also had Δv equal to 140 cm^{-1}, although they did not assign acetate coordination in their material; we attribute this Δv also to a bridging mode. It is worth noting that the materials which exchange with nitrates were the ones with the lowest Δv values while ZnNiHAc and ZnCoHAc which had the two largest Δv values did not react. Besides the Δv differences, the FTIR spectra of all the five acetate based compounds were relatively similar, although ZnNiHAc appeared to be having the most extensive hydrogen bonding network within the interlayer space, evidenced by the presence broad bands from 2900 to 3300 cm^{-1}, while the other materials had some sharp peaks within the same region. The sharp band observed at above 3550 cm^{-1} may be assigned to stretching vibrations of OH groups not involved in hydrogen bonding, whereas the broad bands at *ca*. 3450 cm^{-1} may be assigned to vibrations of OH groups involved in significant hydrogen bonding.[180]CH symmetric and asymmetric stretching vibration bands of the interlayer acetate anion are observed at 2950 and 3020 cm^{-1}. The bands at 1340 and 850 cm^{-1} can be assigned to CH_3 asymmetric deformation and H_2O rocking vibrations, respectively.[75,180] The water bending vibration mode, expected to appear at *ca.* 1600 cm^{-1}, is probably obscured by the strong and broad band due to carboxylate asymmetric stretch.

Table 4.3. FTIR peak frequencies and assignments.

ZnNiHAc	ZnCoHAc	ZnHAc	ZnCuHAc	CuHAc	Assignments
3020, 2950	3020, 2950	3020, 2950	3020, 2950	3020, 2950	$v(C\text{-}H)$
1015	1018	1019	1022	1023	CH_3 rocking
1336	1336	1336	1345	1345	$\delta s\ (CH_3)$
1403	1392	1390	1409	1408	$v_s(COO^-)$
1563	1549	1543	1554	1548	$v_a(COO^-)$
160	**157**	**153**	**145**	**140**	$\Delta = v_a\text{-}\ v_s$

4.3.3 Effect of metal center on acetate release kinetics

Anion exchange reactions in hydroxyl double salts (HDS) are generally viewed as topotactic,[53] since the overall structural integrity of the HDS is maintained during the reaction although the nature of the lamellar structure and the anions involved can result in a dissolution-reprecipitation mechanism.[202] These exchange reactions may involve multiple steps which include: transport of the guest ions in the bulk solution and their subsequent diffusion across the liquid film surrounding the lamellar compound, diffusion of the guest within the interlayer space to completely fill the space, chemical reaction at exchange sites within the layers, and diffusion of the host anion (displaced from the layers) in the interlayer space and its subsequent diffusion in the bulk solution away from the lamellar compound. Analysis of the solid samples obtained during the exchange reaction provides an insight into the transformations of both the guest phase and the host phase as the reaction progresses. Figure 4.8-4.10 show ZnHAc, CuHAc and ZnCuHAc PXRD profiles collected at different at 30, 35, 40, 45 and 50 °C; the profiles are plotted as a function of time.
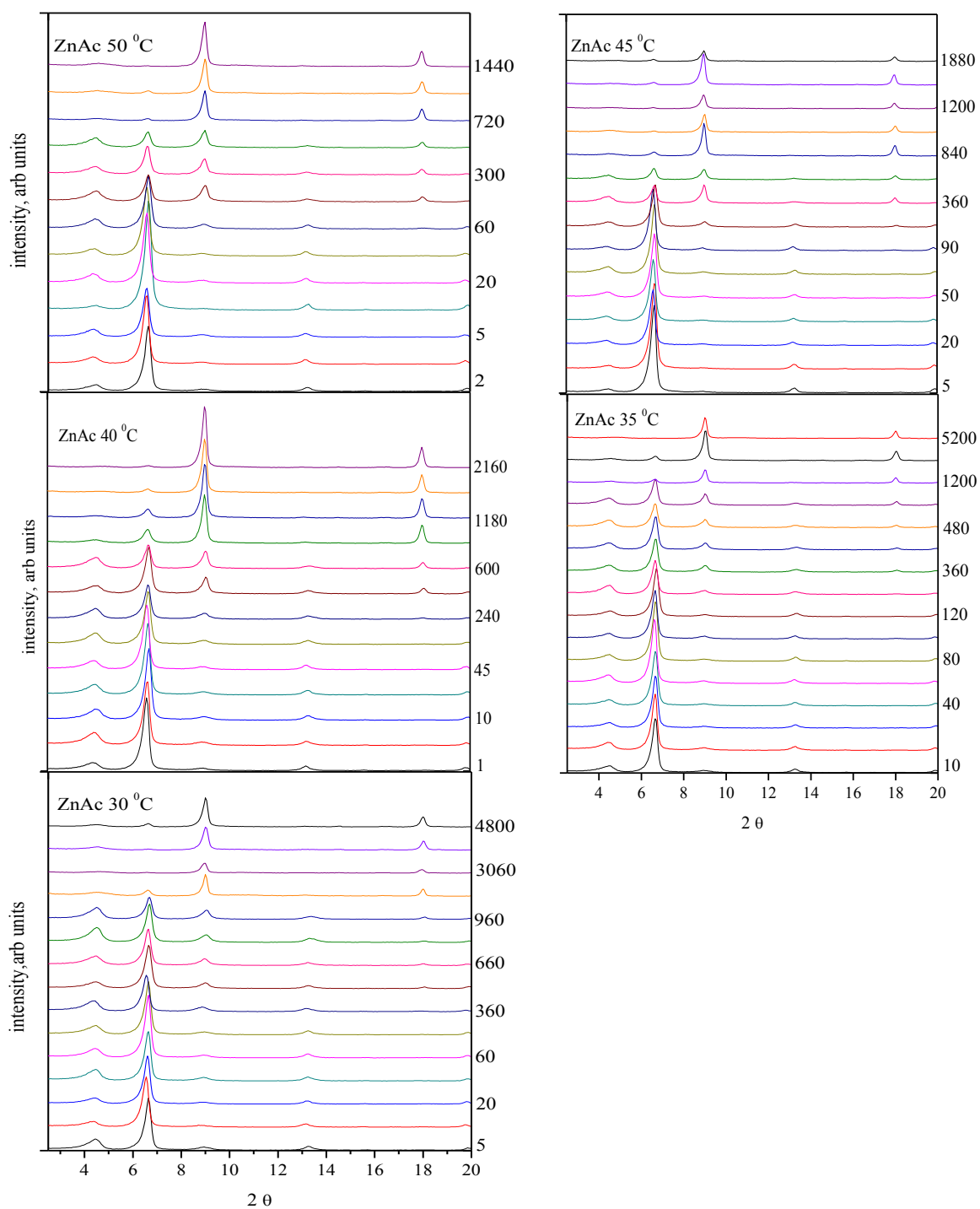
Figure 4.8. PXRD patterns for ZnHAc exchange with nitrate as a function of time (mins).Some of the time labels were omitted for clarity purposes.
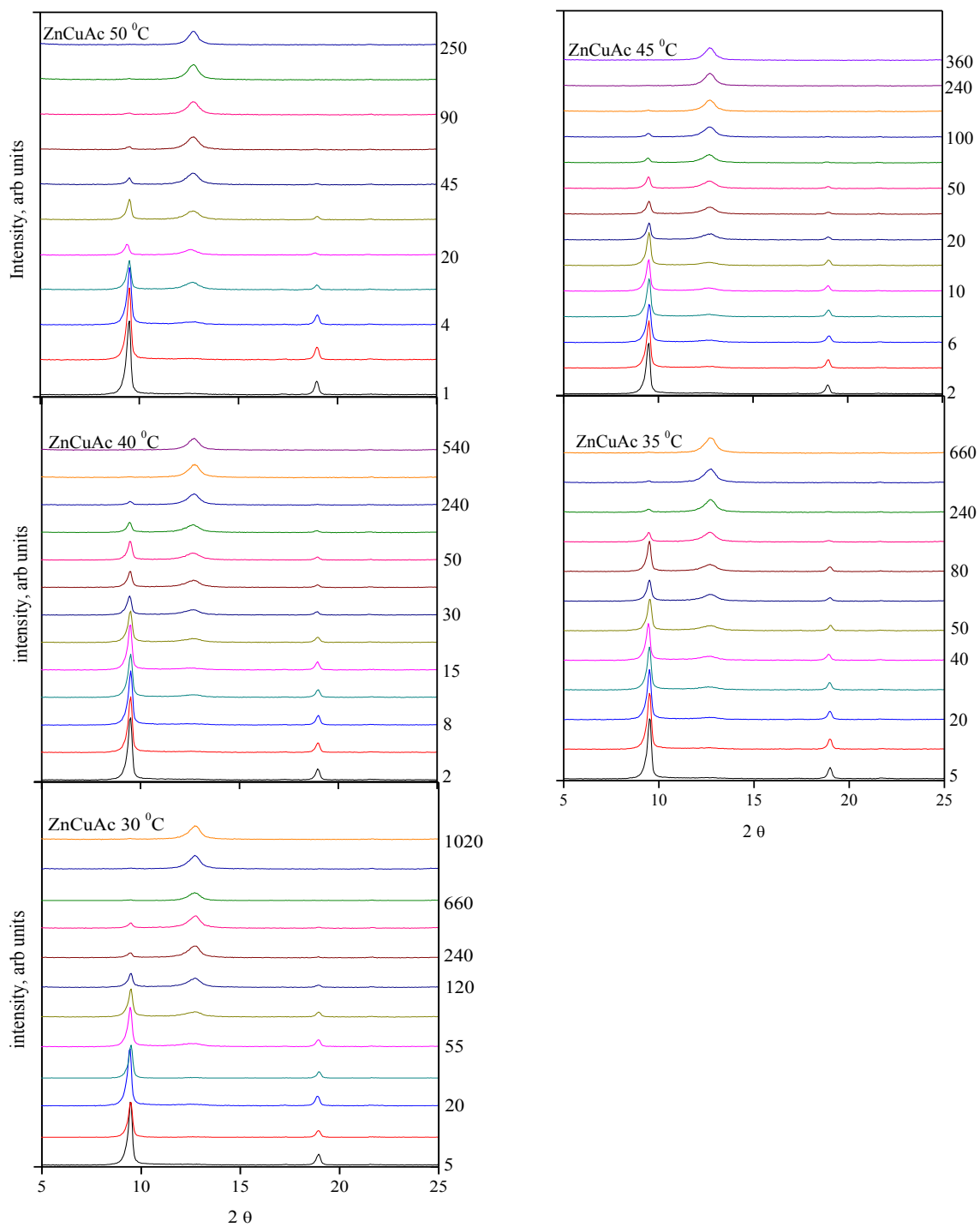
Figure 4.9. **PXRD patterns for ZnCuHAc exchange with nitrate as a function of time (mins).Some of the time labels were omitted for clarity purposes.**
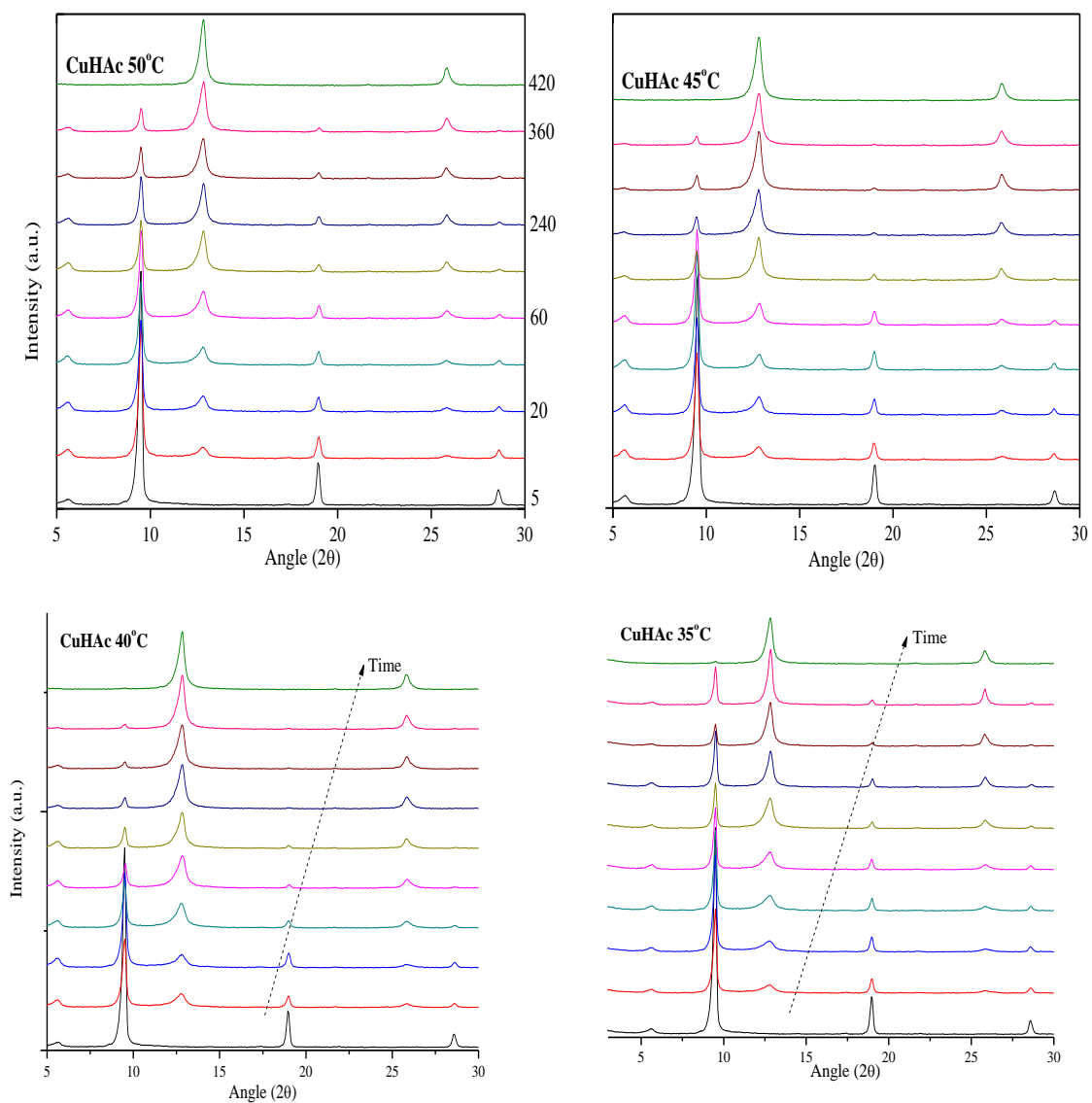
Figure 4.10. PXRD patterns for CuHAc exchange with nitrate as a function of time. Some of the time labels were omitted for clarity purposes.

In all the three HDSs, the exchange reactions went to completion as confirmed by the disappearance of the Bragg reflections from the acetates. The peak intensities of the Bragg reflections corresponding to both the acetate phase and the nitrate phase were used

for evaluation of the extent of reaction (α). The extent of reaction as a function of time plots obtained from solid state transformations at different temperatures are shown in Figure 4.11. The extents of reaction versus time data were fit to the Avrami –Erofe'ev nucleation-growth model[15,87,93]; the model provided reasonably good fits within the range of α of 0.1-0.95. The data was analyzed using the Sharp-Hancock approach[95] and the results are summarized in Table 4.4. The double logarithm plots used for the determination of the slopes (m) are shown in appendix B3 and B4.
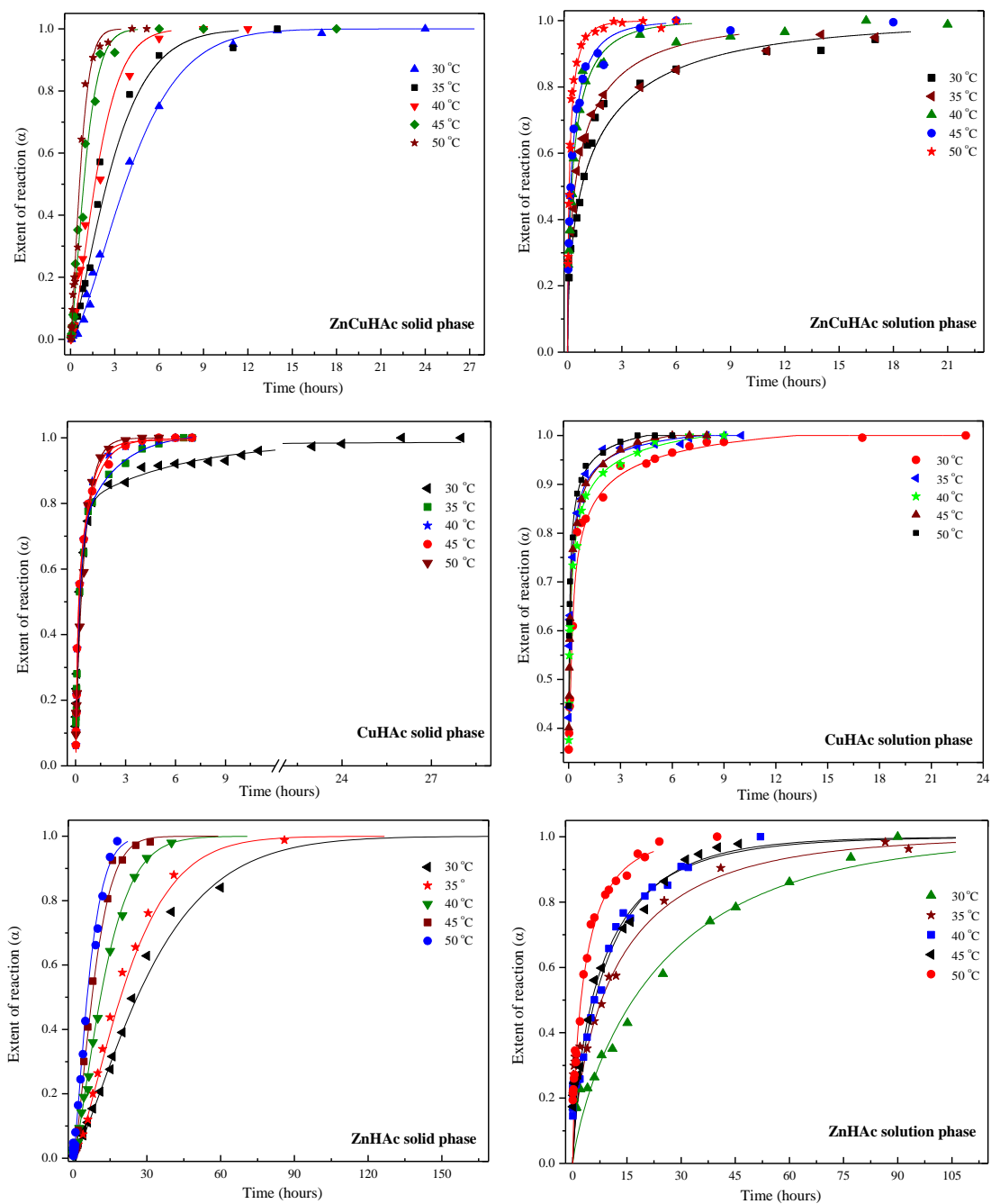
Figure 4.11. Extent of reaction as a function of time for the exchange reactions at various temperatures from solid and solution phase analysis.

Table 4.4. Kinetic parameters for solution and solid phase reactions in ZnCuHAc, CuHAc and ZnHAc.

Material	T (°C)	$k\ (s^{-1}) \times 10^{-4}$ solid	m	r^2	$k\ (s^{-1}) \times 10^{-4}$ solution	m	r^2
ZnCuHAc	30	0.6 ± 0.1	1.47 ± 0.08	0.980	1.7 ± 0.7	0.50 ± 0.02	0.988
	35	0.9 ± 0.3	1.31 ± 0.07	0.981	3.2 ± 1.2	0.48 ± 0.02	0.989
	40	1.3 ± 0.3	1.41 ± 0.10	0.991	6.5 ± 2.7	0.56 ± 0.02	0.987
A	45	2.4 ± 0.5	1.36 ± 0.06	0.987	8.7 ± 2.3	0.55 ± 0.01	0.992
	50	3.5 ± 0.5	1.36 ± 0.04	0.996	1.8 ± 0.5	0.57 ± 0.03	0.972
CuHAc	30	3.8 ± 0.2	0.73 ±0.06	0.979	13.0 ±7	0.38 ± 0.07	0.987
	35	5.0 ± 1.0	0.76 ±0.05	0.990	15.0 ± 5	0.33 ± 0.08	0.989
	40	6.1 ± 1.3	0.74 ±0.07	0.982	23.0 ± 6	0.35 ± 0.06	0.985
	45	6.3 ± 1.4	0.75±0.06	0.984	27.0 ± 5	0.39 ± 0.07	0.988
	50	6.5 ± 1.2	0.76±0.05	0.985	35.0 ±4	0.35 ± 0.06	0.992
ZnHAc	30	0.08 ± 0.01	1.00± 0.09	0.988	0.11 ± 0.02	0.81 ± 0.04	0.982
	35	0.11 ± 0.03	1.20 ± 0.10	0.991	0.20 ± 0.03	0.68 ± 0.04	0.973
	40	0.19 ± 0.03	1.00 ± 0.03	0.994	0.28± 0.04	0.76 ± 0.02	0.990
	45	0.28 ± 0.04	0.97 ± 0.03	0.981	0.31 ± 0.09	0.69 ± 0.03	0.983
	50	0.37 ± 0.06	1.30 ± 0.01	0.983	0.71 ± 0.12	0.65 ± 0.02	0.989

As can be seen in Tables 4.4, the rate constants obtained for anion release into solution are larger than the corresponding rate constants for the solid state transformation. This is to be expected since, for each given time period, the extent of reaction from solution phase is higher than that of the solid state transformation, up to the end of reaction. These differences may indicate that the loss of the host anions and subsequent loss of coherent diffraction from the host phase occurs faster than the gain in coherent diffraction from the product phase.[94,192] It can also be attributed to the presence of an intermediate with poor crystallinity[187] or a delayed appearance of the guest phase which may be because a significant number of layers have to be filled with the guest anions in

order to observe Bragg reflections corresponding to that guest phase. Because anion exchange reactions take place from layer to layer and due to the fact that a smaller anion (NO3-) is replacing a larger anion (CH_3COO^-) coupled with the rigidity of the HDS layers, the layers will collapse to the interlayer dimension of the guest phase when all the host anions in the layers have been replaced. Unless there is instantaneous complete exchange within the individual layers, the growth of the guest phase and the decay of the host phase lags behind acetate anions release into solution. As a result, some of the NO_3^- may be consumed and significant amount of CH_3COO^- released into solution without any noticeable changes in the guest diffraction peaks.

The extent of reaction (α) vs time (t) plots for the solid phase exchange profiles of ZnHAc and ZnCuHAc are sigmoidal in shape, which is typical of many solid-state transformations in bulk powder samples. Avrami exponents (m) observed for the solid phase transformation of ZnHAc and ZnCuHAc fell in the range 1.0 -1.5, suggesting a 2-D diffusion-controlled nucleation-growth model following instantaneous nucleation. CuHAc solid phase transformation had m values ranging from 0.7-0.8, which suggests that both nucleation and 2-D diffusion dependence contribute to the overall exchange reaction. From solution phase analysis, ZnCuHAc and CuHAc had m values ranging from 0.3-0.6, which is a clear indication of random nuclei formation and 2-D nuclei growth, while for ZnHAc both nucleation and 2-D diffusion are the rate determining steps. What can also be seen in the Tables 4.3 is that the rate constants in the three different HDSs follow the trend: CuHAc > ZnCuHAc > ZnHAc. Since ZnCuHAc represents an intermediate case between the above two, its kinetics is expected to be in between. Metal–oxygen bond strength can also help explain the observed kinetics trend. In study

conducted by Biswick *et al.*[56]whoanalyzedthe strengths of the metal-oxygen, bonds for

$Zn^{2+}$and Cu^{2+}compounds, a function of metal cation charge density; it was shown that the

zinc to acetate interaction was much stronger than the copper to acetate interaction.

Consequently, the weaker the metal-acetate bond the faster will be the exchange process.

Comparative studies conducted by Poul and coworkers[75] on hydroxyacetates of

Ni, Co and Zn revealed that despite similar XRD patterns and general chemical formula,

there exists a significant structural difference with respect to cation coordination. This

affects the thickness of the inorganic layers and organization of the water molecules and

acetate anions in the gallery which in turn will have an effect on anion exchange

reactions. These same qualitative arguments can be extended to explain the results

obtained in this study.

The temperature dependence of the reactions was evaluated using both a model-

based method and model-free method. Application of model-based methods yields a

single value of the activation energy representing the whole reaction progress. Model-free

methods, on the other hand, give activation energies corresponding to a particular extent

of reaction. Ion-exchange reactions of layered metal hydroxides are known to occur in

multiple steps which may give rise to significant dependencies of activation energy on

extent of reaction .[172]The use of model-free methods is advantageous in that it can reveal

this dependency of activation energy on the extent of reaction.[174] Such information is

crucial for systems that might change their reaction mechanism as the reaction

progresses. For the model-based analysis, the activation energy was calculated using the

Arrhenius equation, by plotting ln*k* against 1/T (see Appendix B5). Rate constants (*k*)

were obtained from the table 4.4. Activation energies were evaluated using the model-

free approach by applying the equation below;

$$\ln t_{\alpha} = \ln \frac{g(\alpha)}{A} + \frac{E_{iso}}{RT} \qquad \textbf{Equation 4.3}$$

where E_{iso}, $g(\alpha)$, A, t_{α}, R and T are the activation energy, integral reaction model, pre-exponential factor, time to get to a specific conversion, gas constant and temperature, respectively. The gradient of the slope of plot of $\ln t_{\alpha}$ against 1/T gives the activation energy corresponding to a specific α. The values of the model-based effective activation energies and model-free analysis energies are shown in

Figure 4.12.
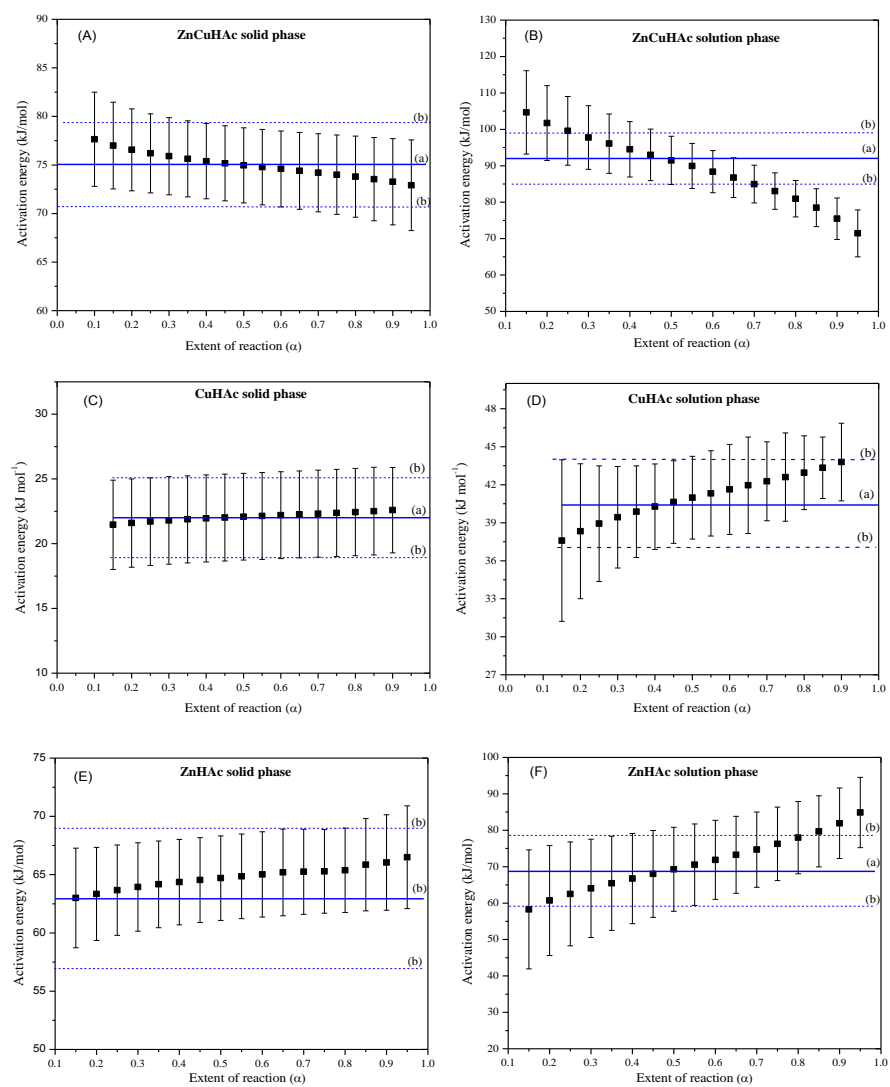
Figure 4.12. Variation of effective Ea with α for solid state and solution analysis. The solid line (a) represents the Arrhenius determined Ea together with the associated errors (broken lines, b).

There is a significant difference between the solution phase and the solid state obtained Arrhenius activation energies indicating different temperature dependences between the two different phases. It also indicates the complexity of these exchange processes. When the chemical reaction at the exchange sites is rapid, the transport

process (by diffusion) then determines the overall rate of reaction. The Avrami *m* coefficients obtained from analyzing both the solid materials and the solution phase released anion concentrations were, as noted previously, consistent with both nucleation and diffusion-controlled mechanisms.[91] If the exchange reactions involve several steps with different activation energies, the contributions of these steps to the overall exchange rates measured will vary with both temperature and extent of reaction[39,40]. The Arrhenius model fitting approach is aimed at a single activation energy value for the entire process.[83] The derivation of activation energies from the Arrhenius model, based on an exponential dependence of some rate parameter on temperature, is most of the time invalidated by the fact that the equilibrium between the activated and non-activated species in the rate determining step according to a Boltzmann distribution is not attained. Consequently, it can never be over-emphasized that kinetic expressions derived from overall reaction rates are not adequate to sufficiently characterize the reaction mechanism. Because of the complexity of some exchange processes, the value obtained by such an approach is an average that does not reflect changes in the reaction mechanisms and kinetics with temperature and extent of reaction. These drawbacks associated with model fitting can be eliminated by using the isoconversional methods, which allow activation energy to be determined as a function of temperature and/or extent of reaction. The dependence of activation energy to temperature and extent of reaction is determined without making any assumptions about the reaction model. As such, isoconversional methods are likely to provide consistent kinetics results. Table 4.5 provides a summary of the energies obtained from Arrhenius based modeling and the model free approach.

The E_a values obtained for ZnCuHAc solid state data range from 73−78 kJ mol^{-1} and those for solution analysis range from 71−102 kJ mol^{-1}. The data shown in

Figure 4.12 for solid state analysis reveal that, within experimental error, the E_a does not significantly change as a function of extent of reaction. This is an indication that the reaction can be described as proceeding via a single mechanism, consistent with fact that the Avrami m values (see table 4.4) did not vary significantly as a function of temperature. The E_a values obtained from the Arrhenius method lies within the range of values obtained using isoconversional method, indicating that in this case the model fitting approach provides reliable averaged effective activation energy for the entire reaction.[87] The activation energy obtained is consistent with a diffusion mechanism.

Solution phase E_a varies with extent of reaction (see Figure 4.12B) for ZnCuHAc. The E_a start at a value of 102 kJ mol^{-1} at an extent of reaction of 0.1 and drops to 90 kJ mol^{-1} at an extent of reaction of 0.5 and then decreases linearly to 71 kJ mol^{-1} at $\alpha = 0.95$. Complete replacement of host anions with guest anion within the layers increases the rate of anion-exchange in the neighboring layers by weakening the neighboring layer thus reducing the E_a for intercalation. If anion exchange within the layers controls the reaction rate, then the effective E_a of exchange in the neighboring layers is expected to decrease and this result in the gradual lowering of E_a values for the reaction as the exchange proceeds. This explains the observed decrease in activation energy from solid and solution phase analysis.

The Arrhenius E_a for CuHAc was 22 and 40 kJ mol^{-1} for solid and solution phase, respectively. There is a slight difference between the solid and solution phase isoconversional analysis, for the solid phase the E_a does not change with extent of

reaction whilst that of the solution phase increases linearly with extent of reaction as seen in Figure 4.10. The solid phase activation energies from both the Arrhenius and isoconversional analysis agree very well indicating that the exchange reaction in solid state takes place via a single mechanism and can be interpreted using the transition state theory. For the solution phase there is an increase in E_a with extent of reaction, it starts out about 36 kJ mol^{-1} at $\alpha = 0.15$ and then ends up as 43.5 kJ mol^{-1} at $\alpha = 0.95$. The Arrhenius determined E_a differs with that from isoconversional analysis except between $\alpha = 0.35$ and $\alpha = 0.5$.

In the case of ZnHAc, solid and solution phase isoconversional analysis show an increase of activation energy with extent of reaction. However the increases in the solid phase is small and when this is compared to the Arrhenius energy, it compares well within the error margins and it can be concluded that there is no significant difference between the two approaches hence the exchange reaction possibly takes place via a single mechanism. For ZnHAc solution phase, the isoconversional analysis determined E_a is 58 $\pm$ 9 kJ mol^{-1} at $\alpha = 0.15$ and increases linearly to 85 $\pm$ 6 kJ mol^{-1} at $\alpha = 0.95$. The activation energies obtained using model-based and model-free approaches are summarized in table 4.5.

Table 4.5.   Summary of activation energies (kJmol^{-1}) obtained from Arrhenius modeling and isoconversional analysis.

	E_a Solid phase (isoconversional)	E_a Solution phase (isoconversional)	E_a Solid phase (Arrhenius)	E_a Solution phase (Arrhenius)
ZnCuHAc	73-78	71-102	75 $\pm$ 4	92 $\pm$ 7
ZnHAc	63-66	58-85	63 $\pm$ 6	68 $\pm$ 10
CuHAc	22-23	37-43	22 $\pm$ 7	40 $\pm$ 3

The variation of E_a with extent of reaction indicates that the reaction does not take place via a single mechanism and the decrease in effective E_a might be due to decreasing contribution(s) from an initial mechanistic step(s) with higher E_a. The increase in activation energy with extent of reaction is possibly due to the formation of a boundary set up by the exchanged acetate anions and this in turn hinders the diffusion of the smaller nitrate anion into the layers. Activation energy values for 2-dimensional diffusion processes which occur in layered metal hydroxides are known to depend on the identity of the interlayer species and also on how densely packed the interlayer space is. According to Hulscher and Cornelissen[184] diffusion through organic matter matrix may resemble diffusion through polymer materials in which high Ea values (> 100 kJ/mol) can be obtained. Comparing the molecular formulae of the three compounds, (i) $ZnCu_{2.8}(OH)_{5.4}(CH_3COO)_{2.2}.H_2O$, (ii) $Cu_{2.1}(OH)_{3.3}(CH_3COO). H_2O$ and (iii) $Zn_{5.1}(OH)_8(CH_3COO)_2.4H_2O$, it can be observed that each mole of ZnCuHAc or ZnHAc has 2 moles of Ac, while 1 mole of CuHAc had 1 mole of Ac. These ratios imply that the gallery space of ZnCuHAc and ZnHAc is more organic than that of CuHAc, thus resulting in higher activation energies than the latter. CuHAc has lower activation energy when compared to ZnHAc and this supports the observed kinetics trend. Based on the observed kinetics trend, one would expect ZnCuHAc to have intermediate activation energy but this turned out not to be the case both from an Arrhenius and isoconversional analysis standpoints. The reason might lie in the fact that without a crystal structure it is difficult to know how the acetates and nitrate anions interact with the metal coordination centers. A knowledge of the crystal morphology is essential in understanding the main factors contributing to the either the nucleation or diffusion process. And also introducing

a second metal center adds more complexity to a system that is already not well understood in terms of how the exchange reactions proceed. Introduction of a second phase with different spatial coordinates increases the interfacial free energy and strain energy. This in turn might make it more difficult for either or both the guest and host anion to leave or get into the interlayer space consequently increasing the activation energy. Solid state reactions demonstrate a tangled interplay of various chemical and physical processes. Additionally, the kinetics of solid state reactions are known to be very sensitive to crystal structure, crystal size and other factors which are likely to change during the course of the reaction.

4.4   Conclusion

Reactivity in layered metal hydroxides is dependent on the identity of the hydroxide-layer metal cations. Varying the identity of the metal ions affects the interaction of the counter anions with the hydroxide layers. Nitrates in ZnCuHN and CuHN are grafted into the brucitic layers and are thus un-exchangeable. The compounds with unbound nitrates (ZnHN, ZnNiHN and ZnCoHN) were reactive. The coordination of the carboxylate group to the brucitic layers also played a part towards the reactivity of the acetate-based compounds; reactivity was favorable for acetates in bridging mode than in unidentate mode. By changing the nature of the layers in hydroxyl double salts, it is possible to control the rate of release of anions from layered metal salts. There was no significant change in the reaction mechanism; hence a model-based approach can be used to describe the rate of acetate release from ZnCuHAc, CuHAc and ZnHAc compounds.

The rate constants calculated using the Avrami-Eroféev model followed the trend:

CuHAc > ZnCuHAc> ZnHAc.

5.   Uptake of tri Chloroacetic acid using layered metal hydroxides: Relationship between thermal decomposition properties and kinetic parameters.

5.1   Introduction

Layered 2-dimensional metal hydroxides have attracted so much attention in the scientific community due to their potential industrial applications. Their importance lies on the possibility of modifying the interlayer space providing different chemical properties to the 2D structures[203]. The modification can be brought about by a number of techniques, which include; varying metal composition, intercalation[77], anion exchange[162], exfoliation[194] and or layer surface grafting reactions[6]. It has been observed through solid-state multi-nuclear NMR study of MgAl-LDHs that the metal cations within the layers adopt an ordered arrangement when the M^{II}/M^{III} ratio is 2:1.[204,205]The importance of these layered compounds is based on their ability to retain chemical species with electrical charges compatible to those layers.

There has been extensive efforts to understand the thermal degradation kinetics of solid state materials.[78]Studies have been conducted on non-isothermal decomposition kinetics of solid systems, utilizing a number of techniques that determine reaction mechanisms and kinetic parameters. Solid state reactions follow complex diffusion or interface controlled mechanisms. There are several thermoanalytical techniques often used to follow the course of solid state reactions but thermo-gravimetry (TG) is the commonest technique used.[90]Other complimentary techniques such as differential scanning calorimetry (DSC),[206]Fourier transform infrared spectroscopy (FTIR),[136] mass spectroscopy (MS)[17] and differential thermal analysis (DTA)[207] have also been coupled to

TG. In other thermoanalytical techniques, properties such as absorption, changes in mass or temperature are monitored as a function of time or temperature.[82,90] In isothermal thermo-gravimetry, change in weight is recorded as a function of time while non-isothermal thermo-gravimetry records change in weight as a function of temperature.[208,209]

Kinetic equations for rate law and kinetic parameters developed by Friedman[210] have been used to describe the thermal degradation of plastic using TGA. Nam and Seferis[211] used this equation to develop a composite methodology for multistage decomposition of polymers. From this extended methodology, analytical schemes for describing complex degradation of polymers by incorporating both experimental and theoretical considerations were established.

The aim of this work was to compare uptake efficiency of tri-chloroacetate (tClAc) using zinc aluminum hydroxy nitrate (ZAN) and zinc gallium hydroxy nitrate (ZGN) and zinc nickel hydroxy nitrate (ZNN).We also explored the relationship between ion-exchange and thermal degradation behavior of these layered materials.

5.2   Experimental

Aluminum nitrate nonahydrate, (+98 %) [(Al(NO$_3$)$_3$.9H$_2$O)], zinc nitrate hexa-hydrate, (99%) [(Zn(NO$_3$)$_2$.6H$_2$O)], gallium nitrate, (98 %) [(Ga(NO$_3$)$_3$) 2.5H$_2$O], sodium nitrate, 98 % [NaNO$_3$] were obtained from Alfa Aesar Co. trichloro acetic acid (99.9%) was obtained from DBH. Sodium hydroxide pellets, (99 %) [NaOH] was obtained from J. T. Baker. Nickel (II) nitrate hexahydrate (98+ %), was obtained from Alfa Aesar Co.

5.3   Synthesis

ZGN and ZAN were synthesized using a salt-base method[6], by adding 23.8 g (0.08 moles) of Zinc nitrate and 10.2 g gallium nitrate (0.04 moles) into 100 ml decarbonated deionized water in a 1 L beaker (solution A). A mixture of 0.1 M NaOH and 0.01 M $NaNO_3$ was prepared in a 1 L volumetric flask, using decarbonated deionized water (solution B). Solution B was added dropwise into solution A until a pH of 7.3 was achieved. The white precipitate was aged at room temperature for 24 hrs. After aging the solution was decanted, and about 1000 ml of fresh decarbonated DI water was added. The mixture was stirred for about 10 mins and then filtered under vacuum. The residue was again washed using about 500 ml DDI water. The white solid was dried in an oven at 40 °C under vacuum for 24 hrs. Zinc aluminum hydroxy nitrate was synthesized using the same approach except that solution B was added until a pH 6.5 was reached and the material was aged at 70 °C for 24 hrs[212]. For both materials, nitrogen gas was purged during the addition of solution B and also during the filtration stage. The dried materials were crushed using a motor and pestle, and then passed through a 125 micro meter sieve. Zinc nickel nitrate (ZNN) was synthesized using the method already outlined in chapter 3.2.2.

5.4   Characterization

Anion exchange was performed using 50 mM trichloro acetic acid, at pH = 7.0. 0.10 g of the layered materials was added to 10 ml of the anion solution in glass vials and stirred in a shaking water bath, at constant temperature, for a specified time period. After

reaction the solutions were filtered and dried at room temperature. The solids were analyzed using PXRD while the HPLC was used for the solutions. After reaction the concentration of the solutions were extrapolated from the calibration curves plotted using tClAc standards having concentrations ranging from 2.5-50 mM. Thermogravimetric analysis was performed on a Netzsch TG 209 F1, TGA-DSC instrument. Aluminum oxide crucibles were used for containing between 9-14 mg of the samples, and heating was done under a constant flow of nitrogen at heating rates ranging from 5-25 °C/min, from 30 °C to 800 °C.

Reitveld refinements were carried out using the Material Analysis Using Diffraction (MAUD) program.[144,213,214] Input data files used for refinements were taken from the Crystallographic Open Database (COD) of related model compounds.[142,143,145,215]

5.5   Results and Discussion

5.5.1   FTIR and PXRD
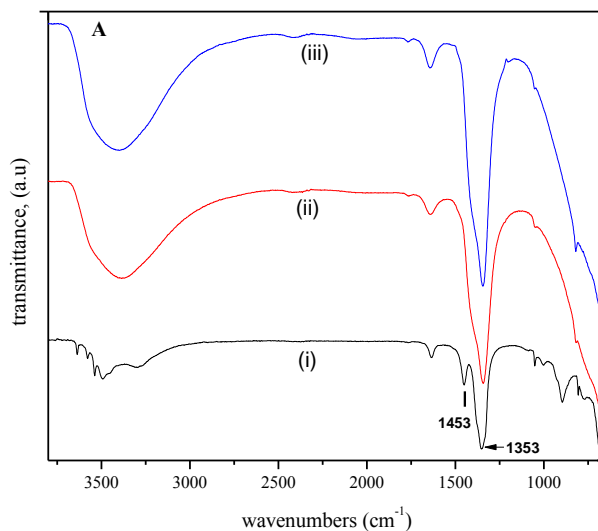
Figure 5.1.FTIR spectra for (i) ZNN, (ii) ZAN and (iii) ZGN precursor layered materials.

Interesting features in the FTIR spectra of these three compounds are observed within the frequency range 1300-1500 and also 2900-3600 cm^{-1}. ZGN appears to be having an almost identical FTIR spectrum with ZAN, but quite different from ZNN. The region 2900-3600 cm^{-1} reveals information about water molecules and hydroxyl groups; it also contains information about the extent of hydrogen bonding within the layers. The range 1300-1500 cm^{-1} reveals information about the nitrate anions. For ZNN, several sharp peaks are observed in the range 3500-3600 cm^{-1}, while broad bands are also

observed from 2900-3500 cm^{-1}. These sharp peaks imply the presence of free hydroxyl groups, not involved in hydrogen bonding. ZGN and ZAN on the other hand only show broad bands from 2900-3700 cm^{-1}; all these can be attributed to intense hydrogen bonding network present within the LDH gallery spaces. Looking at the deconvoluted ZNN spectrum it can be observed that there are more than two nitrate peaks, while the LDH spectra reveal that the observed nitrate bands are a sum of at least two nitrate bands. These observations are confirmed by the deconvoluted spectra shown below, from figure 5.2-5.3. The spectra below are the same as those shown in figure 5.1, but shown as inverted, with baseline correction for deconvolution purposes. The spectra were fit to a Lorentzian function using Origin.[216]
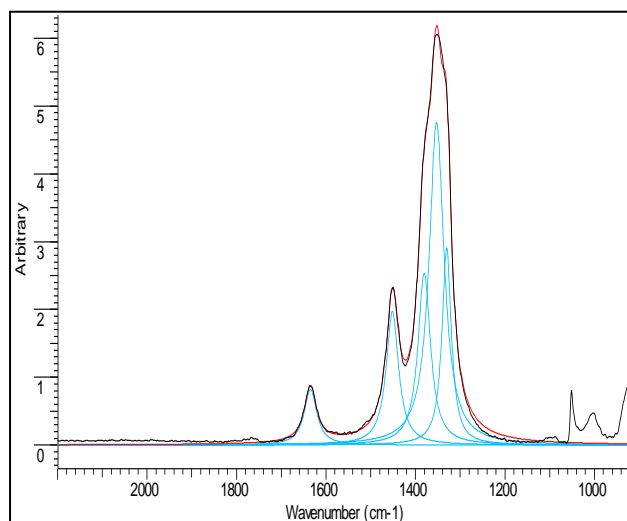
Figure 5.2.FTIR spectra revealing deconvoluted nitrate bands within the range 1250-1550 cm^{-1},in ZNN.
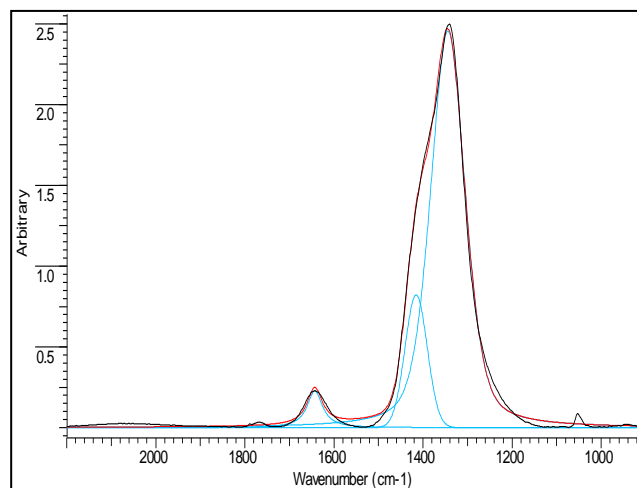
Figure 5.3.FTIR spectra revealing deconvoluted nitrate peaks within the range 1250-1550 cm^{-1}, in ZGN.
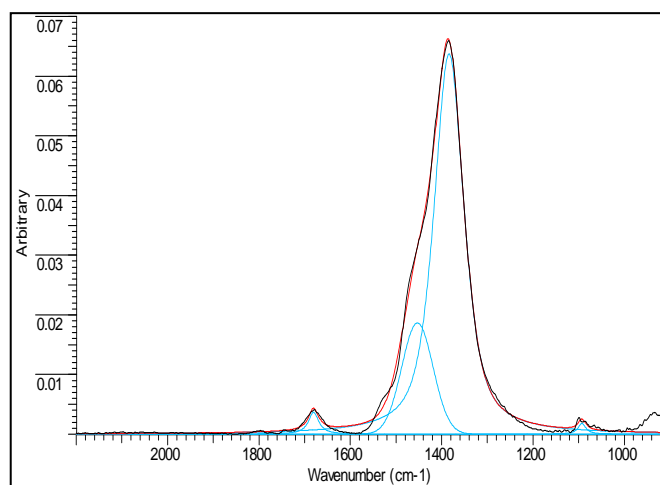
Figure 5.4. FTIR spectra revealing deconvoluted nitrate peaks within the range 1250-1550 cm^{-1}, in ZAN.

Rosenthal[217] and Addison[218] reviewed the structures and vibrational spectra of a large number of nitrate complexes; they showed that NO_3^- anions can coordinate to metal centers as a unidentate, symmetric, and asymmetric chelating bidentate, and bridging bidentate ligand. Gatehouse et al.[196] reported that the unidentate nitrate group exhibits three NO stretching bands, as expected for C_2v symmetry. The compound $Ni(en)_2(NO_3)_2$ (unidentate) exhibits three bands at 1420, 1305 and 1008 cm^{-1} corresponding to $v_a(NO_2)$, $v_s(NO_2)$ and $v(NO)$, whereas $Ni(en)_2NO_3ClO_4$ (chelating) exhibits three bands at 1476, 1290 and 1025 cm^{-1}. The difference between the two highest frequency bands is 115 and 186 cm^{-1} for unidentate and bidentate complexes. Generally, the band separation of the two highest-frequency bands is expected to be larger for bidentate than for unidentate coordination. The bands in ZNN and ZGN are too many for the symmetry to be attributed to just one binding mode or one nitrate conformation. This ability to have more than one conformation has also been observed in hydroxy double salts[165].

Table 5.1. FTIR frequencies (cm^{-1}) corresponding to the nitrate bands observed for the three compounds.

	ZNN	ZGN	ZAN
1	1480	1525	1405
2	1380	1460	1335
3	1350	1400	------
4	1330	1375	------

According to Rajamathi et al.[165], who prepared nickel hydroxy nitrate, the conformation of the nitrate anion is related to the strength of interactions between the anion and the nickel centers. The conformations reported by Rajamathi and co-workers were, however, for separate materials, not the same material having a mixture of conformations. Curtis and Curtis[219], reported a mixture of two conformations for the complex, $Ni(dien)(NO_3)_2$. The nitrate binding modes in $Ni(dien)(NO_3)_2$ have been reported to be unidentate and also bidentate with v_a and v_s equal to (1440 and 1315) and (1480 and 1300) respectively. this behavior has also been reported for carbonate anions in cobalt nickel hydroxides[220]. From this we can surmise that ZNN is found with a mixture of two nitrate phases; the unidentate and also the bidentate. As shown in figure 5.3, the deconvoluted FTIR spectra of ZAN, only two nitrate bands at 1413 and 1343 cm^{-1} are observed. The FTIR spectrum of ZAN is simpler, it has fewer peaks, and this suggests a nitrate ion with higher symmetry than the ions in ZNN and ZGN. The nitrate in ZAN can thus be assigned to a D_3h point group. LDHs (ZGN and ZAN) have been reported to be prone to carbon dioxide contamination,[221] the other peaks observed in these systems might be due to CO_2. Biswick et al. studied the thermal decomposition behavior of group of metal hydroxy nitrates, and they observed that NO stretch vary considerably from electrostatic to a covalent bound nitrate group. They calculated the difference between symmetric stretch (v_4) and asymmetric stretch (v_1) vibrational frequencies, and concluded that bigger the difference the more covalent the $M-ONO_2$ bond will be. For ZNN the difference was found to be 101 cm^{-1} (=1453- 1353cm^{-1}), while for ZGN and ZAN the difference is so small suggesting that the nitrates in ZNN are more ionic than the nitrates in the LDHs.
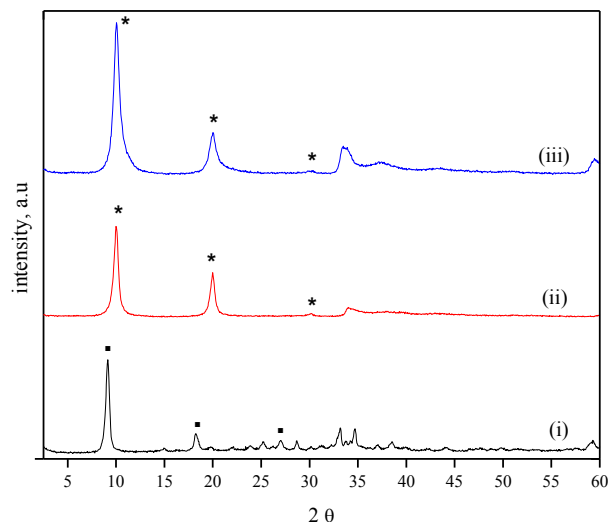
Figure 5.5.PXRD patterns for (i) ZNN, (ii) ZAN and (iii) ZGN.The asterisk (*)are showing the 003, 006 and 009 diffraction peaks for ZGN and ZAN, while the squares are showing the 001, 002 and 003 reflections for ZNN.

The PXRD patterns for the precursor materials are shown in Figure 5.5. All the

materials show at least three equally spaced Bragg reflections at low 2θ values. The

presence of these equally spaced peaks in XRD profiles is evidence that the materials are

layered. Interlayer spacing can be calculated from these Bragg reflections using the

Bragg equation.[6] Broad asymmetric peaks are also observed, at higher 2θ values, which

have been attributed to irregular stacking of sequential layers (i.e. turbostraticity).[10,222]

The PXRD results for ZAN are consistent with literature values and have been indexed as

rhombohedral $Zn_2Al(OH)_6NO_3.1.9H_2O$ with a space group $R\bar{3}m(166)$, (PDF# 055-

0193).[209]The lattice parameters for this crystal are: a= 3.0780 Å and c=26.7838 Å.

Synthesis of ZGN is not reported anywhere in literature, hence no PDF files can be used for referencing. ZGN and ZAN can be assumed to be having same crystal structure since they have a nearly identical PXRD pattern. The three 00l peaks for ZNN, shown by the asterisks (∗), are at 9, 18 and 27°. These 2 θ values translate to d-spacings equal to 9.7 and 8.8 Å for ZNN and the LDHs, respectively. Meyn et al.[178] synthesized ZNN using the same method and obtained a material with a d-spacing 9.68 Å. Since Ga and Al are in the same group, it would be expected that the space group symmetry of the crystallites making up the LDHs be of the identical. The PXRD profile of ZGN was fit using Rietveld method.
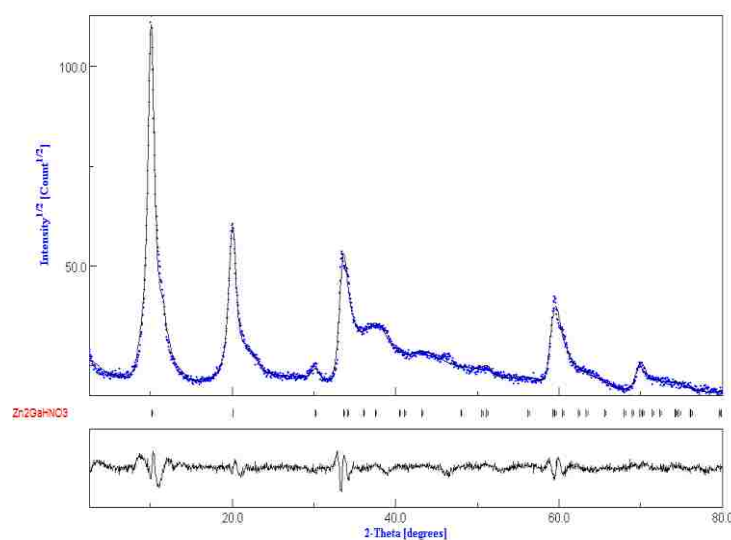
Figure 5.5. PXRD pattern of ZGN LDH. The vertical lines correspond to Bragg angles.

After analysis a space group R-3m, χ^2 =2.1% , R_w =7.1 %, R_{exp} = 3.4% R_b and 6.9 % were obtained. A total of 21 parameters were refined. The background was fitted to 6 coefficient polynomial. Lattice parameters were: a= 3.121 Å and c=26.908 Å. The refinement results are shown in table 5.2. Although the fit was good, the position and occupancy of N and O2 atoms are unrealistic. The N atoms are too close for the system to be stable, and also the amount of N and O2 observed are too low. This might be a result of the sample used. It can be observed from the PXRD profile used for this refinement that the sample was not 100 % pure; there is peak at *ca* 22 ° which is not part of the layered material. There is also a possibility of structural disorders which causes broadening of Bragg reflections.[134] This broadening can be mistakenly attributed to crystallite size effects, which is common in layered materials. Broadening of the higher-2-theta peaks is attributed to turbostraticity.[6] Turbostraticity, stacking faults and interstratification are some of the known disorders affecting crystallinity of layered metal hydroxides.[224] These disorders will complicate the accurate determination of the crystal structure of the material under investigation.

Table 5.2. Results of the Rietveld refinement of the structure of ZGN.

	x	y	z	Occupancy	Goodness of fit
Zn	0.000000	0.000000	0.000000	0.66667	R_w= 7.1189
Ga	0.000000	0.000000	0.000000	0.33333	R_{exp}= 3.4164
O1	0.000000	0.000000	0.381009	1.00000	R_b= 5.4601
H1	0.000000	0.000000	0.800170	1.00000	R_{wnb}=6.9249
N	0.000000	0.000000	0.029952	0.08333	Sig = 2.0837
O2	0.006048	0.006048	0.150923	0.08333	

5.5.2   Reaction Kinetics

Ion exchange of tClAc was conducted using the three layered materials, ZNN, ZGN and ZAN. The reactions were conducted at room temperature; changes in concentration were monitored using HPLC. After the reactions had equilibrated, the extent of reaction (α) which is equal to $[tClAc]_t/[tClAc]_{eqm}$ was plotted against time (mins). $[tClAc]_t$ is the concentration at time while $[tClAc]_{eqm}$ is the concentration at equilibrium.
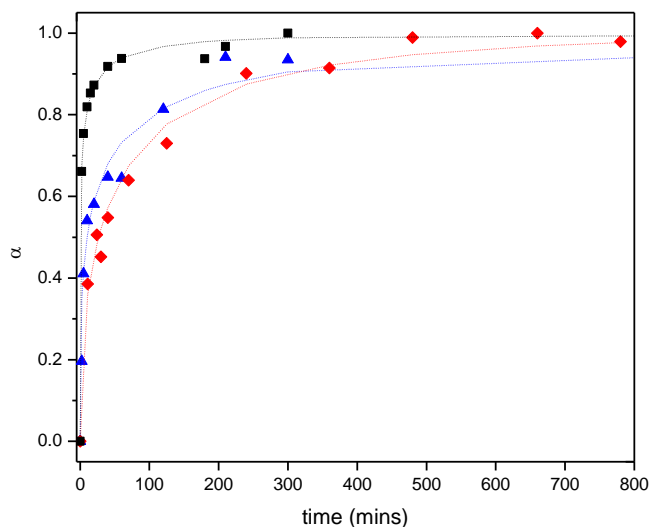
Figure 5.6. Extent of reaction against time for trichloro acetate uptake using ZGN (triangles), ZAN (squares) and ZNN (diamonds).The dotted lines are for the Avrami-Eroféev model fit.

From Figure 5.6, it can be observed that tClAc uptake reached equilibria faster for ZAN (100 mins), followed by ZGN (about 200 mins) and finally ZNN (about 700 mins). Use of PXRD (figure 5.7) helped reveal some trends which were hidden in the solution phase data. First, it can be seen that the host nitrate peak which was at 10.0 ° shifted by 11.3 ° for both ZGN and ZAN. The behavior occurred almost instantaneous especially for ZGN. For ZAN, the tClAc peak intensity continued to grow to the point where the host and guest peak were equal. It was also observed that the guest peaks slightly shifted to lower as the reaction time increased, such that the earliest tClAc corresponding to 5 mins is at 6.4 °, while the latest peak corresponding to 24 hrs is at 6.1 °.
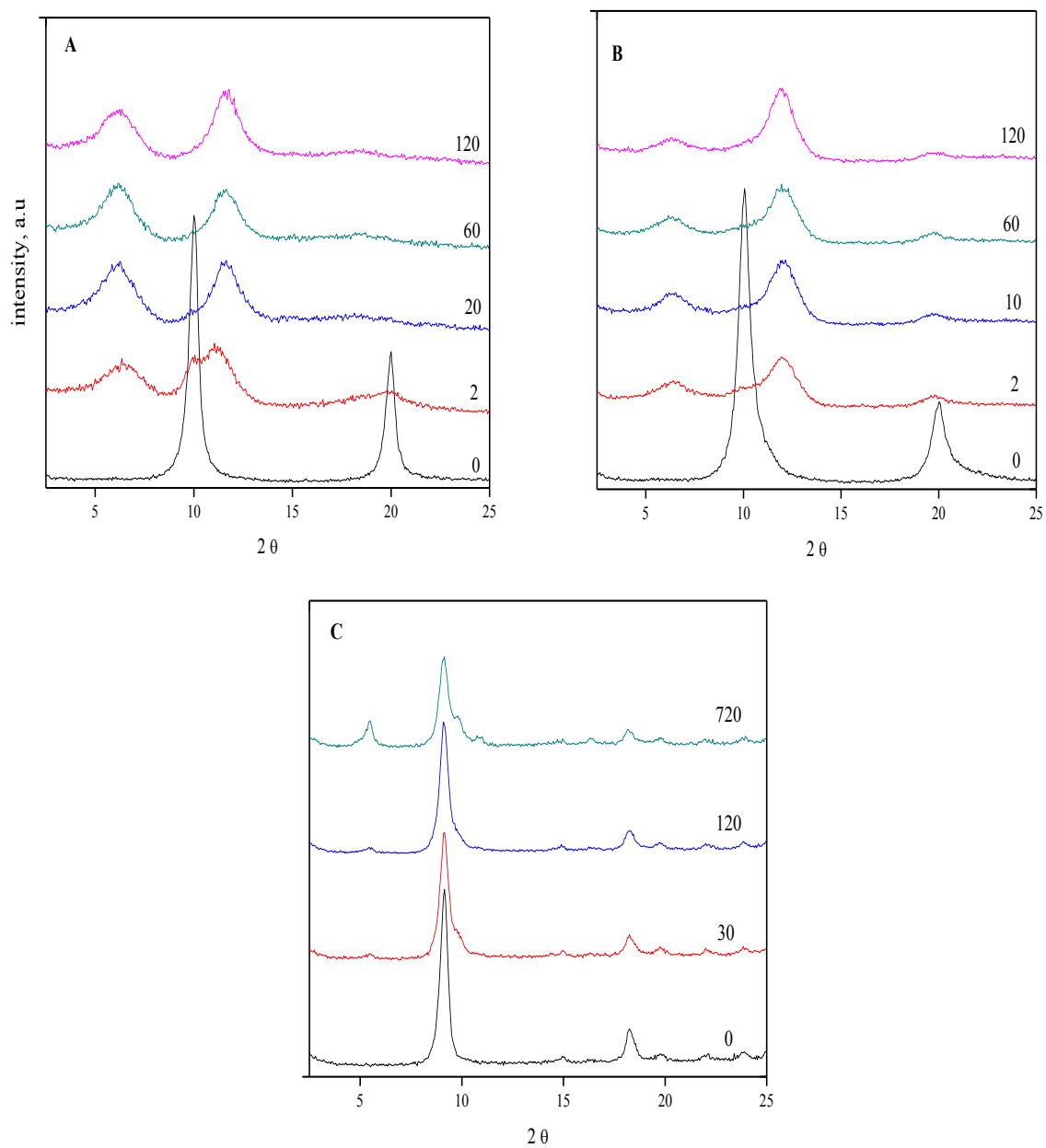
Figure 5.7.PXRD profiles for the pristine materials (A) ZAN, (B) ZGN and (C) ZNN and their exchange products arranged as a function of time (mins).

In order to understand the ion exchange kinetics occurring in these layered materials, solution phase data were fit to the following kinetic models[96,97,192,225].

i. **Avrami-Eroféev model**. The Avrami-Erofe'ev nucleation-growth model is one of the most widely utilized approach for evaluating intercalation or exchange kinetics within heterogeneous systems[15,87,94];

$$\alpha(t) = 1 - e^{(-(kt)^m)}$$

Equation 5.1

where α, t, m and k are the extent of reaction, time, the Avrami exponent and the rate constant respectively. The Avrami exponent is frequently used to provide insight into the reaction mechanism. This ability to describe the mechanism m is one of the reasons why this method is widely utilized. Mechanism m and rate constant (k) can be evaluated from the plot of $\ln(-\ln(1-\alpha))$ against $\ln(t)$. The extent of reaction is obtained using the expression $\alpha = C_t/C_{eqm}$, where C_t and C_{eqm} are the anion concentrations at time t and at equilibria, respectively.

ii. **First order rate model**. This model has been applied to ion exchange reactions and can be expressed as;

$$\ln(\frac{C_t}{C_0}) = -k_d t$$

Equation 5.2

which can be expressed as;

$$\ln(\alpha) = -k_d t \,,$$

Equation 5.3

where α is equal to C_t/C_o, k_d is the apparent rate constant, C_t is concentration at time t while C_o is the initial concentration[96].

iii.   **Parabolic diffusion**. The model is based on the assumption of a diffusion-controlled rate-limiting process in media with homogeneous particle sizes[97].

$$\left(1-\frac{c_t}{c_0}\right)\frac{1}{t} = k_d t^{-0.5} + a,$$ **Equation 5.4**

where k_d is the apparent uptake rate constant. The model plots $\left(1-\frac{c_t}{c_0}\right)\frac{1}{t}$ against $t^{-0.5}$. The ratio of $C_t : C_0$ can also be expressed as the extent of reaction (α).

iv.   **Modified-Freundlich**. The model is expressed as;

$$C_0 - C_t = k_d C_0 t^a,$$ **Equation 5.5**

where k_d is the uptake rate coefficient and a is a constant. This model has been widely applied in ion exchange and adsorption with clay materials. Rearrangement of the equation yields the form below[98];

$$\log(1-\frac{C_t}{C_0}) = a\log(t) + \log k_d$$ **Equation 5.6**

The plots of the four models mentioned above and their corresponding fits are shown in Figure 5.8 below.
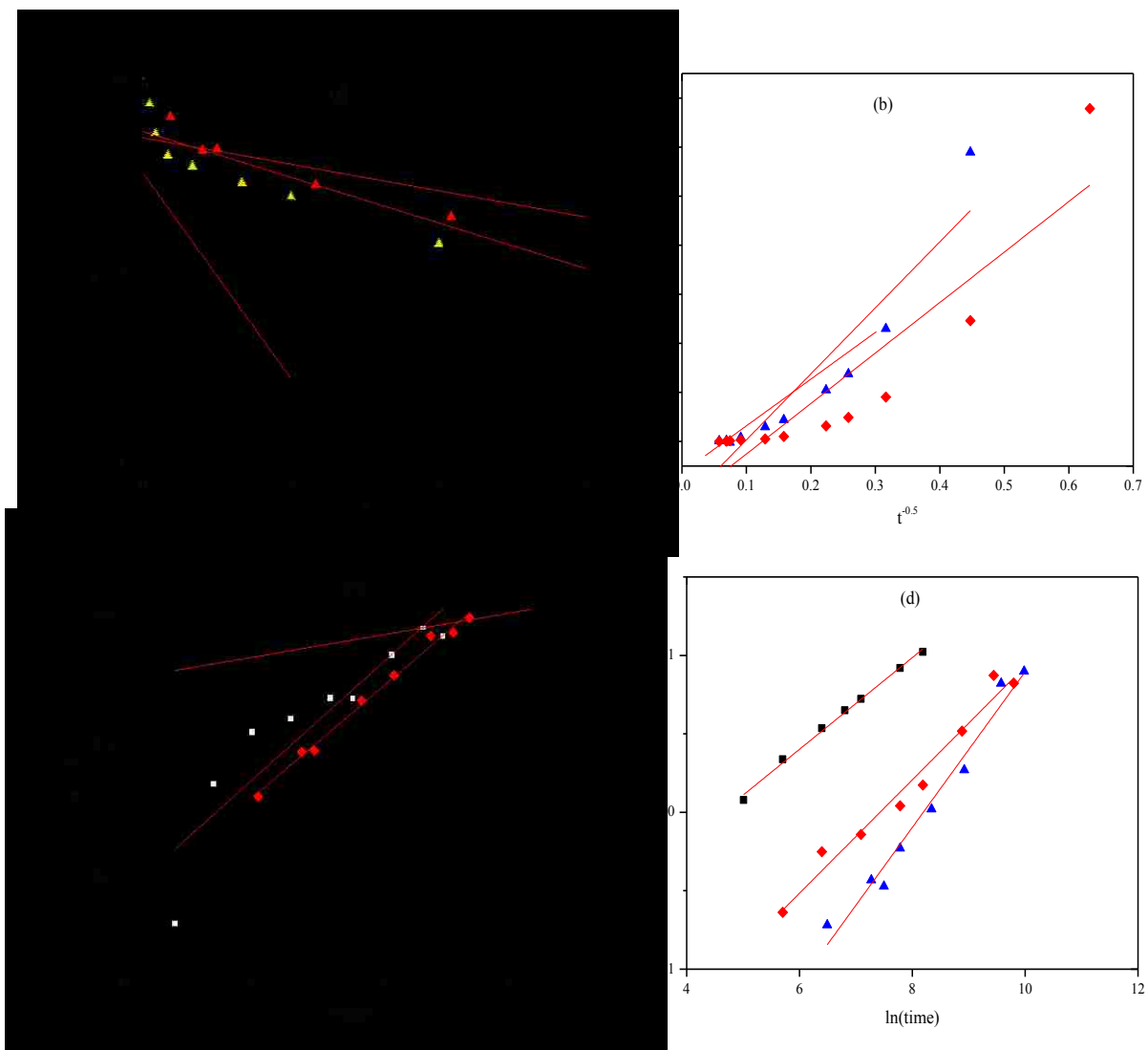
Figure 5.8. Plots of kinetic models (a) first-order (b) parabolic diffusion (c) modified Freundlich and (d) Avrami Erofev, for the uptake of triChloro acetate using ZNN (diamonds), ZGN (triangles) and ZAN (squares).

Table 5.3. Kinetic parameters for the trichloro acetate uptake.

Material	Kinetic models	R^2
ZNN		0.97
ZGN	Avrami-Eroféev	0.97
ZAN		0.99
ZNN		0.91
ZGN	First-order	0.87
ZAN		0.68
ZNN		0.90
ZGN	Parabolic diffusion	0.95
ZAN		0.89
ZNN	Modified Freundlich	0.99
ZGN		0.94
ZAN		0.94

From the calculated R^2 it can be concluded that ZAN system is best described using the *Avrami-Eroféev* model ($R^2 = 0.99$), while the *Modified-Freundlich* model was the most appropriate for ZNN system ($R^2 = 0.99$). The ZGN system on the other hand can also be described using the Avrami-Eroféev model, but the R^2 values are low, 0.97. The *parabolic diffusion* and *first-order* models cannot be used to describe the exchange reactions of all these materials since their R^2 values were poor, ranging from 0.68-0.91. R^2 values differed significantly, meaning that only the rate constants obtained using the Avrami-Eroféev model should be compared, since R^2 value for this model ranged from 0.97-0.99 for all the systems. The Avrami rate constants are summarized in table 5.4.

Table 5.4. Rate constants for the uptake of tClAc using ZNN, ZGN and ZAN.

Material	Rate constant ($\times 10^{-3}$)	R^2	m
ZNN	0.3 ± 0.2	0.97	0.50 ± 0.03
ZGN	0.6 ± 0.4	0.97	0.36 ± 0.03
ZAN	9.7 ± 0.2	0.99	0.29 ± 0.01

Rate constants were calculated only for the Avrami model, since it's the only one that produced relatively good fits compared to the other models. For the Avrami model, ate constants are obtained by using the expression $k = \exp(I/m)$, where k is the rate constant, I is the intercept obtained from the double logarithm plots and m is the slope of the same plots. The rate constants were in the order ZAN > ZGN > ZNN, for the Avrami model. The m value obtained from the double logarithm plot (Avrami) which ranged from 0.3-0.5, imply that tClAc uptake was diffusion controlled. Slope (m) values less than 0.5 have been reported to be diffusion controlled while those within the range 0.5-1.0 have been describe to be for systems that are both diffusion and nucleation dependent. PXRD data revealed that upon intercalation of tClAc a new nitrate phase, in addition to the original one, started to form. This phase transition was very slow that even after 720 mins (Figure 5.7 C) the two nitrate phases were still present. This slow transition is consistent with the observed m value and also on the overall exchange kinetics of this system.

5.5.3 Thermal analysis

Layered metal hydroxide structures are stabilized by electrostatic interactions between anions and the positively hydroxide layers.[226,227]The strength of these interactions determines the ease of ion exchange. According to Miyata et al. the ion exchange equilibrium constants for LDHS are in the order: $OH^->F^->Cl^->Br^->NO_3^->I^-$ and $CO_3^{2-}> C_{10}H_4N_2O_8S^{2-} > SO_4^{2-}$, for monovalent and divalent anions, respectively.[228]Using this series, nitrate or iodide-containing LDHs will be expected to be easily exchangeable, than those containing carbonate or fluoride anions. The relative strengths of these interactions will affect release or uptake rates. In addition to rate constants, activation energies (E_a) have also been calculated as a way of measuring the strengths of these interactions. The conventional way of determining ion-exchange E_a, for LDHs and related compounds, involves running a series of exchange reactions at a constant temperature (T_1),while extracting samples after a specified time period and then repeating the same procedure at temperature T_2, T_3…..T_n. The data collected after these time periods will be used for determining the rate constants which can be used for the evaluation ofE_a[229,230], using the Arrhenius equation.

In this study we seek to explore the relationship between the observed exchange rates and thermal degradation behavior of the three materials (ZNN, ZGN and ZAN) used for the uptake of tClAc. Thermal decomposition profiles of layered metal hydroxides are generally constituted into two isolated thermal events; the first stage being the loss of adsorbed water and water of hydration followed by the loss of water formed from dehydroxylation together with the release of gases formed from the counter-ions[75,231].

Depending on the counter-ion, gases such as NO_2[6], HNO_3, SO_3[232]or CO_2[233], can be released. The largest mass loss generally occurs in the second stage resulting in the formation of metal oxides or mixed metal oxides. For our purposes, the most interesting stage is the one where the observed mass loss will be for the decomposition or loss of the counter-anions.

It has been reported elsewhere that layered metal hydroxide thermal degradation properties are affected by the identity of the metal cations directly interacting with anions.[6,56]This thermal decomposition can be monitored using TG-DSC, while TG-FTIR can be used for identification of the released gases.TG-DSC results for the decomposition of ZNN, ZAN and ZGN are shown in figures5.8-5.10. the graphs on the left are DSC profiles showing the derivative (%/ °C) against temperature in °C, those on the right are TG profiles showing % weight remaining versus temperature (°C).
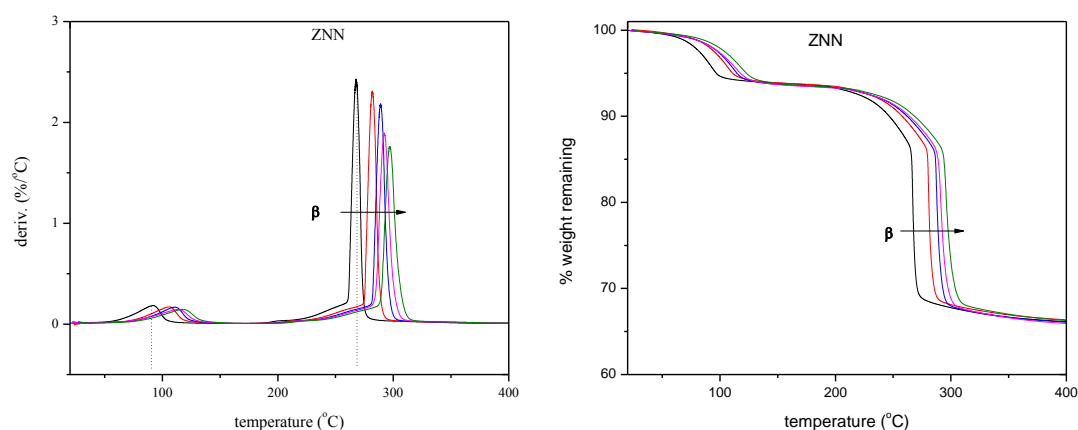
Figure 5.9.TG-DSC profiles for ZNN at β=5, 10, 15, 20 and 25.
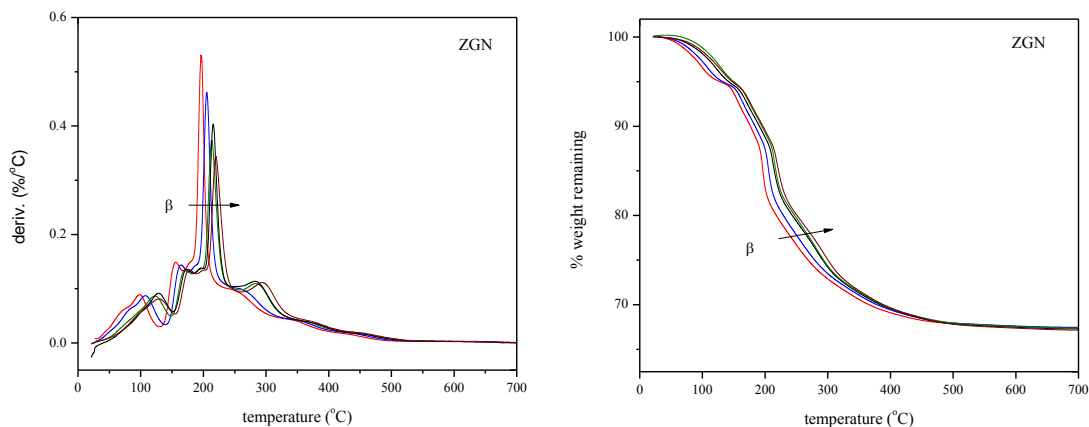
Figure 5.10.TG-DSC profiles for ZGN at β=5, 10, 15, 20 and 25.
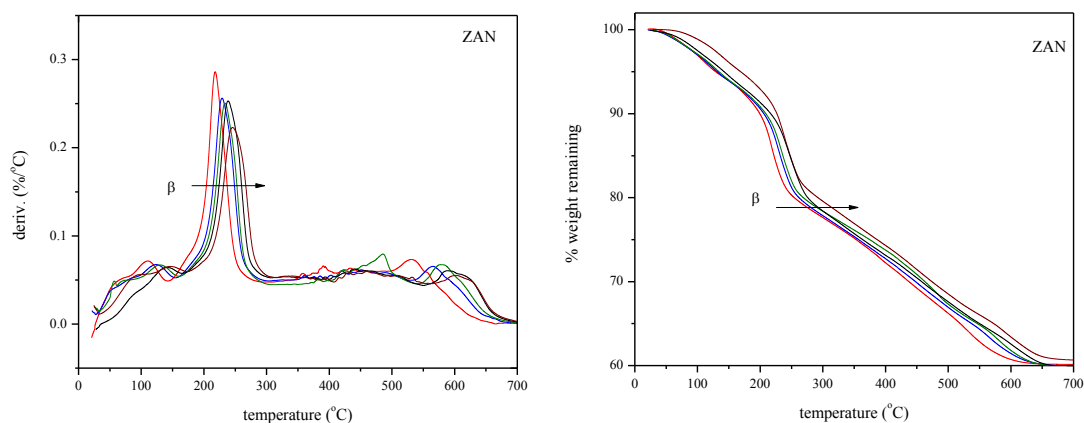
Figure 5.11.TG-DSC profiles for ZAN at β=5, 10, 15, 20 and 25.

The thermal decomposition profiles observed for ZNN decomposition (see Figure 5.9) exhibit two isolated thermal events, one at around 90 °C and the other at around 268 °C. these two events can be assigned to (i) loss of water adsorbed water and also water of hydration and (ii) release of water formed by dehydroxylation and release of gases

formed when nitrates decompose. The first decomposition stage resulted in a 3 % mass loss while for the second stage there was a 15 % mass loss. For ZGN and ZAN there about four stages of decomposition observed. For ZGN, the first mass loss (4 %) is observed at 132 °C, then (7 %) at 174 °C, (15 %) at 220 °C and (25 %) at 296 °C. ZAN mass losses of 5, 15 and 30 % are observed at 149, 245 and 440 °C. Identification of the gases being released as a function of temperature was done using TG-FTIR, and the results are shown below.
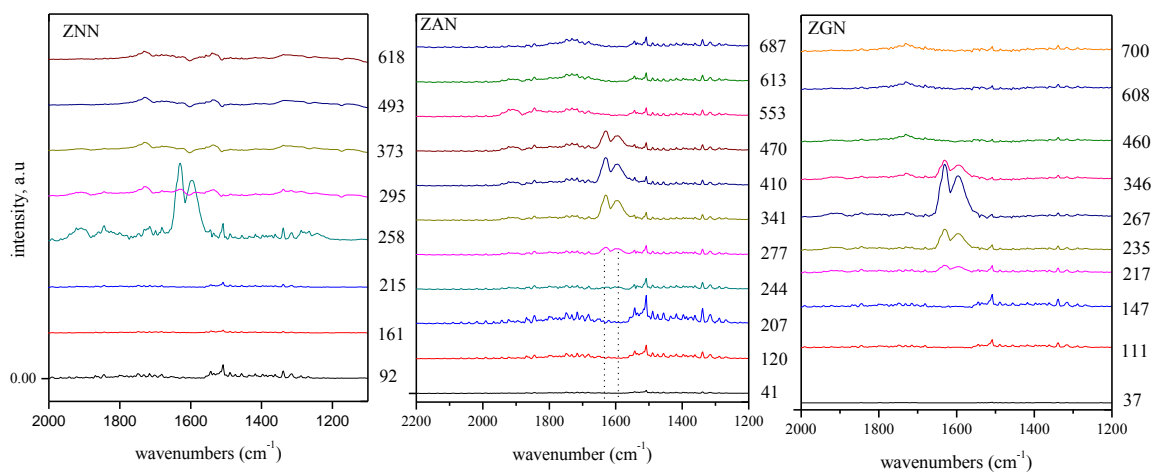
Figure 5.12. TG-FTIR profiles for ZNN, ZAN and ZGN. The spectra are plotted as a function of temperature, in degrees Celsius.

TG-FTIR data was obtained after from 30 °C to 800 °C at a heating rate of 20 °C/min and also under nitrogen atmosphere. Figure, for ZNN, show two FTIR peaks at 1691 cm^{-1} and 1659 cm^{-1} confirm that the gas released at temperature around 260 °C is

nitrogen dioxide (NO_2).[234] The identity of the gases can also be confirmed by using the library that comes with the instrument; a table as the one shown in the appendix D is produced, giving all possible matches found. The FTIR profiles ZGN and ZAN also reveal that NO_2 is the gas releases after decomposition of the nitrate. However, for the LDHs, NO_2 release was observed over a wide range of temperatures. The nitrate in the LDHs could be binding stronger to the layers as the temperature increases, thereby stabilizing the compounds. Since NO_2 is the gas produced after NO_3^- decomposition, this would imply that the formation of metal oxides may be initiated through the breaking of the N-O bond in M-O-NO_2, where M is the metal cation.

To evaluate the thermal stability of layered metal hydroxides, decomposition activation energies (E_a) were calculated. This activation energy was obtained by monitoring the peak corresponding to the largest mass loss (Tp), which is also the temperature at which NO_2 started to be release, plotted as a function of heating rate (β). The β values were then used to calculate the activation energies using a non-isothermal method, Kissinger's multi-curve method.[235,236] This method involves heating a material from T_1-T_2 at a constant heating rate (β); by having at least four different heating rates, activation energies will be evaluated. Only the first peak corresponding to the first stage decomposition of the nitrate from the layers from the layers was used. The Kissinger corrected kinetic equation is expresses below:

$$\ln(\frac{\beta}{T_p^2}) = \ln(\frac{AR}{E_a}) - \frac{E_a}{RT_p}$$

Equation 5.7

where T_p is the peak temperature, β is the heating rate (°C/min), A is the pre-exponential factor while R is the gas constant. A plot of $\ln(\beta/T_p^2)$ against $1/T_p$ will yield a straight line with a slope equal to $-E_a/R$. In this work we used five heating rates ($\beta = 5, 10, 15, 20$ and 25 °C/min), by ramping from 30- 800 °C under nitrogen atmosphere.

Table 5.5. Tp vs heating rate for the decomposition of the three materials.

β (°C/min)	ZGN	ZAN	ZNN
5	198	218	268
10	207	228	282
15	211	237	289
20	216	242	292
25	221	245	297

ZNN had the highest Tp values, followed by ZAN and lastly ZGN. The strength of the $MO-NO_2$ bond is related to Tp; since ZNN had the largest Tp temperature than would suggest that its $MO-NO_2$ bond was the strongest. This would also mean that the $MO-NO_2$ bond in ZAN will be lesser stronger than that in ZNN but stronger than the $MO-NO_2$ bond in ZGN. The observed trends are consistent with what has been reported elsewhere.[6] It has been reported that decomposition temperatures are higher when a compound is made up of cations with smaller charge densities. The charge densities of the three cations which interact with the nitrate are in the order: Ni < Ga < Al. The strength of the $MO-NO_2$ bond has been reported to be reduced through the polarization of the electron cloud of the nitrate anion by the charge density on the metal cation.[237] Tp values for ZGN are lower than expected; this could be a result of the electronegativity of

Ga^{3+} which is slightly higher than that of Al^{3+}. A higher electronegativity would imply

that the M-O bond will be slightly stronger than expected hence causing a slight

weakening of the $MO-NO_2$ bond and thus lowering of the Tp. The activation energies

were evaluated by plugging in Tp values shown in table 5.5, into equation 5.7.

Table 5.6. Ea values (in kJ/mol) corresponding to the decomposition of the nitrate for the three
systems.

Material	E_a	$\pm E_a$
ZAN	113	5
ZGN	128	7
ZNN	135	8

The linear plots of $\ln(\beta/Tp^2)$ versus $1/Tp$, used for determining E_a are shown in the

appendix D. E_a values derived from table 5.5 are shown in table 5.6 together with their

corresponding experimental errors. From the energies observed above it can be concluded

that the release of the counter-ions is much easier for ZAN, followed by ZGN and lastly

ZNN. However, the E_a values observed for ZGN and ZNN are within the same error

margins hence cannot quantitatively said to be different. These charge densities are

consistent with observed rate constants, and also with the observed activation energies.

The observed E_a values are in agreement with the rate constants that were calculated from

ion-exchange of tClAc using these three materials (see table 5.4).

5.5.4 Equilibrium

In order to obtain ion-exchange equilibrium parameters, eight tClAc solutions with concentrations equal to; 30, 35, 40, 45, 50, 60, 70 and 80 mM were prepared. NaOH was used to adjust the pH of all the solutions to 7.0 ± 0.2. Exactly 10 ml of each of these solutions were placed into 100 ml glass vials, followed by the addition of 0.1 g of the adsorbent (e.g. ZAN). The reactants were then stirred in a shaking water bath at 25 °C for 12 hrs, to allow the reactions to go to equilibria. Reactants were then filtered and the tClAc still remaining in the solution was quantified using HPLC. The same procedure was repeated using ZNN and ZGN.

The most frequently used approach for studying equilibrium uptake of ions consists of measuring the adsorption isotherms [238]. This represents the quantity of ion uptake (q) versus the equilibrium concentration of the ion in the solution. The uptake capacity is calculated using the expression below;

$$q_e = \frac{(C_i - C_e)V}{m}$$
Equation 5.8

where C_i and C_e are the initial and equilibrium concentrations; V is the volume of the solution and m is the mass of the adsorbent. It also corresponds to the equilibrium distribution of the ions, in this case tClAc, between the aqueous and solid phases at different concentrations. Equilibrium studies were conducted to determine the optimum conditions for maximum uptake of tClAc ion by the layered materials.

The Langmuir isotherm is one of the most frequently used model available in literature, and is frequently used to describe experimental data on adsorption.[239] The Langmuir equation is expressed by the following expression:

$$\frac{C_e}{q_e} = \frac{1}{Q^0 b} + \frac{C_e}{Q^0}$$
Equation 5.9

where C_e (mg/L) is the equilibrium concentration of the analyte, q_e is the anion exchange capacity at equilibrium (mg/g) and Q^0 (mg/g) and b (L/mg) are constants related to the loading and the energy of adsorption, respectively. Plots of C_e/q_e versus Ce are linear showing suitability of the proposed isotherm. The essential characteristics of Langmuir isotherm can be expresses in terms of the dimensionless parameter R_L which is defined by the following expression:

$$R_L = 1 / (1 + bC_0)$$
Equation 5.10
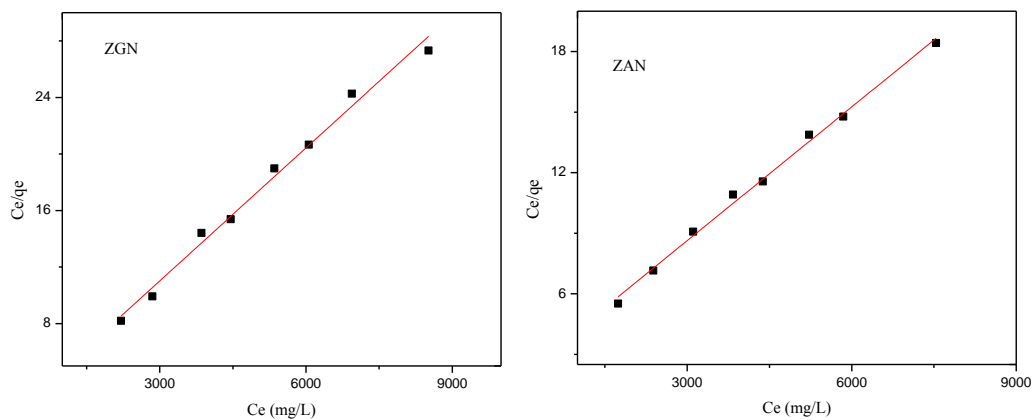
Figure 5.13. Langmuir plots for tClAc uptake using ZGN (left) and ZAN (right).

Table 5.7.The values of Langmuir constant Q^0, b and R_L for ZGN.

concentration (mM)	Q^0 (mg/g)	b	R_L	R^2
30			0.09	
35			0.08	
40			0.07	
45	318.15	0.001975	0.06	0.9899
50			0.06	
55			0.05	
60			0.05	
71.2			0.04	

Table 5.8. The values of Langmuir constant Q^0, b and R_L for ZAN.

concentration (mM)	Q^0 (mg/g)	b	R_L	R^2
30			0.13	
35			0.12	
40			0.10	
45	433.02	0.001314	0.09	0.9955
50			0.09	
55			0.08	
60			0.07	
71.2			0.06	

The removal of the tClAc anions was found to obey the Langmuir adsorption isotherm, and also that adsorption capacity was higher for ZAN (433 mg/g) than ZGN (318 mg/g). R_L values less than 1 indicate favorable adsorption[240,241]. The data obtained from ZNN uptake system could not be fit to Langmuir model, an R^2 value of 0.4 was obtained (see appendix D5). The high adsorption capacity of ZAN makes it even a better material than the other two.

5.6   Conclusion

Uptake efficiency of tClAc is improved by substitution of divalent metal cations with trivalent ones. Aluminum substitution resulted in a higher efficiency and higher rate constants. Thermal degradation of nitrates in ZNN, ZGN and ZAN produces NO_2. The decomposition behavior of the compounds can be applied to explain the observed rate constants. In exchange rate constants, decomposition temperatures and activation energies have been observed to be affected by charge densities of the metal cations. Cations with a higher charge density caused the lowering of decomposition temperature, and vice versa. Adsorption of tClAc using ZAN and ZGN followed Langmuir model, and ZAN had the highest adsorption capacity as compared to ZGN.

6. Methyl Orange adsorption using calcined materials

6.1 Introduction

Layered metal hydroxides have the ability to take up charged or neutral species from solutions through adsorption,[221] ion-exchange.[162]X-ray diffraction and differential scanning calorimetry measurements reveal that thermal treatment of layered materials induces dehydration, at temperatures up to 200 °C.[117]Dehydroxylation and loss of vaporizable anions such as acetates, carbonates, nitrates and oxalates occurs for temperatures between 200 and 500 °C,[237,242] and leads to the formation of poorly crystalline mixed oxides. For some layered materials spinels are formed. These calcined layered metal hydroxides have the ability to rehydrate on contact with water, taking up anions and reconstructing the original layered material structures, a property known as "memory effect".[21,119,243] This memory effect however is affected by calcination temperature and the metal composition of the precursor LDH. The extent and ease of the restructuring of the calcined LDHs is dependent on the properties of the matrix cations and also the temperature of calcination. Memory effect has been successful for compounds calcined at lower temperature.[244,245] For LDHs, it has been reported that higher temperature cause solid state diffusion of tetrahedrally coordinated trivalent metal into octahedral sites, occupied by divalent metals.[205] This diffusion of ions results in formation of stable spinels, and the compounds will not be able to regenerate their original layers. Depending on the application of these compounds, memory effect can be a constructive or destructive property. Memory effect is a destructive property for some

compounds especially in catalysis where the mixed oxides are used. Formation of layers from these compounds will deactivate the catalysts. However, this property can be constructively utilized for environmental remediation purposes by improving absorption properties of calcined layered metal hydroxides. The memory effect has been successfully utilized for the synthesis of I^-, ReO_4^-, and mixed $I^-/ReO4^-$ hydrotalcite.[246]

Textile and printing industries use dyes and pigments which end up being discharged in large amounts into wastewater.[128,247] Improper treatment and discharge of this wastewater is a threat to the environment, as these dyes when they degrade produce compounds that have toxic, mutagenic and carcinogenic effects on living organisms.[125] The need for cleaner and safer drinking water necessitates the need for more research aimed at finding new materials that can be applied removal of organic dyes from solution. Variety of materials have been investigated as adsorbents for the removal of dyes from water, some of them include sluge,[248] wheat straw,[249] banana pith,[250] fly ash, sugar cane dust,[251] montimorillonite,[252] zeolite,[253] bentonite[254] and kaolinite.[255]

Methyl orange (MO) is a model dye of a series of common water soluble azo dyes widely used in chemistry, paper and textile industries.[122] In this study investigated the adsorption properties of calcined zinc gallium and zinc aluminum LDHs.
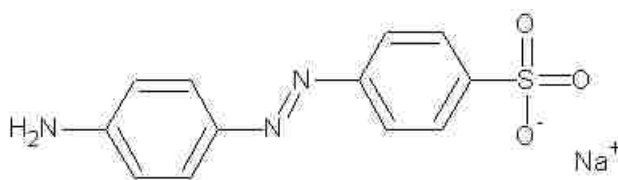
Figure 6.1. Methyl orange structure

6.2   Experimental

Zinc gallium hydroxy nitrate (ZGN) and zinc aluminum hydroxy nitrate (ZAN) were synthesized according to the methods already described in chapter 5.2.The layered compounds were then calcined for 2 hours, at 300 °C, 400 °C, 500 °C, 600 °C, and 800 °C. The resultant zinc gallium oxides were named ZGO3, ZGO4, ZGO5, ZGO6 and ZGO8, while zinc aluminum oxides were named ZAO3, ZAO4, ZAO5, ZAO6 and ZAO8.The numbers 3-8, after the letters ZAO or ZGO, are for the calcination temperature (T_{cal}).

Adsorption reactions were conducted by adding 0.1 g of the oxides into 25 ml 60 ppm MO solution in glass vial. The glass vials were then placed in a shaking water bath at 25 °C. The materials were allowed to react for one hour, and then filtered and dried at room temperature for analysis. For kinetics studies, 2 mg of the oxide was reacted with 3 ml of a 60 ppm MO solution, in a 1 cm square cuvette; the experiment was done at 25 °C. The powder oxide samples were wrapped using a thin Kimwipe^{TM} paper; to allow continuous data collection, without stopping the reactions for filtration purposes. A Polytetrafluoroethylene (PTFE) plastic mesh was used placed between the stirrer bar and the paper, as shown in Figure 6.3. The PTFE was used in order to protect the paper from damage. To prevent solvent evaporation, a para-film was used to seal the open end of the cuvette. Solutions were stirred using magnetic stirrer bars. Concentration change was monitored using UV-vis spectroscopy, by observing the changes in absorbance of the 464 nm MO peak (see figure 6.2).
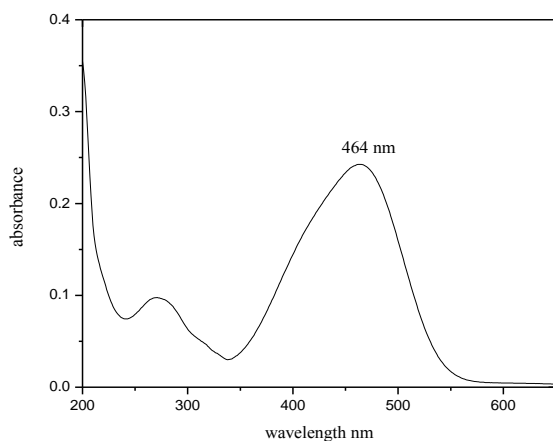
Figure 6.2. MO UV-vis profile showing the absorption bands at 464 nm.

A calibration curve (see appendix E 1.0) was constructed using concentrations ranging from 2-60 ppm. De-ionized water was used as the blank solution.
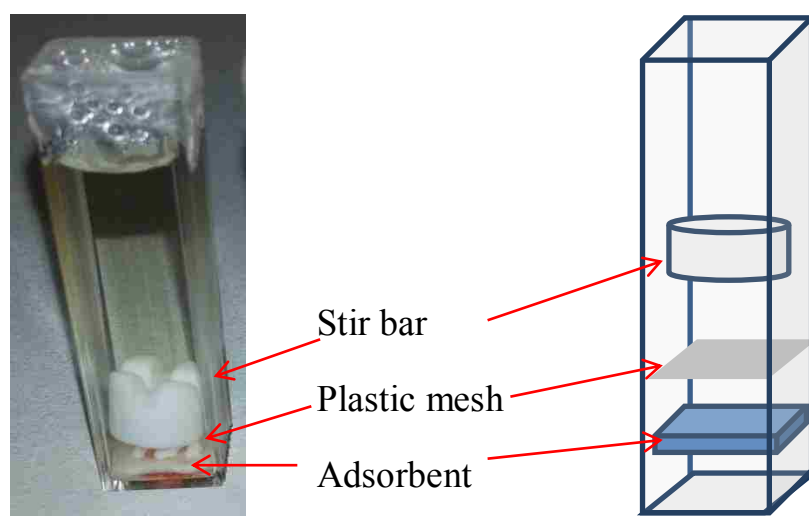
Figure 6.3. An actual picture (left) and a drawing (right) of the reaction cell used for monitoring MO adsorption reactions. The plastic cuvette on the left is covered with a para-film.

6.3   Characterization

The calcined materials were analyzed using a Rigaku powder X-ray diffraction machine with a CuK_α radiation with λ=1.5418 Å. Thermal analysis was conducted on a Netzsch TG 209 F1 machine coupled with a differential scanning calorimeter (TG/DSC). Aluminum oxide crucibles were used as sample holders and materials were heated under a constant flow of nitrogen at a heating rate of 20 °C min^{-1}. Fourier transform infrared spectra of the solid materials were obtained using Perkin-Elmer Spectrum 100 FT-IR spectrometer operated at a 2 cm^{-1} resolution. The FTIR spectra were recorded using a single reflection ATR accessory with a ZnSe prism (PIKE MIRacle, from PIKE technology), while the solutions were analyzed using a Perkin Elmer UV/vis lambda 25 machine.

6.4   Results and discussion
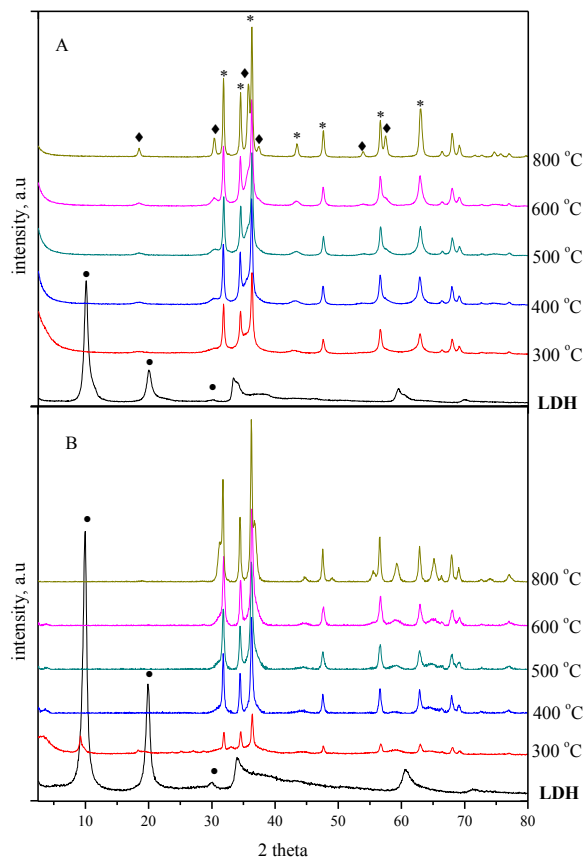
Figure 6.4.PXRD profiles of (A) ZGN LDH, ZGO3, ZGO4, ZGO5, ZGO6 and ZGO8, and (B)ZAN LDH, ZAO3, ZAO4, ZAO5, ZAO6 and ZAO8.The diamonds are showing the Bragg reflections due to the $ZnGa_2O_4$phase, the asterisks are Bragg reflections due to ZnO and the circles are for the 003, 006 and 009 reflections of the LDHs.

The PXRD profiles in figure 6.4 show the transformation of the LDHs into their

corresponding oxides. For ZGN decomposition, ZnO and $ZnGa_2O_4$ phases are observed;

the two phases are marked by asterisks and diamonds, respectively. The Bragg reflections

for the LDH completely disappeared at 300 $^{\circ}$C and above. $ZnGa_2O_4$ phase was clearly

observed at 800 $^{\circ}$C, although there is evidence of the phase also at 400 $^{\circ}$C. ZAN on the

other hand appeared to be more stable; no spinel formation can be observed. Calcination

of ZAN at 300 $^{\circ}$C did not result in a complete destruction of the layers. Although the

material was partially layered, ZnO started to form. At 400 $^{\circ}$C, the layers were

completely destroyed. After calcination, 0.1 g of the materials was reacted with 25 ml of

60 ppm MO solution, for one hour, at room temperature. Reactants were filtered and

analyzed using UV-vis spectroscopy; dried samples were analyzed using PXRD.

Figure 6.5. Pictorial evidence of the decolorization of MOusing ZAOs (left) and ZGOs (right). **The calcination temperatures are marked on the glass vials.**
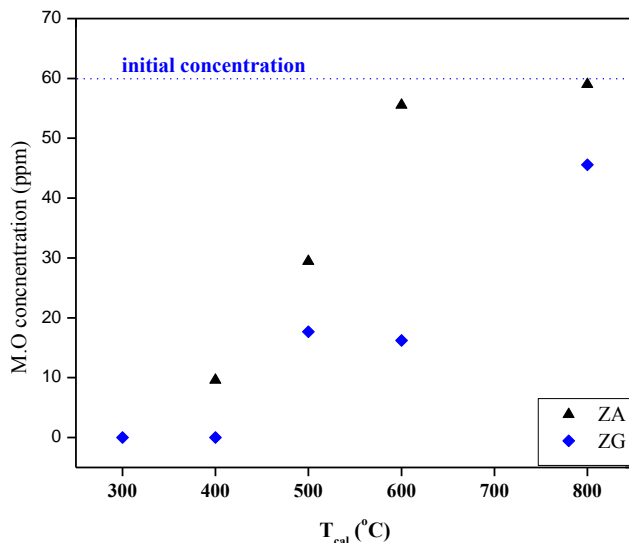
Figure 6.6. Effects of calcination temperature (Tcal) on MO concentration change, after reacting with ZGO and ZAO materials. Materials were reacted for one hour at room temperature.

Figures 6.5 and 6.6 show that ZGOs are better absorbents than ZAOs. ZGO3 and ZGO4 completely decolorized MO; the concentration was decreased from the initial 60 ppm (shown by the dotted line) to about 0 ppm (see Figure 6.6). The best ZAO material was ZAO4, which reduced the concentration to about 10 ppm. ZAO3 was not used for the adsorptions since it was still layered.

T_{cal} had the same effects on both materials. It can be seen that the adsorption efficiency of both materials decreased as a function of T_{cal}. However, for any given T_{cal}, ZGOs were always superior to ZAOs. The effects of increasing T_{cal} appeared to affect ZAOs more than they affect ZGOs; this is coming from the fact that ZAO6 reduced MO concentration to 56 ppm, which is about 8 % change, while ZGO6 reduced the

concentration to 20 ppm, which is about 67 % change. Concentration change was about 0 % when ZAO8 was used, while ZGO8 caused a 25 % concentration change. The PXRD profiles of the materials which were reacted with MO are shown in figure 6.7.
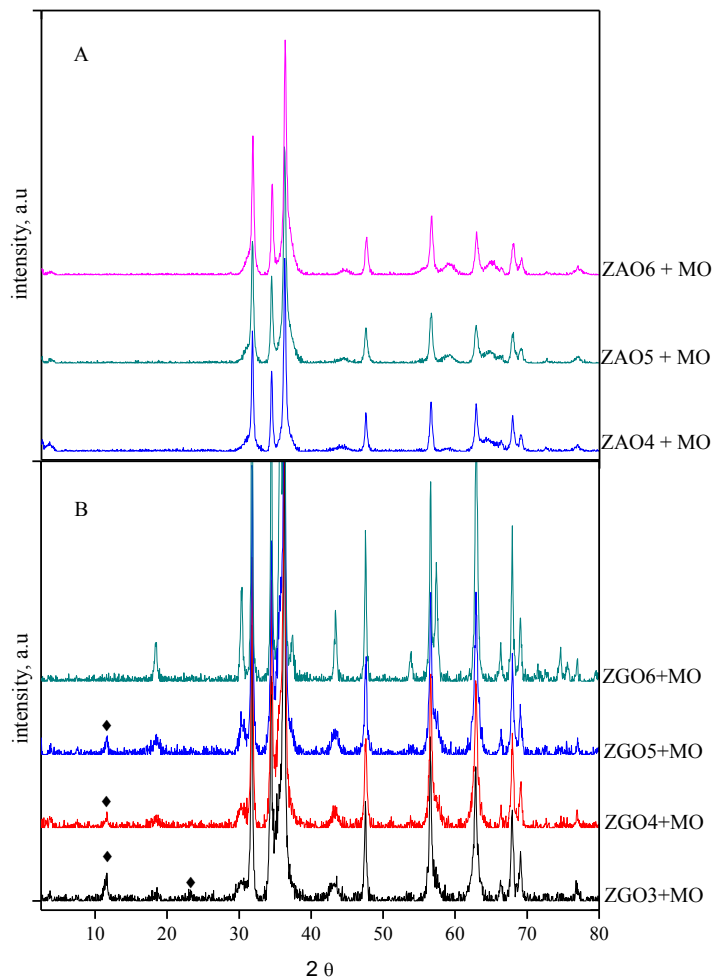
Figure 6.7.PXRD profiles of ZAOs (A) and ZGOs (B) after reacting with 60 ppm MO for an hour at room temperature. The diamonds in (B) are indicating a new phase formed after ZGOs reacted with MO.

The PXRD profiles of the oxides after reaction with MO reveal no changes for ZAOs, while new peaks are observed for ZGOs. The new peaks (marked by diamonds) are observed at 2 theta angles equal to 11.5 ° and 23.1 °. The position of the new peaks corresponds to d-spacings equal to 7.6Å and 3.8 Å, respectively. These two equally spaced reflections likely indicate the restructuring of the layered material. The restructuring was only to a small extent, probably because of the low dye concentration (60 ppm). The reflections at 11.5 ° and 23.1 ° decreased in intensity as the calcination temperature increased; no new reflections were observed for ZG8.

Thermal transformation of some LDHs, such as MgAl-, NiFe- and CoAl-LDHs, into their corresponding oxides (NiO, MgO, CoO) and spinels ($MgAl_2O_4$, $NiAl_2O_4$, $NiFe_2O_4$, $CoAl_2O_4$) has been reported to take place topotactically.[256]ZnAl-LDH compounds on the other hand have been reported to transform into oxides using a different mechanism.[256]Using ^{27}Al MAS NMR, Zhao et al.[205] observed that upon thermal treatment, $Al(OH)_6$ octahedra in the ZnAl-LDH layers are destroyed, releasing Al^{3+} cations into the gallery space. The released Al^{3+}cations then adopt a tetrahedral coordination with O atoms. Increasing calcination temperature resulted in an increase in the occupancy of the tetrahedral sites occupied by Al^{3+}, suggesting that Al^{3+} in the amorphous phase migrates into ZnO-like lattices. As temperature increases, Al^{3+}can move from the ZnO-like lattice to form the $ZnAl_2O_4$ spinel. Unlike ZnAl, ZnGa compounds appeared to start forming the spinel at a much lower temperature (see figure 6.4A). This might suggest that the decomposition mechanism followed by ZnGa compounds is different from that of ZnAl compounds. Ga^{3+} has a cationic radius of 0.62 Å when octahedrally coordinated, and is larger than the octahedrally coordinated Al^{3+},

which has a cationic radius of 0.53 Å.[257]This size difference might negatively affect lability of Ga^{3+}cations relative to that of Al^{3+}cations. If Ga^{3+} is not as labile, it will form without first migrating into the gallery space, thus making the spinel formation faster.

After observing that ZGO3 was the most efficient material, we then conducted some pH dependent kinetics studies. The reactions were performed in a cuvette as was described in section 6.2.

6.4.1 Kinetics

The reaction progress was monitored at five pH values; 4.5, 5.8, 6.7, 7.3 and 8.3. The change in absorbance was changed into concentration after making a calibration curve. The extent of reaction (α) was determined using the expression below;

$$\alpha = \frac{C_0 - C_t}{C_0} \qquad \textbf{Equation 6.1}$$

where C_0 and C_t are the initial MO concentration and remaining MO concentration at time t.
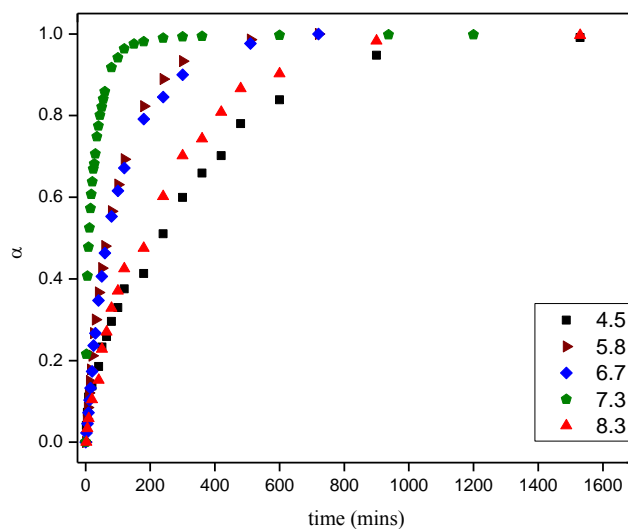
Figure 6.8.Plot of extent of reaction against time for the adsorption of MO using ZGO3, at different pH values.

It can be seen that adsorption was slowest at pH 4.5 and 8.3, moderate at 5.8 and 6.7 and fastest 7.3. The data shown in figure 6.8 were fit to Avrami Eroféev, Parabolic, modified-Freundlich and the first-order kinetic models. These models have been introduced previously in chapter 5.5.2.
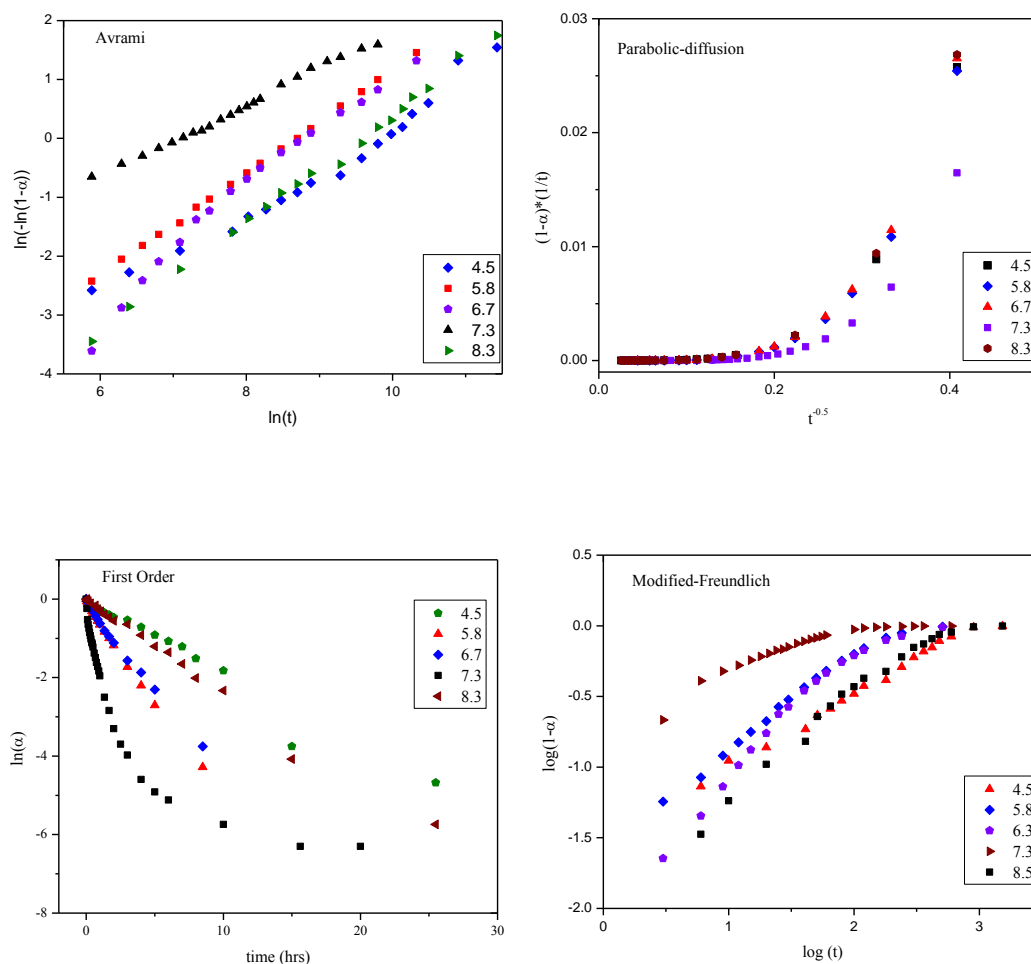
Figure 6.9.Plots of kinetic equations of (a) Avrami model, (b) parabolic diffusion, (c) first order kinetics model, and (d) the modified Freundlich model for the adsorption of MO at different pH values using calcined ZGN.

The trendlines for these linear fits were omitted for clarity purposes. Relative to the other models, the Avrami-Eroféev model provides a reasonable fit. Fitting data to some of these models require caution, as some fits might produce statistically acceptable values which are, however, chemically incorrect. Since we noticed some of our materials regenerated to some extent, during the adsorption, it would thus be expected that the data

would not fit to a single model. Treatment of solid state kinetics has been done using a scheme proposed by Avrami, separating overall reaction progress into separate stages.[92,170] This scheme makes use of the shape of the double-logarithm plots, i.e. plots of $\ln(-\ln(1-\alpha))$ versus $\ln(t)$; the slope (m)of this plot can reveal information about the reaction mechanism.[89,258]In order to reveal all the steps taking place we plotted the double-logarithm plots for each profile separately.
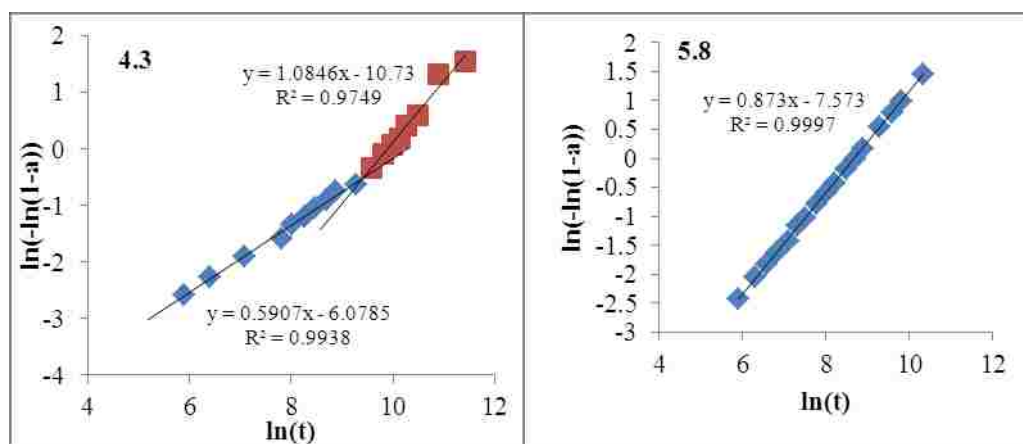
Figure 6.10.Double-logarithm plots for data collected at pH=4.3 and 5.8, using ZGO3 as adsorbent.
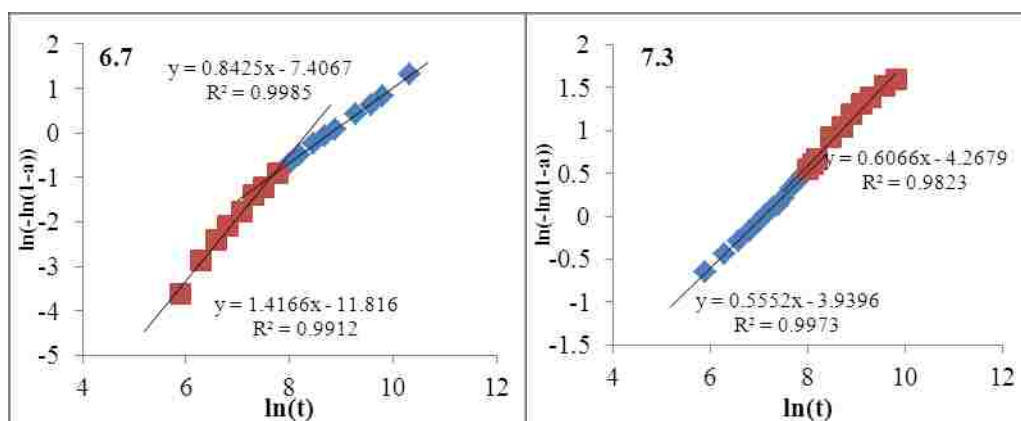
Figure 6.11.Double-logarithm plots for data collected at pH=6.7 and 7.3, using ZGO3 as adsorbent.
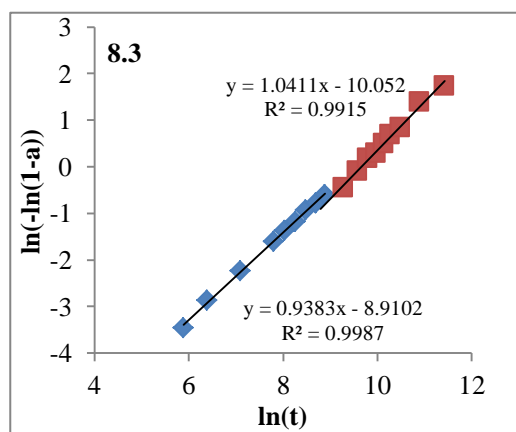
Figure 6.12.Double-logarithm plots for data collected at pH=8.3, using ZGO3 as adsorbent.

The breaks in plots shown in figure 6.10-6.12 suggest that the reaction mechanism is changing as the reaction progresses. This would also suggest that these reactions cannot be fit to a single model. The formation of layered metal hydroxides and also their ion-exchange reactions are believed to undergo dissolution-reprecipitation mechanism;[165,190,259] a process which will be affected by the pH of the reaction media. The mechanisms obtained from the double-logarithm plots are summarized in the table 6.1 below;

Table 6.1. Effect of pH on the slopes of the double-logarithm plots.

pH	m_1	m_2
4.3	0.6	1.0
5.8	0.9	
6.7	1.4	0.8
7.3	0.5	0.6
8.3	0.9	1.0

The slopes (m_1 and m_2) correspond to the gradients of the first and second stage, respectively. The slopes observed for all the pH values, except pH=6.7, ranged from 0.5-1.0. Fogg et al.[94] observed m values around 1.0 and suggested a two dimensional diffusion-controlled growth model followed by an instantaneous nucleation. The range $0.5 < m < 1.0$ would indicate contributions from both diffusion and nucleation processes, while m=1.4 indicate nucleation dependent reaction mechanism.[87] The summary of the other fits are shown in table 6.2.

Table 6.2. Rate constants and R^2 values obtained after fitting to several models.

Kinetic parameter	pH = 4.3	5.8	6.7	7.3	8.3
First-Order $\ln(C_t/C_o)=k_d t$					
k_d T	0.193	0.5095	0.445	0.337	0.234
R^2	0.968	0.996	0.992	0.707	0.99
Modified-Freundlich $\log(1-C_t/C_o)=\log(k_d) + a\log(t)$					
k_d	0.0322	0.0341	0.0153	0.2837	0.0158
a	0.501	0.609	0.772	0.242	0.64
R^2	0.987	0.965	0.933	0.805	0.95
Parabolic diffusion model $(1-C_t/C_o)/t=k_d t^{-0.5}+a$					
k_d	0.05	0.145	0.1508	0.097	0.0527
a	-0.0036	-0.0191	-0.0198	-0.0113	-0.0037
R^2	0.71884	0.65123	0.65318	0.53948	0.7209

The First-order data revealed that adsorptions at pH 5.8 and 6.7 are the ones best described by this model, with R^2 values equal to 0.996 and 0.991, respectively. The data obtained at pH 7.3, 8.3 and 4.5 gave R^2 values of 0.707, 0.989 and 0.968, respectively. None of that data obtained at all the pH values could fit the Modified-Freundlich model well; R^2 values 0.987, 0.965, 0.933, 0.805 and 0.950, for pH = 4.5, 5.8, 6.7, 7.3, 8.3, respectively. The Modified Freundlich models describe the adsorption onto the flat surface with the heterogeneous sites by diffusion process. The data which was fit to the Avrami-Eroféev revealed that there was a change in mechanisms as the reactions progress; this is shown by the slight bending of the plots as α increases. The slopes obtained were also changing with pH. These *m* values suggest that the adsorption

reactions were both diffusion and nucleation dependent. R^2 values for the parabolic model were poor, all values ranged from 0.539 to 0.720.

6.5   Conclusion

Calcined ZGN compounds are better MO adsorbents that calcined ZAN compounds. Thermal decomposition of ZGN resulted in the formation of the spinel $ZnGa_2O_3$ and ZnO, while only ZnO was observed for the ZAN-LDH. The memory effect was observed for the low-temperature-calcined ZGOs. ZGO6 and ZGO8 did not show any reconstruction. Methyl orange adsorption efficiency was best at neutral pH and decreased at higher and lower pH; the order of adsorption rates as a function of pH is: 7.3 > 6.7 > 5.8 > 8.3 > 4.3. The adsorption of the dye could best be described using the Avrami Eroféev model with R^2 ranging from 0.964 to 0.999 for all the pH conditions used.

7.0   Future Work

1.   With the help of ^{27}Al MAS NMR spectroscopy, Zhao et al.[205] proposed a mechanism for the formation $ZnAl_2O_4$ from ZnAl-LDH, which we applied in order to explain the occurrence of $ZnGa_2O_4$ from ZnGa-LDH. In order to have a clear understanding of the mechanism, it would be useful to also apply $^{69/71}$Ga NMR spectroscopy and compare the results alongside those for ^{27}Al MAS NMR spectroscopy. Solid state NMR spectroscopy has been be utilized to study variations in site occupancy of ^{27}Al in $ZnAl_2O_4$. The position of the NMR peak corresponding to the tetrahedral coordination will be different from that resulting from an octahedrally coordinated cation. The peak intensity will also vary depending with the amount of the cations in that particular coordination; peak position and intensity can thus be used to reveal the LDH to mixed metal oxide to spinel mechanism. The study will also require the use of high-resolution transmission electron microscopy (HRTEM).HRTEM is a powerful tool for materials characterization; it can provide real-space images with a resolution down to 0.1 nm.[205] It has been used to monitor structural changes such as nucleation processes and phase evolution during thermal decomposition of layered metal hydroxides.

Understanding the mechanistic formation of $ZnGa_2O_4$ from LDHs is also important since the spinel is a potential material for reflective optical coatings in aerospace applications[260] and ultraviolet-transport electro conductive oxide.[261] Revealing the mechanism will help improve the synthesis of the spinel for its targeted application.

2.   We attempted to do some photocatalytic degradation studies on the 6-chloro nicotinic acid. The acid is a degradation product of imidacloprid, a pesticide; it has been proved to cause colon collapse disorder (CCD).[262,263]The aim of the study was to use metal oxides for the mineralization of the acid.

We stopped the work because we could not reproduce catalyst using the method proposed by Carja et al.[157]. They calcined ZnAl-LDH, and then regenerated it using a solution titanium oxysulphate. Upon regeneration they showed that titanium oxide (anatase) will also be incorporated in the fully regenerated layered structure. Their material reconstructed fully within 30 mins at room temperature. The material we synthesized (Zn_2Al-nitrate) did not regenerate, and also no anatase was deposited on the calcined material. We could try to explore other materials which can easily regenerate in the presence of titanium oxysulphate. After successful regeneration we will then check whether anatase has been deposited on the reconstructed layers. The work will require comparative studies with the four materials that follow;

(i)   Pure LDH with no anatase

(ii)   Calcined oxide of the LDH with no anatase

(iii)   Regenerated LDH with anatase deposited and

(iv)   Pure anatase.

The solid phase analysis will require the use of mainly FTIR, PXRD (for the identification of phases), TEM (for the location of crystallites) and Rietveld analysis for the quantification of all the phases present. Solution phase analysis will require UV-vis analysis (quantification of 6-CNA) and HPLC (presence of new compounds after degradation).

Bibliography

(1)   Rives, V. *Layered Double Hydroxides: Present and Future*; Nova Science: New York, 2001.

(2)   Khan, A. I.; O'Hare, D. *Journal of Materials Chemistry***2002**, *12*, 3191–3198.

(3)   Allmann, R. *Acta Crystallographica Section B***1968**, *24*, 972–977.

(4)   Taylor, H. *Mineralogy Magazine***1969**, *37*, 339.

(5)   Evans, D.; Slade, R. T. In *Layered Double Hydroxides SE - 5*; Duan, X.; Evans, D., Eds.; Springer Berlin Heidelberg, 2006; Vol. 119, pp. 1–87.

(6)   Arizaga, G.; Satyanarayana, K.; Wypych, F. *Solid State Ionics***2007**, *178*, 1143–1162.

(7)   Taibi, M.; Ammar, S.; Jouini, N.; Fiévet, F. *Journal of Physics and Chemistry of Solids***2006**, *67*, 932–937.

(8)   Shinoda, K.; Aikawa, N. *Physics and Chemistry of Minerals***1998**, *25*, 197–202 LA – English.

(9)   Catti, M.; Ferraris, G.; Hull, S.; Pavese, A. *Physics and Chemistry of Minerals***1995**, *22*, 200–206 LA – English.

(10)   Choy, J. *Materials Letters***1998**, *34*, 356–363.

(11)   Ghose, S. *Acta Crystallographica***1964**, *17*, 1051–1057.

(12)   Rajamathi, J. T.; Britto, S.; Rajamathi, M. *Journal Chemical Sciences***2005**, *117*, 629–633.

(13)   Yamanaka, S.; Sako, T.; Seki, K.; Hattori, M. *Solid State Ionics***1992**, *53–56, Par*, 527–533.

(14)   Pereira, D. C.; Faria, D. L. A. De; Constantino, V. R. L. *Journal of Brazilian Chemical Society***2006**, *17*, 1651–1657.

(15)   Kandare, E.; Hossenlopp, J. M. *The Journal of Physical Chemistry B***2005**, *109*, 8469–75.

(16)   Stählin, W.; Oswald, H. R. *Acta Crystallographica Section B***1970**, *26*, 860–863.

(17)   Newman, S. P.; Jones, W. *Journal of Solid State Chemistry***1999**, *148*, 26–40.

(18)   Lin, Y.-H.; Adebajo, M. O.; Frost, R. L.; Kloprogge, J. T. *Journal of Thermal Analysis and Calorimetry***2005**, *81*, 83–89 LA – English.

(19)   Meyn, M.; Beneke, K.; Lagaly, G. *Inorganic Chemistry***1993**, *32*, 1209–1215.

(20)   Fudala, Å.; Pálinkó, I.; Hrivnák, B.; Kiricsi, I. *Journal of Thermal Analysis and Calorimetry***1999**, *56*, 317–322.

(21)   Marchi, A. J.; Apesteguía, C. R. *Applied Clay Science***1998**, *13*, 35–48.

(22)   Besserguenev, A. V; Fogg, A. M.; Francis, R. J.; Price, S. J.; Hare, D. O. *Chemistry of Materials***1997**, *2*, 241–247.

(23)   Thiel, J. P.; Chiang, C. K.; Poeppelmeier, K. R. *Chemistry of Materials***1993**, *5*, 297–304.

(24)   Williams, G. R.; Fogg, A. M.; Sloan, J.; Taviot-Guého, C.; O'Hare, D. *Dalton Transactions***2007**, *2*, 3499–506.

(25)   Trave, A.; Selloni, A.; Goursot, A.; Tichit, D.; Weber, J. *The Journal of Physical Chemistry B***2002**, *106*, 12291–12296.

(26)   Gago, S.; Pillinger, M.; Valente, A. a; Santos, T. M.; Rocha, J.; Gonçalves, I. S. *Inorganic Chemistry***2004**, *43*, 5422–31.

(27)   Thevenot, F.; Szymanski, R.; Chaumette, P.; Fran, I.; Prrau, A. D. B.; Cedex, R. *Clay and Clay Minerals***1989**, *37*, 396–402.

(28)   Gutmann, N.; Müller, B. *Journal of Solid State Chemistry***1996**, *122*, 214–220.

(29)   Kaneyoshi, M.; Jones, W. *Journal of Materials Chemistry***1999**, *9*, 805–811.

(30)   Cavani, F.; Trifirò, F.; Vaccari, A. *Catalysis Today***1991**, *11*, 173–301.

(31)   Frost, R. L.; Erickson, K. L. *Journal of Thermal Analysis and Calorimetry***2004**, *76*, 217–225.

(32)   Hofmeister, W.; Platen, H. Von *Crystallography Reviews***1992**, *3*, 3–26.

(33)   Rabenau, A. *Angewandte Chemie International Edition in English***1985**, *24*, 1026–1040.

(34)   Stählin, W.; Oswald, H. R. *Journal of Solid State Chemistry***1971**, *3*, 256–264.

(35)   Gomes Silva, C.; Bouizi, Y.; Fornés, V.; García, H. *Journal of the American Chemical Society* **2009**, *131*, 13833–9.

(36)   Gunjakar, J. L.; Kim, T. W.; Kim, H. N.; Kim, I. Y.; Hwang, S.-J. *Journal of the American Chemical Society* **2011**, *133*, 14998–15007.

(37)   Martin, M. J. S.; Villa, M. V; Sanchez-Camazano, M. *Clay and Clay Minerals* **1999**, *47*, 777–783.

(38)   Reichle, W. T.; Kang, S. Y.; Everhardt, D. S. *Journal of Catalysis* **1986**, *101*, 352–359.

(39)   Crepaldi, E. L.; Pavan, P. C.; Valim, J. B. *Journal of Materials Chemistry* **2000**, *10*, 1337–1343.

(40)   Komarneni, S.; Kozai, N.; Roy, R. *Journal of Materials Chemistry* **1998**, *8*, 1329–1331.

(41)   Gardner, E.; Huntoon, K. M.; Pinnavaia, T. J. *Advanced Materials* **2001**, *13*, 1263–1266.

(42)   Carlino, S.; Hudson, M. J. *Journal of Materials Chemistry* **1995**, *5*, 1433–1442.

(43)   Kooli, F.; Rives, V.; Ulibarri, M. A. *Inorganic Chemistry* **1995**, *34*, 5114–5121.

(44)   Aloisi, G. G.; Costantino, U.; Elisei, F.; Latterini, L.; Natali, C.; Nocchetti, M. *Journal of Materials Chemistry* **2002**, *12*, 3316–3323.

(45)   You, Y.; Zhao, H.; Vance, G. F. *Journal of Materials Chemistry* **2002**, *12*, 907–912.

(46)   Tagaya, H.; Ogata, A.; Kuwahara, T.; Ogata, S.; Karasu, M.; Kadokawa, J.; Chiba, K. *Microporous Materials* **1996**, *7*, 151–158.

(47)   Adachi-Pagano, M.; Forano, C.; Besse, J.-P. *Chemical Communications* **2000**, *0*, 91–92.

(48)   Tao, F.; Grass, M. E.; Zhang, Y.; Butcher, D. R.; Renzas, J. R.; Liu, Z.; Chung, J. Y.; Mun, B. S.; Salmeron, M.; Somorjai, G. A. *Science* **2008**, *322*, 932–934.

(49)   Thompson, M. E. *Chemistry of Materials* **1994**, *6*, 1168–1175.

(50)   An, Z.; Lu, S.; He, J.; Wang, Y. *Langmuir* **2009**, *25*, 10704–10710.

(51)   Fuertes, A. B.; Pico, F.; Rojo, J. M. *Journal of Power Sources* **2004**, *133*, 329–336.

(52)   Wypych, F.; Bubniak, G. A.; Halma, M.; Nakagaki, S. *Journal of Colloid and Interface Science***2003**, *264*, 203–207.

(53)   Choy, J.-H.; Kwak, S.-Y.; Park, J.-S.; Jeong, Y.-J.; Portier, J. *Journal of the American Chemical Society***1999**, *121*, 1399–1400.

(54)   Tamaki, H.; Zhong, Z. J.; Matsumoto, N.; Kida, S.; Koikawa, M.; Achiwa, N.; Hashimoto, Y.; Okawa, H. *Journal of the American Chemical Society***1992**, *114*, 6974–6979.

(55)   Kanezaki, E. *Journal of Materials Science***1995**, *30*, 4926–4929.

(56)   Biswick, T.; Jones, W.; Pacuła, A.; Serwicka, E. *Journal of Solid State Chemistry***2006**, *179*, 49–55.

(57)   Li, P.; Xu, Z. P.; Hampton, M. a; Vu, D. T.; Huang, L.; Rudolph, V.; Nguyen, A. V *The Journal of Physical Chemistry C***2012**, *116*, 10325–10332.

(58)   Rouba, S.; Rabu, P.; Drillon, M. *Journal of Solid State Chemistry***1995**, *118*, 28–32.

(59)   Tagaya, H.; Sasaki, N.; Morioka, H.; Kadokawa, J. *Molecular Crystals and Liquid Crystals Science and Technology. Section A. Molecular Crystals and Liquid Crystals***2000**, *341*, 413–418.

(60)   Shishido, T.; Yamamoto, M.; Li, D.; Tian, Y.; Morioka, H.; Honda, M.; Sano, T.; Takehira, K. *Applied Catalysis A: General***2006**, *303*, 62–71.

(61)   Sigoli, F. a.; Davolos, M. R.; Jafelicci, M. *Journal of Alloys and Compounds***1997**, *262-263*, 292–295.

(62)   Markov, L.; Petrov, K.; Petkov, V. *Thermochimica Acta***1986**, *106*, 283–292.

(63)   Fujita, W.; Awaga, K. *Inorganic chemistry***1996**, *2*, 1915–1917.

(64)   Xu, R.; Zeng, H. C. *Journal of Physical Chemistry***2003**, *107*, 926–930.

(65)   Rajamathi, M.; Kamath, P. V. *International Journal of Inorganic Materials***2001**, *3*, 901–906.

(66)   Kaupp, G.; Reza Naimi-Jamal, M.; Schmeyers, J. *Tetrahedron***2003**, *59*, 3753–3760.

(67)   Manzini, S. S.; Coville, N. J. *Inorganic Chemistry Communications***2004**, *7*, 676–678.

(68)   Möhmel, S.; Kurzawski, I.; Uecker, D.; Müller, D.; Geßner, W. *Crystal Research and Technology***2002**, *37*, 359–369.

(69)   Tao, Q.; Zhang, Y.; Zhang, X.; Yuan, P.; He, H. *Journal of Solid State Chemistry***2006**, *179*, 708–715.

(70)   Petrov, K.; Lyubchova, A.; Markov, L. *Polyhedron***1989**, *8*, 1061–1067.

(71)   Henrist, C.; Mathieu, J.-P.; Vogels, C.; Rulmont, a; Cloots, R. *Journal of Crystal Growth***2003**, *249*, 321–330.

(72)   Rivera, J. a.; Fetter, G.; Bosch, P. *Microporous and Mesoporous Materials***2006**, *89*, 306–314.

(73)   Komarneni, S.; Li, Q. H.; Roy, R. *Journal of Materials Research***2011**, *11*, 1866–1869.

(74)   Hussein, M. Z. B.; Zainal, Z.; Ming, C. Y. E. N. *Journal of Materials Science Letters***2000**, *9*, 879–883.

(75)   Poul, L.; Jouini, N.; Fivet, F.; Fie, F. *Chemistry of Materials***2000**, *12*, 3123–3132.

(76)   He, J.; Wei, M.; Li, B.; Kang, Y.; Evans, D.; Duan, X. In *Layered Double Hydroxides SE - 6*; Duan, X.; Evans, D., Eds.; Springer Berlin Heidelberg, 2006; Vol. 119, pp. 89–119.

(77)   Morel-Desrosiers, N.; Pisson, J.; Israeli, Y.; Taviot-Gueho, C.; Besse, J.-P.; Morel, J.-P. *Journal of Materials Chemistry***2003**, *13*, 2582–2585.

(78)   Vyazovkin, S.; Wight, C. A. *Annual Review of Physical Chemistry***1997**, *48*, 125–149.

(79)   Maciejewski, M.; Reller, A. *Thermochimica Acta***1987**, *110*, 145–152.

(80)   Vyazovkin, S. *International Journal of Chemical Kinetics***1996**, *28*, 95–101.

(81)   Vyazovkin, S.; Sbirrazzuoli, N. *Macromolecules***1996**, *29*, 1867–1873.

(82)   Vyazovkin, S. *International Reviews in Physical Chemistry***2000**, *19*, 45–60.

(83)   Simon, P. *Journal of Thermal Analysis and Calorimetry***2004**, *76*, 123–132.

(84)   Budrugeac, P.; Homentcovschi, D.; Segal, E. *Journal of Thermal Analysis and Calorimetry***2001**, *63*, 457–463.

(85)   Budrugeac, P.; Homentcovschi, D.; Segal, E. *Journal of Thermal Analysis and Calorimetry* **2001**, *63*, 465–469.

(86)   Budrugeac, P.; Popescu, C.; Segal, E. *Journal of Thermal Analysis and Calorimetry* **2001**, *64*, 821–827.

(87)   Majoni, S.; Hossenlopp, J. M. *The Journal of Physical Chemistry A* **2010**, *114*, 12858–69.

(88)   Tarasov, K. a; O'Hare, D.; Isupov, V. P. *Inorganic chemistry* **2003**, *42*, 1919–27.

(89)   Lianxi, H.; Heng, W.; Xin, W. *Journal of Alloys and Compounds* **2012**, *513*, 343–346.

(90)   Jabal, A. A. B. O.; Tan, I. S. A. M.; Man, Z.; Maitra, S. *Journal of Engineering Science and Technology* **2009**, *4*, 364–373.

(91)   Williams, G. R.; Crowder, J.; Burley, J. C.; Fogg, A. M. *Journal of Materials Chemistry* **2012**, *22*, 13600–13611.

(92)   Fogg, A. M.; Price, S. J.; Francis, R. J.; O'Brien, S.; O'Hare, D. *Journal of Materials Chemistry* **2000**, *10*, 2355–2357.

(93)   Avrami, M. *Journal of Chemical Physics* **1939**, *117*, 1103–1112.

(94)   Fogg, A. M.; Hare, D. O. *Chemistry of Materials* **1999**, *11*, 1771–1775.

(95)   Hancock, J. D.; Sharp, J. H. *Journal of the American Ceramic Society* **1972**, *55*, 74–77.

(96)   Yang, J.; Han, Y.; Park, M.; Park, T.; Hwang, S.; Choy, J. *Chemistry of Materials* **2007**, *19*, 2679–2685.

(97)   Kithome, M.; Paul, J. W.; Lavkulich, L. M.; Bomke, A. A. Kinetics of Ammonium Adsorption and Desorption by the Natural Zeolite Clinoptilolite **1998**, *62*, 622–629.

(98)   Sivaraj, R. *International journal of Engineering Science and Technology* **2010**, *2*, 2040–2050.

(99)   Wang, C. J.; O'Hare, D. *Journal of Materials Chemistry* **2012**, *22*, 23064–23070.

(100)   Rojas, R.; Barriga, C.; Angeles Ulibarri, M.; Malet, P.; Rives, V. *Journal of Materials Chemistry* **2002**, *12*, 1071–1078.

(101)   Reichle, W. T. *Journal of Catalysis* **1985**, *94*, 547–557.

(102) Kappenstein, C.; Černák, J.; Brahmi, R.; Duprez, D.; Chomič, J. *Thermochimica Acta***1996**, *279*, 65–76.

(103) Li, F.; Jin, L.; Han, J.; Wei, M.; Li, C. *Industrial & Engineering Chemistry Research***2009**, *48*, 5590–5597.

(104) Chubar, N. *Journal of Colloid and Interface Science***2011**, *357*, 198–209.

(105) Rajamathi, J. T.; Britto, S.; Rajamathi, M. *Journal of Chemical Sciences***2005**, *117*, 2005.

(106) Gago, S.; Pillinger, M.; Santos, T. M.; Gonçalves, I. S. *Journal Ceramics-Silikáty***2004**, 155–158.

(107) Lochan, R.; Sengupta, P. *Applied Clay Science***1998**, *13*, 21–34.

(108) Hanson, M. L.; Solomon, K. R. *Environmental Pollution***2004**, *130*, 385–401.

(109) Zhang, P.; Lapara, T. M.; Goslan, E. H.; Xie, Y.; Parsons, S. a; Hozalski, R. M. *Environmental science & technology***2009**, *43*, 3169–75.

(110) Wu, C.; Wei, D.; Fan, J.; Wang, L. *Chemosphere***2001**, *44*, 1293–7.

(111) Církva, V.; Žabová, H.; Hájek, M. *Journal of Photochemistry and Photobiology A: Chemistry***2008**, *198*, 13–17.

(112) Wang, X.; Ning, P.; Liu, H.; Ma, J. *Applied Catalysis B: Environmental***2010**, *94*, 55–63.

(113) Gherardini, L.; Michaud, P. A.; Panizza, M.; Comninellis, C.; Vatistas, N. *Journal of Electrochemical Society***2001**, *148*, D78–D82.

(114) Scialdone, O.; Galia, A.; Gurreri, L.; Randazzo, S. *Electrochimica Acta***2010**, *55*, 701–708.

(115) Elving, P. J.; Tang, C.-S. *Journal of the American Chemical Society***1950**, *72*, 3244–3246.

(116) Elving, P. J.; Rosenthal, I.; Kramer, M. K. *Journal of the American Chemical Society***1951**, *73*, 1717–1722.

(117) Wong, F.; Buchheit, R. G. *Progress in Organic Coatings***2004**, *51*, 91–102.

(118) Mandal, S.; Lerner, D. a.; Marcotte, N.; Tichit, D. *Zeitschrift für Kristallographie***2009**, *224*, 282–286.

(119) Frunza, M.; Lisa, G.; Popa, M. I.; Miron, N. D.; Nistor, D. I. *Journal of Thermal Analysis and Calorimetry***2008**, *93*, 373–379.

(120) Valente, J. S.; Tzompantzi, F.; Prince, J.; Cortez, J. G. H.; Gomez, R. *Applied Catalysis B: Environmental***2009**, *90*, 330–338.

(121) Park, H.; Choi, W. *Journal of Photochemistry and Photobiology A: Chemistry***2003**, *159*, 241–247.

(122) Fan, J.; Guo, Y.; Wang, J.; Fan, M. *Journal of Hazardous Materials***2009**, *166*, 904–10.

(123) Semerjian, L.; Ayoub, G. M. *Advances in Environmental Research***2003**, *7*, 389–403.

(124) Ciardelli, G.; Corsi, L.; Marcucci, M. *Resources, Conservation and Recycling***2000**, *31*, 189–197.

(125) Jalil, A. a; Triwahyono, S.; Adam, S. H.; Rahim, N. D.; Aziz, M. A. a; Hairom, N. H. H.; Razali, N. A. M.; Abidin, M. a Z.; Mohamadiah, M. K. a *Journal of Hazardous Materials***2010**, *181*, 755–62.

(126) Wu, F.-C.; Tseng, R.-L. *Journal of Hazardous Materials***2008**, *152*, 1256–67.

(127) Belessi, V.; Romanos, G.; Boukos, N.; Lambropoulou, D.; Trapalis, C. *Journal of Hazardous Materials***2009**, *170*, 836–44.

(128) Hameed, B. H.; Ahmad, a. L.; Latiff, K. N. a. *Dyes and Pigments***2007**, *75*, 143–149.

(129) Wang, S.; Zhu, Z. H. *Journal of Hazardous Materials***2006**, *136*, 946–52.

(130) Mall, I. D.; Srivastava, V. C.; Agarwal, N. K.; Mishra, I. M. *Chemosphere***2005**, *61*, 492–501.

(131) Janssen, T. In *Aperiodic Crystals SE - 1*; Schmid, S.; Withers, R. L.; Lifshitz, R., Eds.; Springer Netherlands, 2013; pp. 1–9.

(132) Bragg, W. H.; Bragg, W. L. *Proceedings of the Royal Society A: Mathematical, Physical and Engineering Sciences***1913**, *88*, 428–438.

(133) Patterson, A. L. *Physical Review***1939**, *56*, 978–982.

(134) Britto, S.; Joseph, S.; Vishnu Kamath, P. *Journal of Chemical Sciences***2010**, *122*, 751–756.

(135)   Li, X. C. and X.-J. L. and Y. B. and C.-F. *Journal of Optics***2013**, *15*, 33001.

(136)   Wilkie, C. A. *Polymer Degradation and Stability***1999**, *66*, 301–306.

(137)   Jiang, D. D.; Yao, Q.; McKinney, M. A.; Wilkie, C. A. *Polymer Degradation and Stability***1999**, *63*, 423–434.

(138)   Marenich, A. V; Cramer, C. J.; Truhlar, D. G. *The journal of physical chemistry. B***2009**, *113*, 6378–96.

(139)   Rietveld, H. *Journal of Applied Crystallography***1969**, *2*, 65–71.

(140)   Walker, J. R.; Bish, D. L. *Clay and Clay Minerals***1992**, *40*, 319–322.

(141)   Friedel, P.; Jehnichen, D.; Bergmann, J.; Taut, T.; Haase, A. *International Centre for Diffraction Data***1999**, 593–600.

(142)   Gražulis, S.; Daškevič, A.; Merkys, A.; Chateigner, D.; Lutterotti, L.; Quirós, M.; Serebryanaya, N. R.; Moeck, P.; Downs, R. T.; Le Bail, A. *Nucleic acids research***2012**, *40*, D420–7.

(143)   Gražulis, S.; Chateigner, D.; Downs, R. T.; Yokochi, a F. T.; Quirós, M.; Lutterotti, L.; Manakova, E.; Butkus, J.; Moeck, P.; Le Bail, A. *Journal of Applied Crystallography***2009**, *42*, 726–729.

(144)   Guilmeau, E.; Chateigner, D.; Suzuki, T. S.; Sakka, Y.; Henrist, C.; Ouladdiaf, B. *Chemistry of Materials***2005**, *17*, 102–106.

(145)   Meneghini, C.; Dalconi, M. C.; Nuzzo, S.; Mobilio, S.; Wenk, R. H. *Biophysical Journal***2003**, *84*, 2021–9.

(146)   Sanchez-Bajo, F.; Cumbrera, F. L. *Journal of Applied Crystallography***1999**, *32*, 730–735.

(147)   Christman, R. F.; Norwood, D. L.; Millington, D. S.; Johnson, J. D.; Stevens, A. A. *Environmental Science & Technology***1983**, *17*, 625–628.

(148)   Lee, J.; Kim, E.-S.; Roh, B.-S.; Eom, S.-W.; Zoh, K.-D. *Environmental Monitoring and Assessment***2013**, 1–17.

(149)   Magnuson, M.; Kelty, C. *Analytical chemistry***2000**, *72*, 2308–12.

(150)   Krasner, S. W.; Wright, J. M. *Water Research***2005**, *39*, 855–864.

(151)   Chang, C.-Y.; Hsieh, Y.-H.; Hsu, S.-S.; Hu, P.-Y.; Wang, K.-H. *Journal of Hazardous Materials***2000**, *79*, 89–102.

(152) Nissinen, T. K.; Miettinen, I. T.; Martikainen, P. J.; Vartiainen, T. *Chemosphere***2002**, *48*, 9–20.

(153) Coleman, W. E.; Melton, R. G.; Kopfler, F. C.; Barone, K. a.; Aurand, T. a.; Jellison, M. G. *Environmental science & technology***1980**, *14*, 576–588.

(154) Wang, G. S.; Lai, S. P.; Huang, Y. T. *Water Science & Technology: Water Supply***2009**, *9*, 557.

(155) Xu, Y. H.; Zhang, H.; Chu, C. P.; Ma, C. A. *Journal of Electroanalytical Chemistry***2012**, *664*, 39–45.

(156) Hozalski, R. M. *Environmental science & technology***2004**, *38*, 6881–6889.

(157) Carja, G.; Nakajima, A.; Dranca, S.; Dranca, C.; Okada, K. *Journal of Physical Chemistry C***2010**, *114*, 14722–14728.

(158) Unnikrishnan, R.; Narayanan, S. *Journal of Molecular Catalysis A: Chemical***1999**, *144*, 173–179.

(159) Wang, X.; Rathore, R.; Songtipya, P.; Jimenez-Gasco, M. D. M.; Manias, E.; Wilkie, C. a. *Polymer Degradation and Stability***2011**, *96*, 301–313.

(160) Huang, W.; Zhang, H.; Pan, D. *AIChE Journal***2011**, *57*, 1936–1946.

(161) Morioka, H.; Tagaya, H.; Karasu, M.; Kadokawa, J.; Chiba, K. *Inorganic Chemistry***1999**, *38*, 4211–4216.

(162) Tezuka, S.; Chitrakar, R.; Sonoda, A.; Ooi, K.; Tomida, T. *Green Chemistry***2004**, *6*, 104–109.

(163) Bull, R. M. R.; Markland, C.; Williams, G. R.; O'Hare, D. *Journal of Materials Chemistry***2011**, *21*, 1822–1828.

(164) Chaparadza, A.; Hossenlopp, J. M. *Journal of Colloid and Interface Science***2011**, *363*, 92–97.

(165) Michael Rajamathi, P. V. K. *Journal of Power Sources***1998**, *70*, 118–121.

(166) Young, D. C. *Chemistry Computational Chemistry A Practical Guide for Applying Techniques to Real-World Problems*; 2001; Vol. 9, p. 111.

(167) Bober, L.; Kawczak, P.; Baczek, T. *International journal of molecular sciences***2012**, *13*, 6665–78.

(168) Wang, F.; Downton, M. *Journal of Physics B: Atomic, Molecular and Optical Physics* **2004**, *37*, 557–569.

(169) Zhenlan, Q.; Heng, Y.; Bin, Z.; Wanguo, H. *Colloids and Surfaces A: Physicochemical and Engineering Aspects* **2009**, *348*, 164–169.

(170) Evans, J. S. O.; Price, S. J.; Wong, H.; Hare, D. O.; June, R. *Journal of American Chemical Society* **1998**, *120*, 10837–10846.

(171) Khawam, A.; Flanagan, D. R. *The Journal of Physical Chemistry B* **2006**, *110*, 17315–28.

(172) Vyazovkin, S. *New Journal of Chemistry* **2000**, *24*, 913–917.

(173) White, D. R.; White, R. L. *Applied Spectroscopy* **2008**, *62*, 116–120.

(174) Vyazovkin, S.; Wight, C. A. *Thermochimica Acta* **1999**, *340–341*, 53–68.

(175) Holubová, J.; Èernošek, Z.; Èernošková, E. *Journal of Thermal Analysis and Calorimetry.* **2000**, *62*, 715–719.

(176) Strømme, K. O. *Thermochimica Acta* **1986**, *97*, 363–368.

(177) De Bruijn, T. J. W.; De Jong, W. A.; Van Den Berg, P. J. *Thermochimica Acta* **1981**, *45*, 315–325.

(178) Meyn, M.; Beneke, K.; Lagaly, C.; Chemie, A.; Kiel, U. *Inorganic chemistry* **1993**, 1209–1215.

(179) Smilgies, D. M. *Journal of Applied Crystallography* **2009**, *42*, 1030–1034.

(180) Biswick, T.; Jones, W.; Pacuła, A.; Serwicka, E.; Podobinski, J. *Solid State Sciences* **2009**, *11*, 330–335.

(181) Arizaga, G. G. C.; Mangrich, A. S.; da Costa Gardolinski, J. E. F.; Wypych, F. *Journal of colloid and interface science* **2008**, *320*, 168–76.

(182) Anan'ev, V.; Miklin, M. *Optical Materials* **2000**, *14*, 303–311.

(183) Johnsen, R. E.; Krumeich, F.; Norby, P. *Journal of Applied Crystallography* **2010**, *43*, 434–447.

(184) Ten Hulscher, T. E. M.; Cornelissen, G. *Chemosphere* **1996**, *32*, 609–626.

(185) Kressman, T. R. E. *Journal of Physical Chemistry* **1952**, *56*, 118–123.

(186)   Graul, T. W.; Li, M.; Schlenoff, J. B. *The Journal of Physical Chemistry B***1999**, *103*, 2718–2723.

(187)   Williams, G. R.; Dunbar, T. G.; Beer, A. J.; Fogg, A. M.; O'Hare, D. *Journal of Materials Chemistry***2006**, *16*, 1222–1230.

(188)   Gasser, M. S. *Colloids and surfaces. B, Biointerfaces***2009**, *73*, 103–9.

(189)   Rajamathi, J. T.; Britto, S.; Rajamathi, M. *Journal of Chemical Sciences***2005**, *117*, 629–633.

(190)   Rives, V.; Angeles Ulibarri, M. *Coordination Chemistry Reviews***1999**, *181*, 61–120.

(191)   Morel-Desrosiers, N.; Pisson, J.; Israeli, Y.; Taviot-Gueho, C.; Besse, J.-P.; Morel, J.-P. *Journal of Materials Chemistry***2003**, *13*, 2582.

(192)   Walton, R. I.; O'Hare, D. *The Journal of Physical Chemistry B***2001**, *105*, 91–96.

(193)   Masciocchi, N.; Corradi, E.; Sironi, A.; Moretti, G.; Minelli, G.; Porta, P. *Journal of solid state chemistry***131**, 252–262.

(194)   Kandare, E.; Chigwada, G.; Wang, D.; Wilkie, C. a.; Hossenlopp, J. M. *Polymer Degradation and Stability***2006**, *91*, 1781–1790.

(195)   Xue, M.; Chitrakar, R.; Sakane, K.; Ooi, K.; Kobayashi, S.; Ohnishi, M.; Doi, A. *Journal of Solid State Chemistry***2004**, *177*, 1624–1630.

(196)   Gatehouse, B. M.; Livingstone, S. E.; Nyholm, R. S. *Journal of the Chemical Society (Resumed)***1957**, *0*, 4222–4225.

(197)   Nakamoto, K. *Infrared and Raman Spectra of Inorganic and Coordination Compounds: Applications in coordination, organometallic, and bioinorganic chemistry*; Wiley, 1997; pp. 87–88.

(198)   Deacon, G. B.; Phillips, R. J. *Coordination Chemistry Reviews***1980**, *33*, 227–250.

(199)   Kooli, F.; Chisem, I. C.; Vucelic, M.; Jones, W. *Chemistry of Materials***1996**, *8*, 1969–1977.

(200)   Jirnenez-lopez, A.; Rodriguez-castellon, E.; Olivera-pastor, P.; Maireles-, P.; Tornlinson, A. A. G.; Jonesc, D. J.; Roziere, J. *Journal of Materials Chemistry***1993**, *3*, 303–307.

(201)   Nakamoto, K. *Infrared and Raman Spectra of Inorganic and Coordination Compounds: Theory and applications in inorganic chemistry*; Wiley, 2009.

(202) Prasanna, S. V; Kamath, P. V. *Journal of Colloid and Interface Science***2009**, *331*, 439–45.

(203) An, Z.; Lu, S.; Zhao, L.; He, J. *Langmuir : Journal of Surfaces and Colloids***2011**, *27*, 12745–50.

(204) Sideris, P. J.; Nielsen, U. G.; Gan, Z.; Grey, C. P. *Science* **2008**, *321* , 113–117.

(205) Zhao, X.; Zhang, F.; Xu, S.; Evans, D. G.; Duan, X. *Chemistry of Materials***2010**, *22*, 3933–3942.

(206) Gill, P.; Moghadam, T. T.; Ranjbar, B. *Journal of biomolecular techniques : JBT***2010**, *21*, 167–93.

(207) Androsch, R.; Stolp, M.; Radusch, H.-J. *Thermochimica Acta***1996**, *271*, 1–8.

(208) Duz, M. Z.; Tonbul, Y.; Baysal, a.; Akba, O.; Saydut, a.; Hamamci, C. *Journal of Thermal Analysis and Calorimetry***2005**, *81*, 395–398.

(209) In, K. *Turkish Journal of Engineering and Environmental Sciences***2004**, *28*, 233–239.

(210) Friedman, H. L. *Journal of Polymer Science Part C: Polymer Symposia***1964**, *6*, 183–195.

(211) Nam, J.; Seferis, J. C. *Journal of Polymer Science Part B: Polymer Physics***1991**, *29*, 601–608.

(212) Lv, L.; Sun, P.; Gu, Z.; Du, H.; Pang, X.; Tao, X.; Xu, R.; Xu, L. *Journal of Hazardous Materials***2009**, *161*, 1444–1449.

(213) Dinnebier, R. E.; Billinge, S. J. L. *Powder Diffraction: Theory and Practice*; Royal Society of Chemistry, 2008; p. 532.

(214) Lonardelli, I.; Wenk, H. R.; Lutterotti, L.; Goodwin, M. *Journal of Synchrotron Radiation***2005**, *12*, 354–60.

(215) Toby, B. H. *Powder Diffraction***2012**, *21*, 67–70.

(216) Paul, K. W.; Borda, M. J.; Kubicki, J. D.; Sparks, D. L. *Langmuir : the ACS journal of surfaces and colloids***2005**, *21*, 11071–8.

(217) Rosenthal, M. R. *Journal of Chemical Education***1973**, *50*, 331.

(218) Addison, C. C.; Logan, N.; Wallwork, S. C.; Garner, C. D. *Quarterly Reviews, Chemical Society***1971**, *25*, 289–322.

(219)   Curtis, N. F.; Curtis, Y. M. *Inorganic Chemistry***1965**, *4*, 804–809.

(220)   Faure, C.; Borthomieu, Y.; Delmas, C.; Fouassier, M. *Journal of Power Sources***1991**, *36*, 113–125.

(221)   Elkhattabi, E. H.; Lakraimi, M.; Badreddine, M.; Legrouri, A.; Cherkaoui, O.; Berraho, M. *Applied Water Science***2013**, *3*, 431–438.

(222)   Liu, Z.; Ma, R.; Osada, M.; Iyi, N.; Ebina, Y.; Takada, K.; Sasaki, T. *Journal of the American Chemical Society***2006**, *128*, 4872–80.

(223)   Majoni, S.; Hossenlopp, J. *Polymer Degradation and Stability***2010**, *95*, 1593–1604.

(224)   Thomas, G.; Kamath, P. V. *Journal of Chemical Sciences***2006**, *118*, 127–133.

(225)   Kodama, T.; Harada, Y.; Ueda, M.; Shimizu, K.; Shuto, K.; Komarneni, S. *Langmuir***2001**, *17*, 4881–4886.

(226)   Kovář, P.; Pospíšil, M.; Nocchetti, M.; Čapková, P.; Melánová, K. *Journal of Molecular Modeling***2007**, *13*, 937–942.

(227)   Kalinichev, A. G.; Padma Kumar, P.; James Kirkpatrick, R. *Philosophical Magazine***2010**, *90*, 2475–2488.

(228)   Miyata, S. *Clays and Clay Minerals***1983**, *31*, 305–311.

(229)   Lv, L.; He, J.; Wei, M.; Duan, X. *Industrial & Engineering Chemistry Research***2006**, *45*, 8623–8628.

(230)   Lee, I.-H.; Kuan, Y.-C.; Chern, J.-M. *Journal of the Chinese Institute of Chemical Engineers***2007**, *38*, 71–84.

(231)   Markov, L.; Ioncheva, R.; Marinov, M.; Ivanov, K. *Materials Chemistry and Physics***1990**, *26*, 493–504.

(232)   Xu, R.; Zeng, H. C. *Journal of Physical Chemistry B***2003**, *107*, 12643–12649.

(233)   Ding, Y.; Zhang, G.; Zhang, S.; Huang, X.; Yu, W.; Qian, Y. *Chemistry of Materials***2000**, *12*, 2845–2852.

(234)   Cucos, A.; Budrugeac, P. *Journal of Thermal Analysis and Calorimetry***2013**, 1–9.

(235)   Cai, X. E.; Shen, H. *Journal of Thermal Analysis and Calorimetry***1999**, *55*, 67–76.

(236) Hsieh, Y.-C. *Aerosol and Air Quality Research* **2010**, 212–218.

(237) Yuvaraj, S.; Fan-Yuan, L.; Tsong-Huei, C.; Chuin-Tih, Y. *The Journal of Physical Chemistry B* **2003**, *107*, 1044–1047.

(238) Lv, L.; He, J.; Wei, M.; Evans, D. G.; Duan, X. *Water Research* **2006**, *40*, 735–743.

(239) Sharma, Y. C.; Srivastava, V.; Weng, C. H.; Upadhyay, S. N. *The Canadian Journal of Chemical Engineering* **2009**, *87*, 921–929.

(240) Ai, L.; Zhang, C.; Meng, L. *Journal of Chemical and Engineering data* **2011**, *56*, 4217–4225.

(241) Venkateswaran, V.; Priya, V. T. *Journal of Applied Technology in Environmental Sanitation* **2012**, *2*, 7–16.

(242) Kandare, E.; Hossenlopp, J. M. *Inorganic Chemistry* **2006**, *45*, 3766–73.

(243) Ulibarri, M.-A.; Labajos, F. M.; Rives, V.; Trujillano, R.; Kagunya, W.; Jones, W. *Inorganic Chemistry* **1994**, *33*, 2592–2599.

(244) Erickson, K. L.; Bostrom, T. E.; Frost, R. L. *Materials Letters* **2005**, *59*, 226–229.

(245) Hussein, M. Z. Bin; Ghotbi, M. Y.; Yahaya, A. H.; Abd Rahman, M. Z. *Materials Chemistry and Physics* **2009**, *113*, 491–496.

(246) Fetter, G.; Ramos, E.; Olguin, M. T.; Bosch, P.; Bulbulian, S. *Journal of Radioanalytical and Nuclear Chemistry* **1997**, *221*, 63–66.

(247) Chen, Y.; Wang, K.; Lou, L. *Journal of Photochemistry and Photobiology A: Chemistry* **2004**, *163*, 281–287.

(248) Theriault, E. J.; McNamee, P. D. *Industrial & Engineering Chemistry* **1936**, *28*, 79–82.

(249) Tian, Y.; Wu, M.; Lin, X.; Huang, P.; Huang, Y. *Journal of Hazardous Materials* **2011**, *193*, 10–16.

(250) Namasivayam, C.; Prabha, D.; Kumutha, M. *Bioresource Technology* **1998**, *64*, 77–79.

(251) Mondal, M.; Singh, R.; Kumar, A.; Prasad, B. *Korean Journal of Chemical Engineering* **2011**, *28*, 1386–1392.

(252) Hower, W. F. *Clays and Clay Minerals* **1970**, *18*, 97–105.

(253) Arbuznikov, A.; Vasilyev, V.; Goursot, A. *Surface Science***1998**, *397*, 395–405.

(254) Al-Qunaibit, M. H.; Mekhemer, W. K.; Zaghloul, A. A. *Journal of Colloid and Interface Science***2005**, *283*, 316–21.

(255) Kaolin, G. *Clays and Clay Minerals***1970**, *18*, 37–46.

(256) Fan, H. J.; Yang, Y.; Zacharias, M. *Journal of Materials Chemistry***2009**, *19*, 885–900.

(257) Francke, L.; Durand, E.; Demourgues, A.; Vimont, A.; Daturi, M.; Tressaud, A. *Journal of Materials Chemistry***2003**, *13*, 2330.

(258) Lennie, A. R.; Vaughan, D. J. *American Mineralogist***1992**, *77*, 1166–1171.

(259) Thomas, G. S.; Kamath, P. V. *Solid State Sciences***2006**, *8*, 1181–1186.

(260) Omata, T.; Ueda, N.; Ueda, K.; Kawazoe, H. *Applied Physics Letters***1994**, *64*, 1077–1078.

(261) Hsieh, I. J.; Feng, M. S.; Kuo, K. T.; Lin, P. *Journal of The Electrochemical Society***1994**, *141*, 1617–1621.

(262) Holland, J. S. The Plight of the Honeybee. *National Geographic***2103**.

(263) Walsh, B. Beepocalypse Redux: Honeybees Are Still Dying — and We Still Don't Know Why. *Science and Space***2013**.

9.0   Appendices

A1.   Plot of ln(t$_\alpha$) against 1/T for the determination of isoconversional energy corresponding to Ac, ClAc, dClAc and tClAc intercalation (solid).
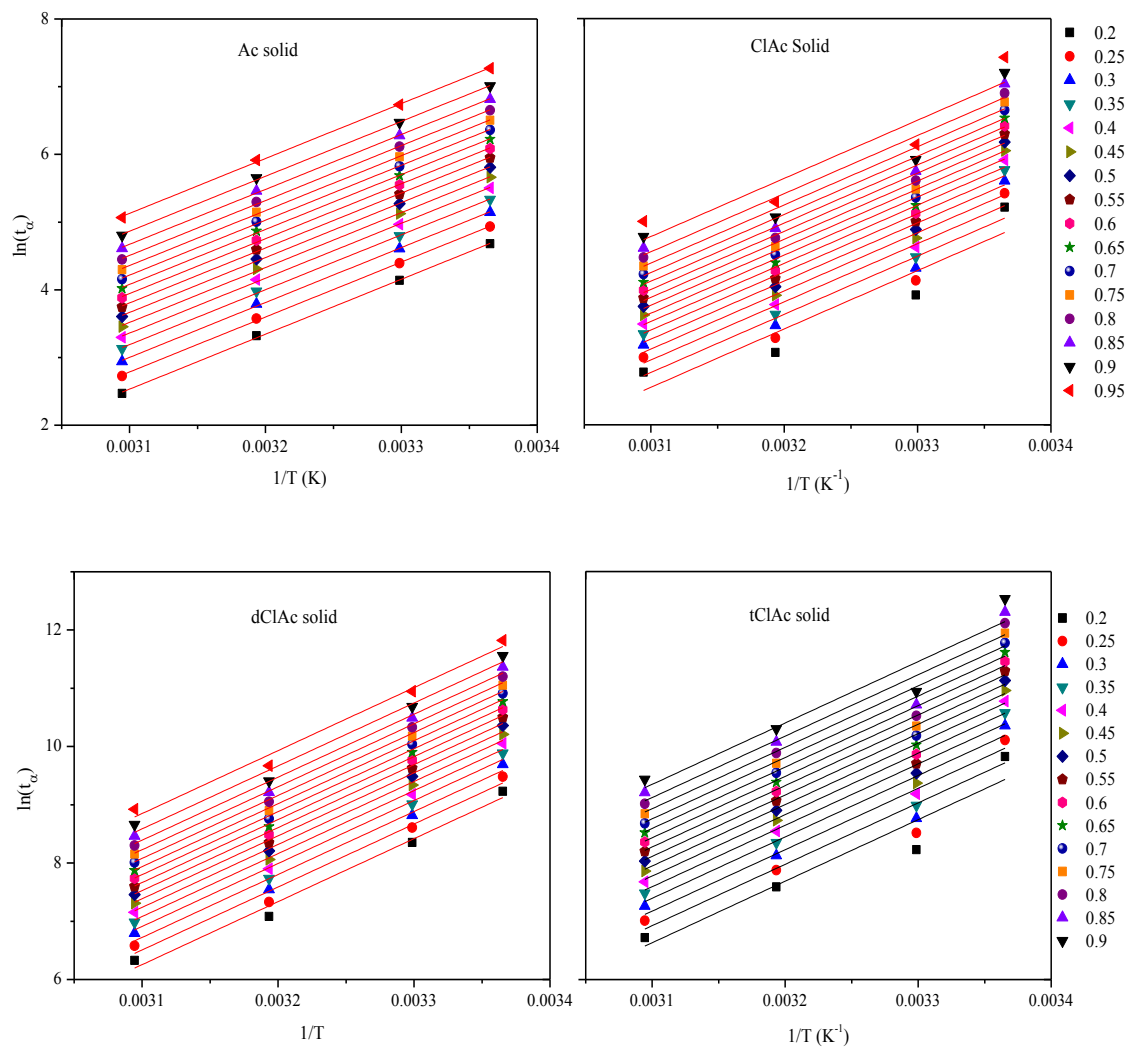
A2.   Plot of ln(t$_\alpha$) against 1/T for the determination of isoconversional energy corresponding to Ac, ClAc, dClAc and tClAc intercalation (solution).
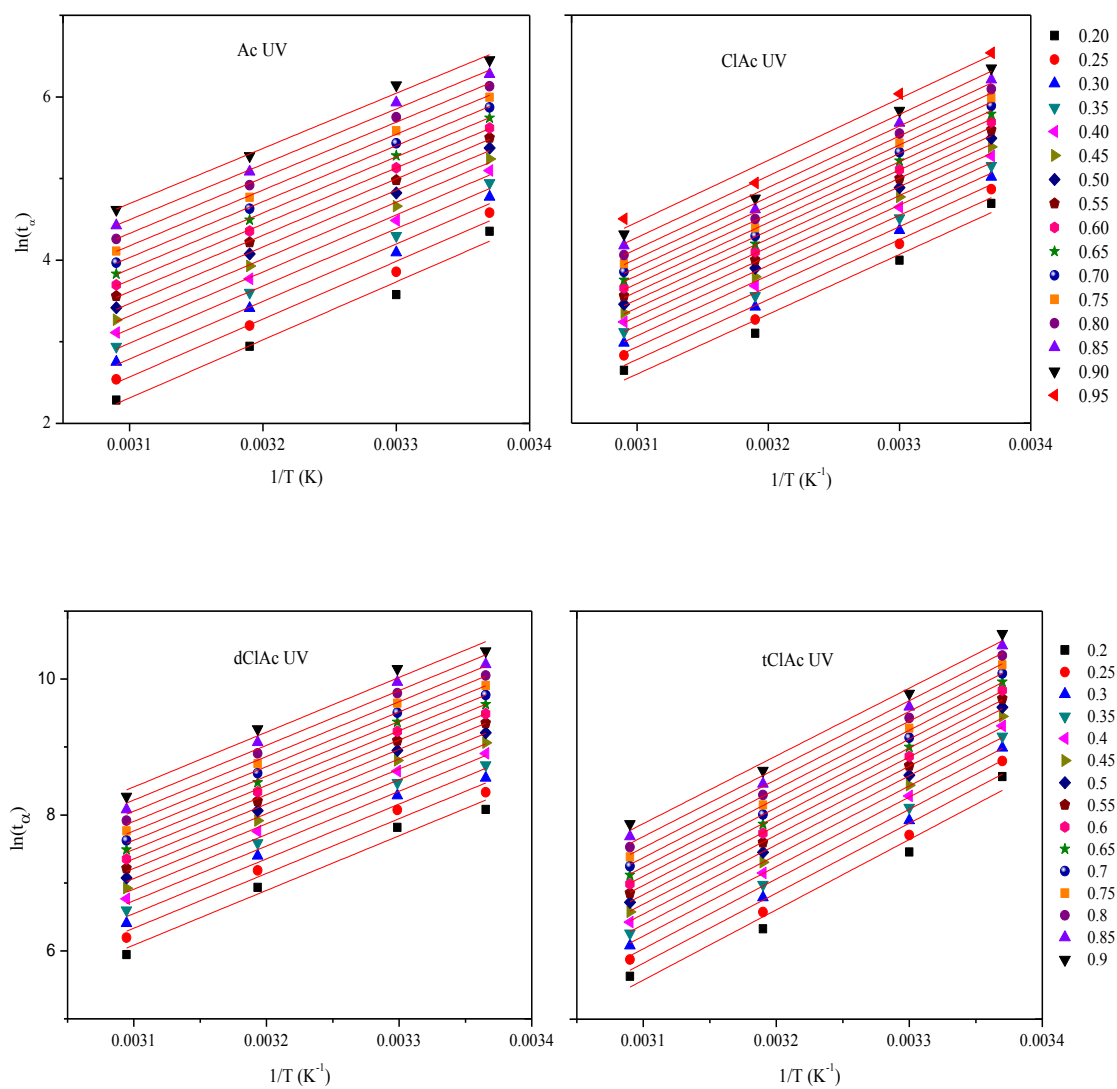
A3. E_{iso} dependence on α for the solution phase transformations due to tClAc and dClAc, ClAc and Ac intercalation.
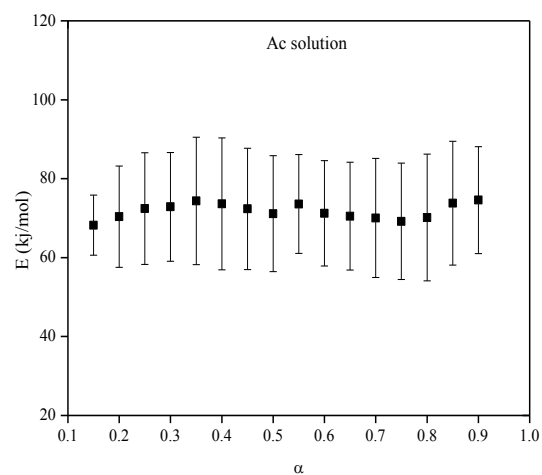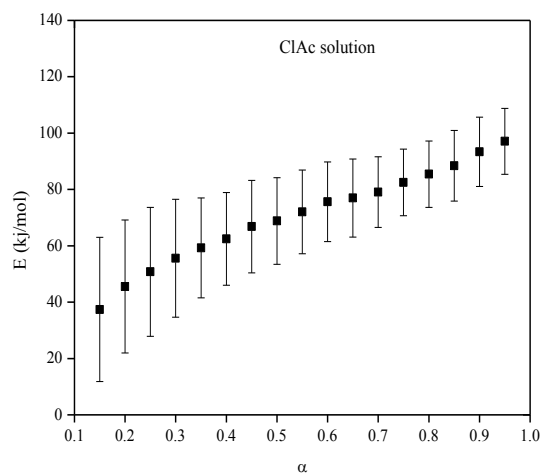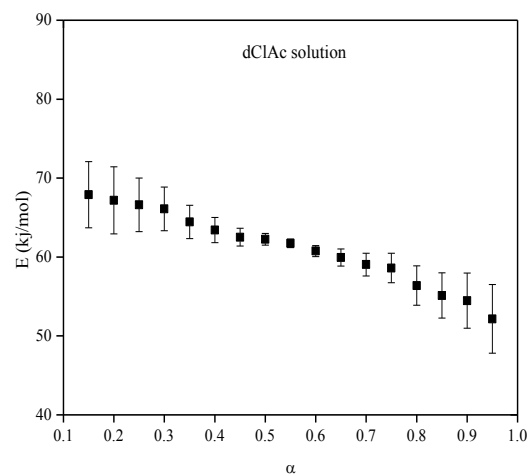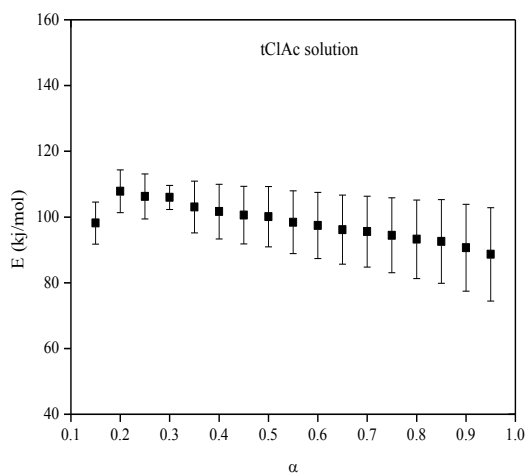
A4. E_{iso} dependence on α for the solid phase changes due to tClAc, dClAc, ClAc and Ac intercalation
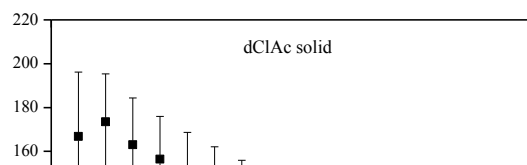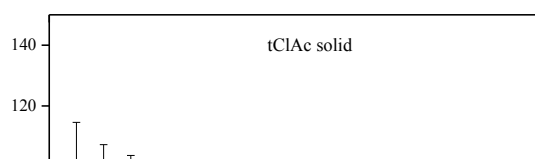
A5.   Extent of reaction plot as function of time (s) for the transformation of the solid phase upon intercalation of Ac (A), ClAc (B), dClAc (C) and tClAc (D) at 24 °C, 30 °C, 40 °C, and 50 °C; and their corresponding double-logarithmic plots (inserts).
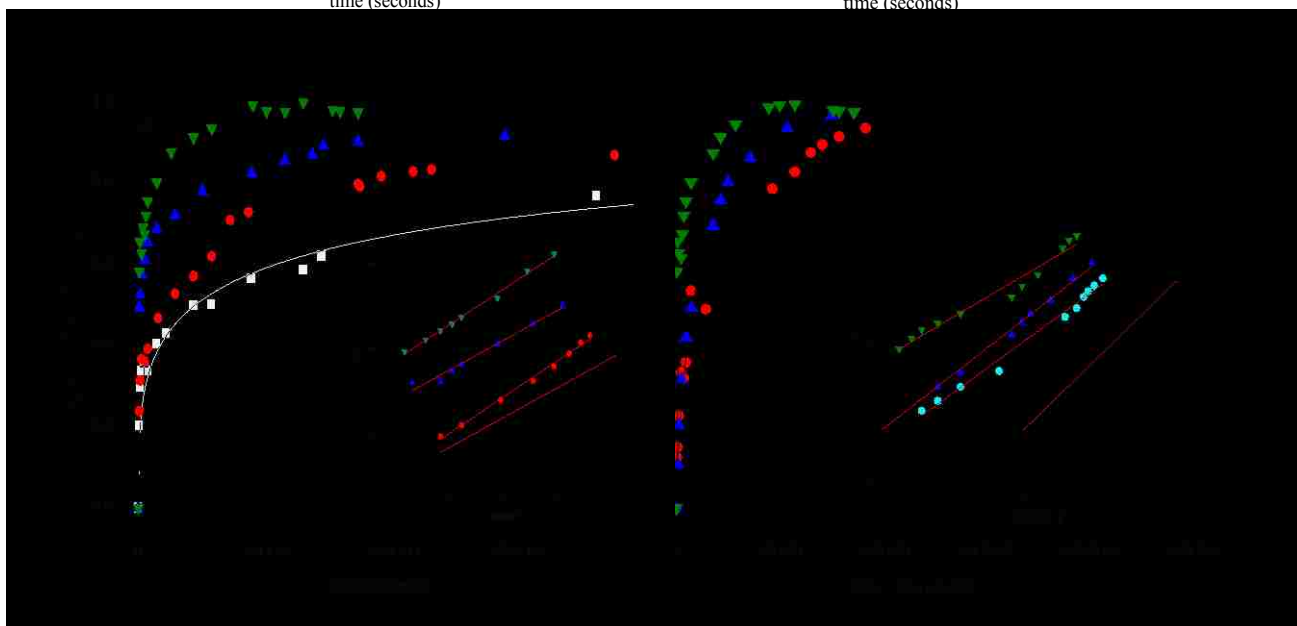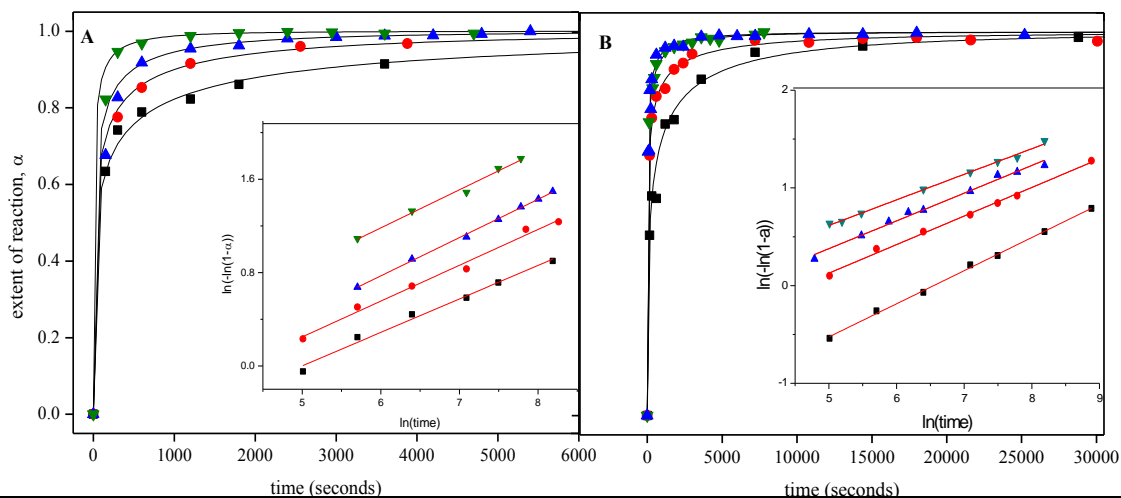
A6. Extent of reaction plot as function of time (s) for the nitrate concentration change upon intercalation of Ac (A) ClAc (B) dClAc (C) and tClAc (D) at 24 $^{\circ}$C, 30 $^{\circ}$C, 40 $^{\circ}$C, and 50 $^{\circ}$C; and their corresponding double-logarithmic plots (inserts).
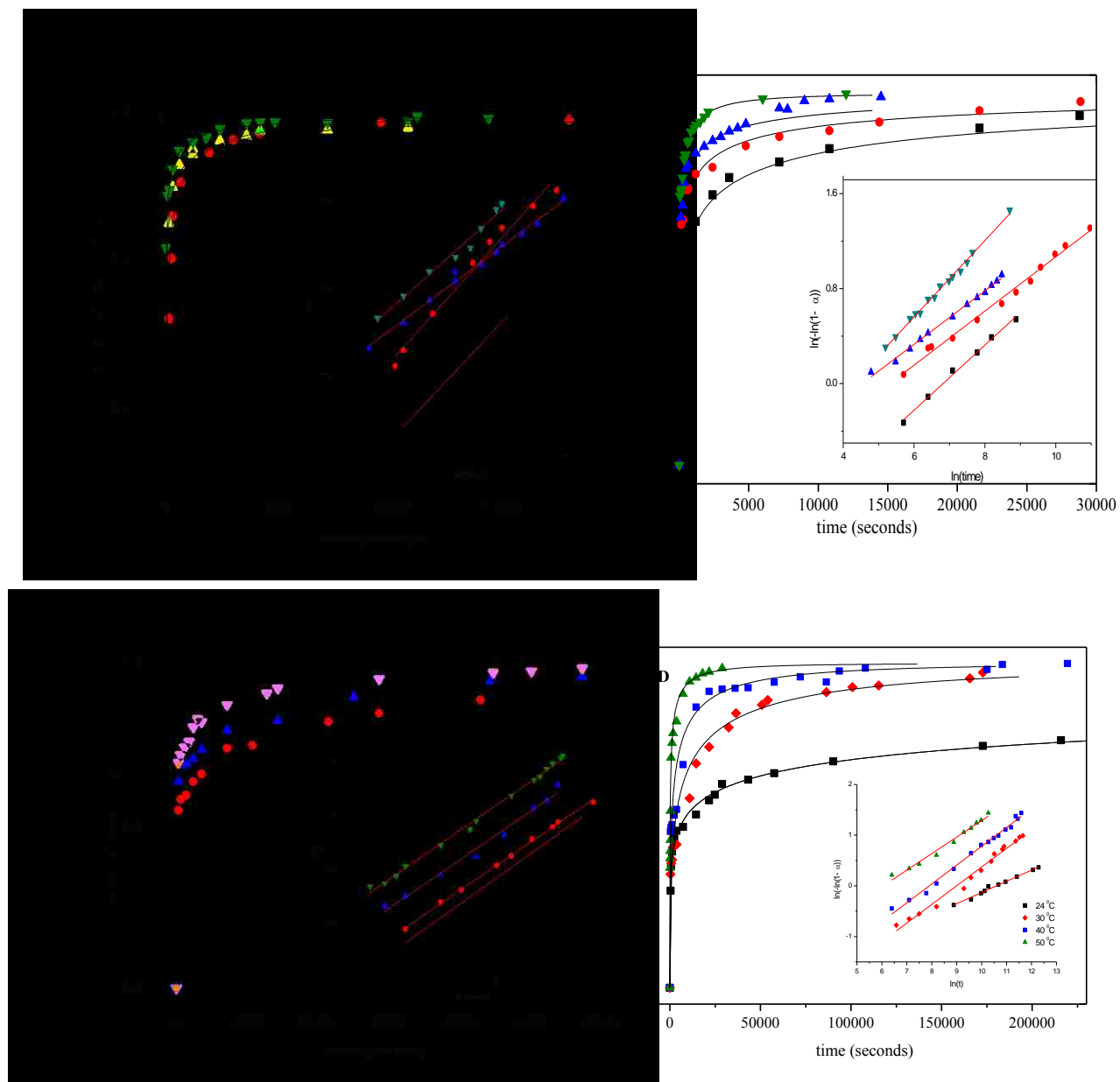
A7. Plot of ln(k) against 1/T for the determination of Arrhenius energy for Ac and ClAc (left) and dClAc and tClAc(right) for both solid and liquid phases.
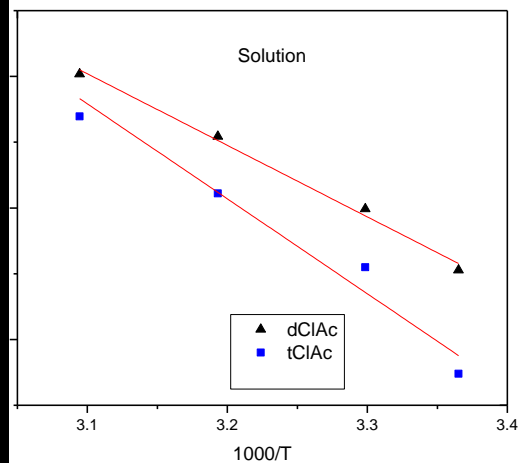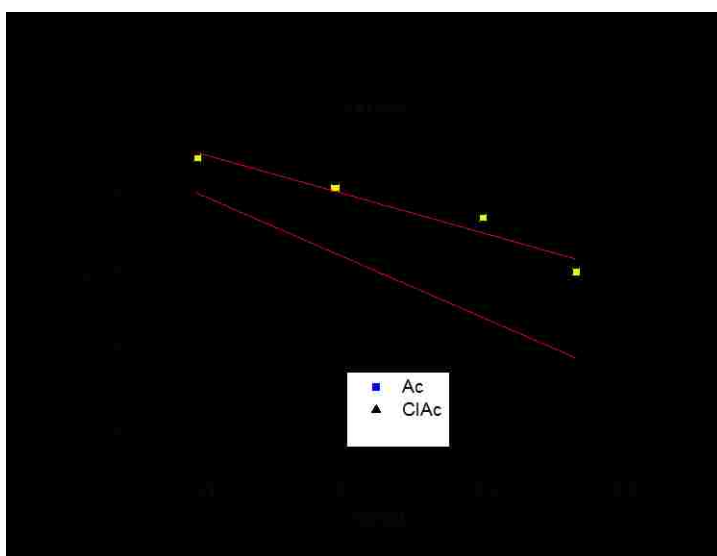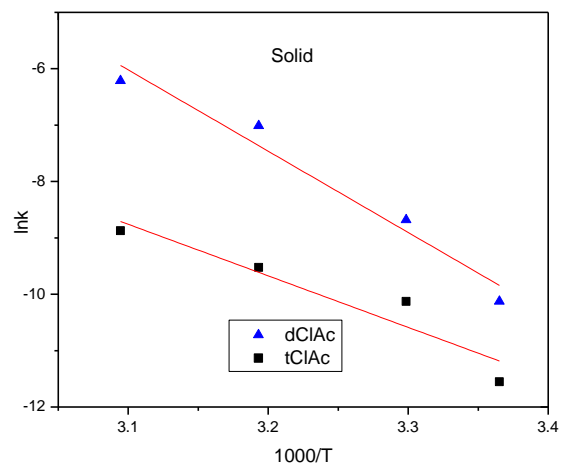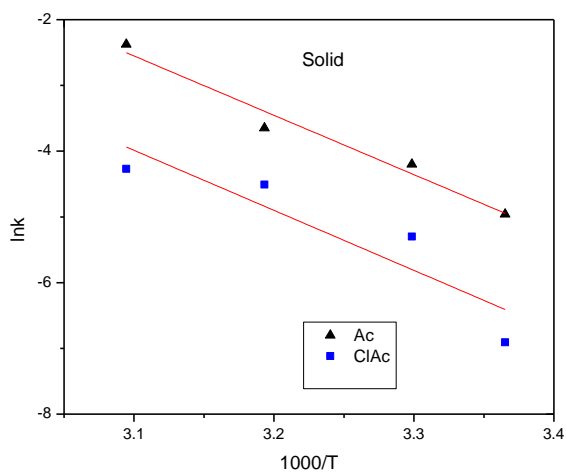
B1. Calibration curves used for analysis of Zn and Cu in the three HDSs (ZnHAc, ZnCuHAc and CuHAc) using AAS, and also the curve used for acetate analysis using HPLC.
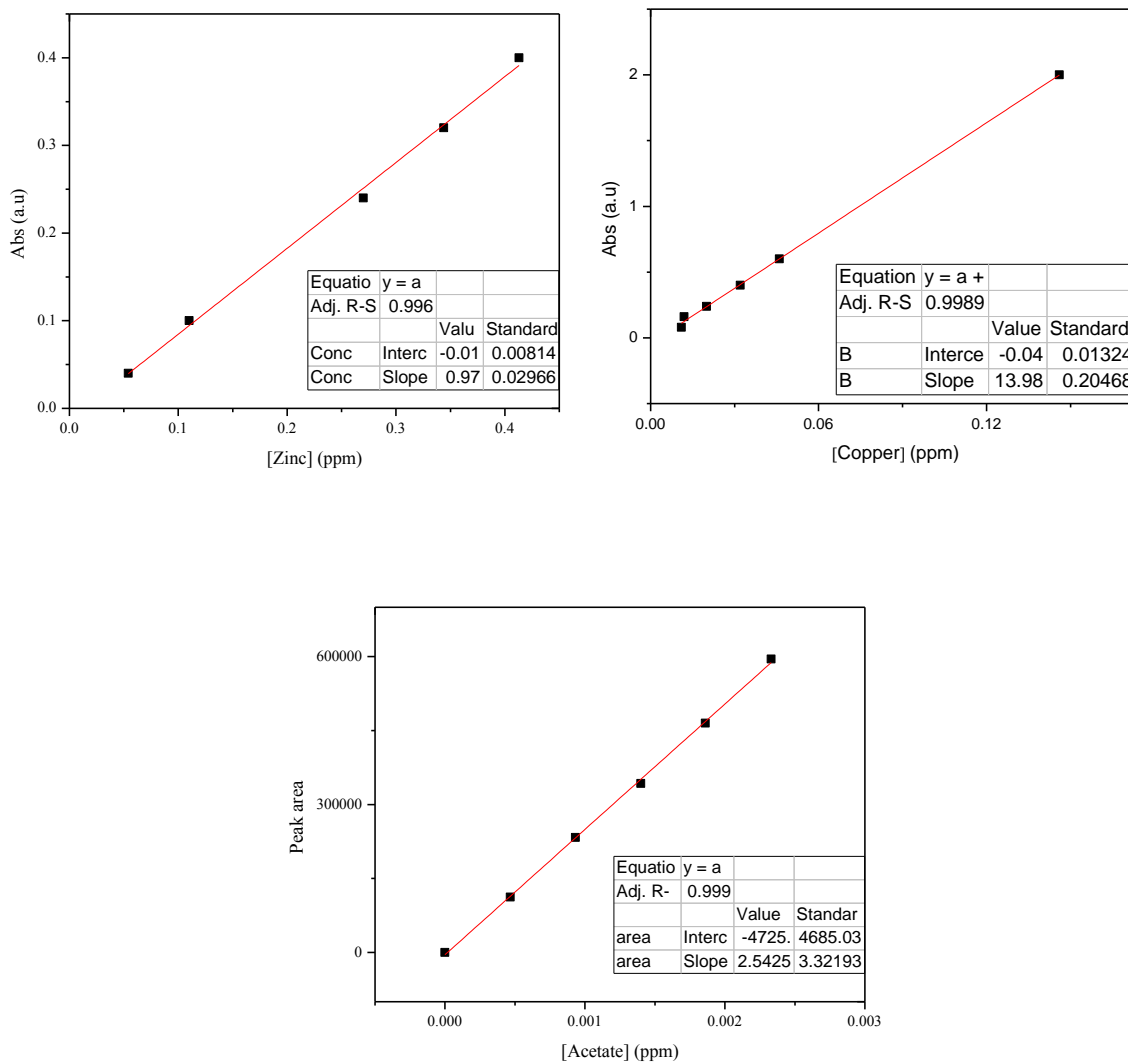
B2. TG-DSC data for the degradation of CuHAc (left), ZnHAc (right) and ZnCuHAc (bottom) in nitrogen at 20 °C/min.
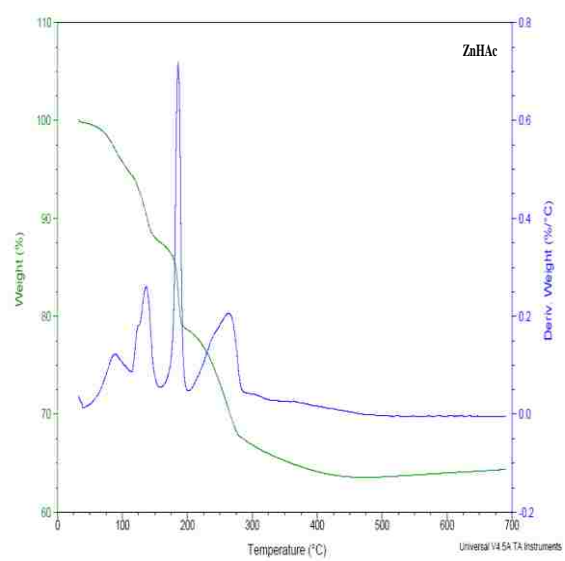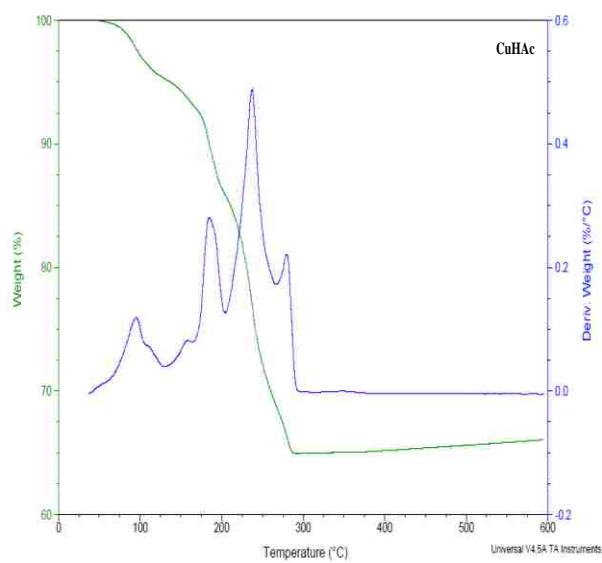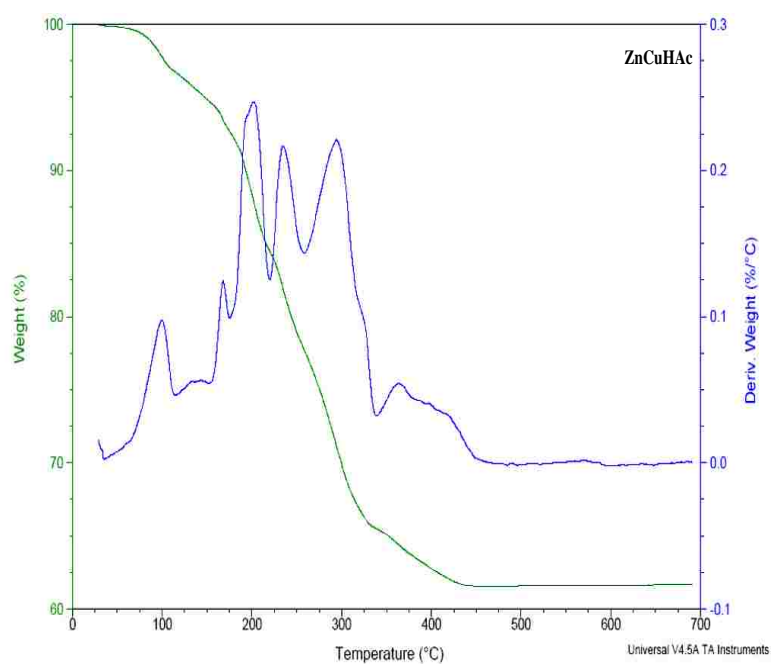
B3 Double-logarithm plots of the solution and solid phase data for ZnCuHAc and ZnHAc.
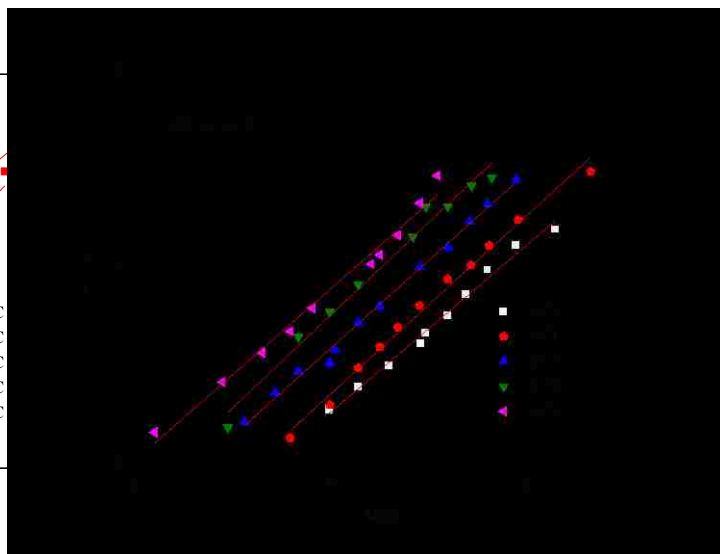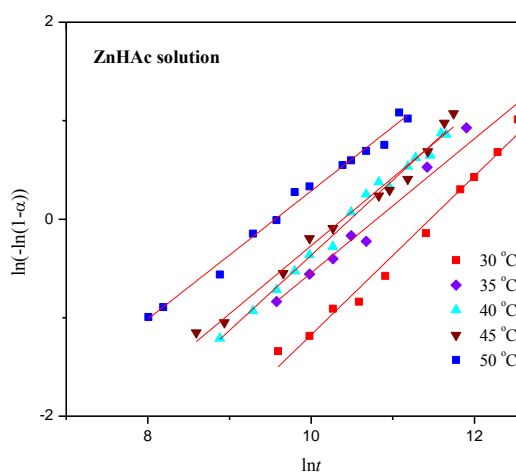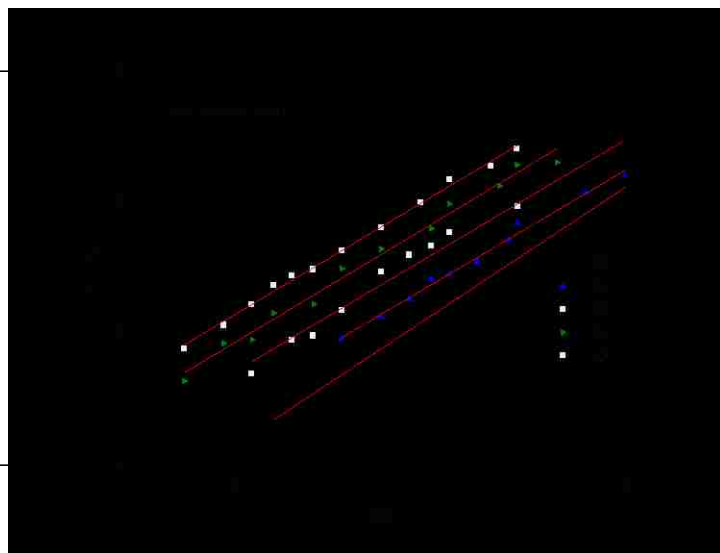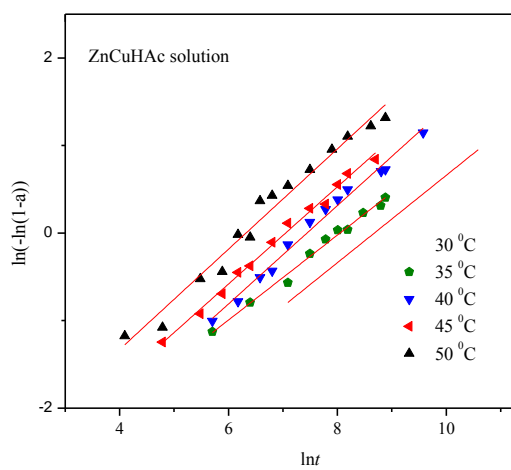
B4   Double-logarithm plots of the solution and solid phase data for CuHAc.
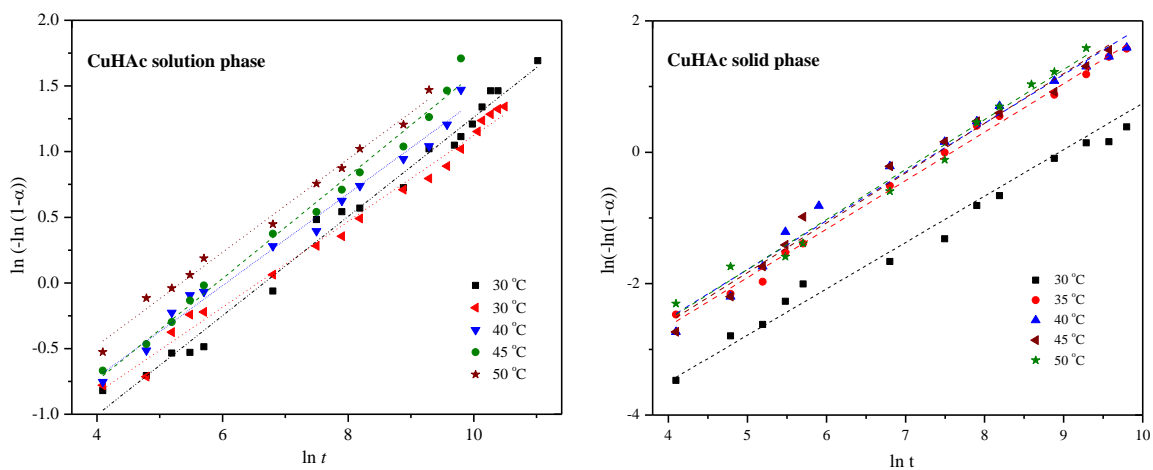
B5 Plots of lnk against 1/T, for the derivation of activation energy using the Arrhenius equation.
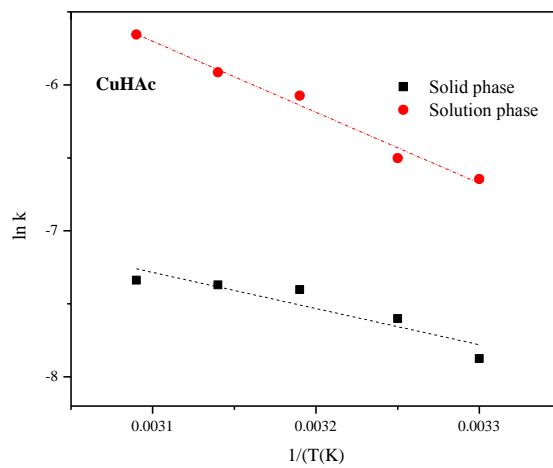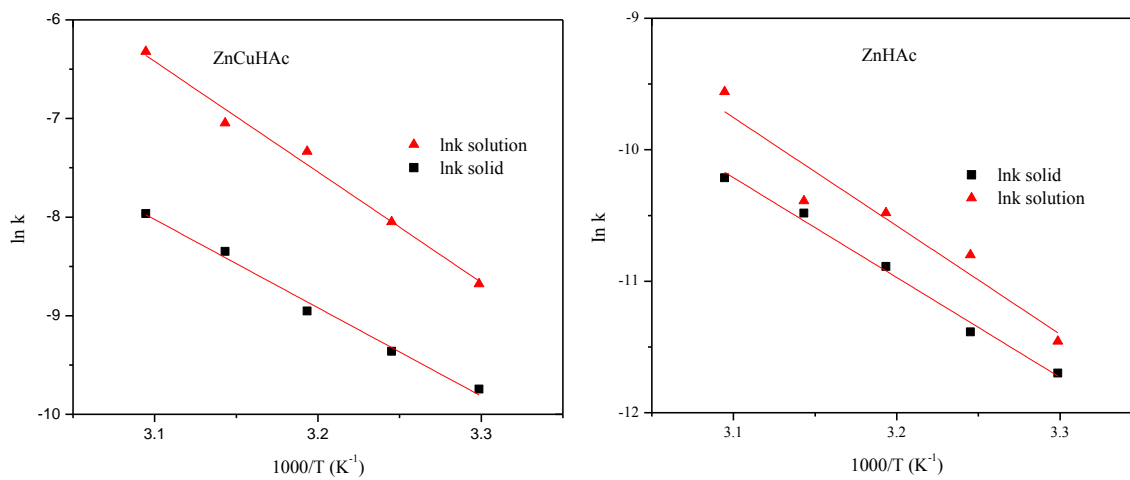
C1: Acetate: freq rb3lyp/6-311+g scrf=(iefpcm,solvent=water) geom=connectivity

Atomic charges with hydrogens summed into heavy atoms:

1 C   0.014984
 2 H   0.000000
 3 H   0.000000
 4 H   0.000000
 5 C   0.298657
 6 O -0.664865
 7 O -0.648776

Electronic spatial extent (au): **<R**2>= 262.7011**
Charge=   -1.0000 electrons

		1			2			3	
		A			A			A	
Frequencies --		18.4535			460.7247			615.5007	
Red. masses --		1.0834			3.1718			2.7176	
Frc consts --		0.0002			0.3967			0.6066	
IR Inten --		0.1865			10.3765			12.8514	
Atom AN	X	Y	Z	X	Y	Z	X	Y	Z
1 6	0.00	0.00	0.00	0.01	0.20	0.00	0.01	0.00	-0.02
2 1	0.00	0.00	0.54	-0.49	0.38	0.00	0.01	0.00	0.36
3 1	0.04	-0.50	-0.32	0.26	0.40	0.01	-0.55	-0.06	0.20
4 1	-0.04	0.50	-0.31	0.26	0.40	-0.01	0.58	0.06	0.20
5 6	0.00	0.00	0.02	0.01	-0.15	0.00	0.00	0.00	-0.35
6 8	0.00	0.00	0.04	-0.22	-0.06	0.00	-0.01	0.01	0.12
7 8	0.00	0.00	-0.05	0.21	-0.06	0.00	-0.01	-0.01	0.11

		4			5			6	
		A			AA				
Frequencies --		622.1560			889.5979			1038.2459	
Red. masses --		6.6725			7.3541			1.5028	
Frcconsts --		1.5217			3.4290			0.9544	
IR Inten --		37.0651			5.5565			86.5149	
Atom AN	X	Y	Z	X	Y	Z	X	Y	Z
1 6	0.42	-0.01	0.00	-0.38	0.01	0.00	0.01	0.17	0.00
2 1	0.44	-0.01	-0.02	-0.36	-0.02	0.00	0.75	-0.11	0.00
3 1	0.47	0.01	0.00	-0.44	-0.04	-0.02	-0.36	-0.23	-0.07
4 1	0.40	0.00	-0.02	-0.44	-0.04	0.02	-0.36	-0.23	0.07
5 6	0.14	0.01	0.02	0.27	0.01	0.00	0.00	0.04	0.00
6 8	-0.24	0.23	-0.01	0.06	0.35	0.00	-0.05	-0.06	0.00
7 8	-0.26	-0.23	-0.01	0.10	-0.36	0.00	0.05	-0.05	0.00

		7			8			9	
		A			AA				
Frequencies --		1080.7945			1330.7980			1413.7670	
Red. masses --		1.7342			9.8004			1.9500	
Frcconsts --		1.1936			10.2262			2.2964	
IR Inten --		8.7197			333.7092			612.1699	
Atom AN	X	Y	Z	X	Y	Z	X	Y	Z
1 6	0.00	0.00	0.16	-0.13	0.00	0.00	0.12	-0.06	0.00
2 1	0.00	0.00	-0.34	-0.36	0.05	0.00	-0.48	0.16	0.00
3 1	0.62	-0.06	-0.17	-0.25	-0.10	-0.02	-0.44	0.14	0.34
4 1	-0.62	0.07	-0.17	-0.25	-0.10	0.02	-0.44	0.15	-0.34
5 6	0.00	0.00	-0.19	0.72	0.03	0.00	-0.02	0.22	0.00
6 8	0.00	0.00	0.03	-0.19	-0.25	0.00	-0.03	-0.07	0.00
7 8	0.00	0.00	0.03	-0.20	0.24	0.00	0.04	-0.08	0.00

		10			11			12	
		A			AA				
Frequencies --		1421.4219			1510.4888			1511.5689	
Red. masses --		2.0709			1.1278			1.0483	
Frcconsts --		2.4652			1.5161			1.4112	
IR Inten --		579.0662			53.7316			14.0699	
Atom AN	X	Y	Z	X	Y	Z	X	Y	Z
1 6	-0.13	-0.06	0.00	-0.02	-0.04	0.00	0.00	0.00	-0.06
2 1	0.40	-0.22	0.00	0.43	-0.18	-0.05	0.03	-0.01	0.73
3 1	0.53	0.25	-0.09	-0.17	0.46	0.35	0.29	0.40	0.08
4 1	0.53	0.26	0.09	-0.12	0.51	-0.36	-0.31	-0.34	0.03

```
 5  6   0.01  0.24  0.00    0.02 -0.08  0.00    0.00 -0.01 -0.02
 6  8  -0.03 -0.08  0.00    0.00  0.02  0.00    0.00  0.00  0.00
 7  8   0.03 -0.07  0.00   -0.01  0.03  0.00    0.00  0.00  0.00
                    13                 14                 15
                     A                 AA
Frequencies --  3020.6078        3083.6166        3120.1515
 Red. masses --     1.0369           1.0984           1.1008
Frcconsts   --     5.5740           6.1538           6.3140
 IR Inten   --    16.1150          23.5155          37.1927
Atom AN    X    Y    Z      X    Y    Z      X    Y    Z
 1  6  -0.05  0.02  0.00    0.00  0.00  0.09   -0.01 -0.09  0.00
 2  1   0.14  0.42  0.00    0.00  0.00  0.02    0.30  0.85  0.00
 3  1   0.21 -0.30  0.52   -0.25  0.35 -0.56   -0.11  0.13 -0.25
 4  1   0.21 -0.30 -0.52    0.25 -0.35 -0.56   -0.11  0.13  0.25
 5  6   0.00  0.00  0.00    0.00  0.00  0.00    0.00  0.00  0.00
 6  8   0.00  0.00  0.00    0.00  0.00  0.00    0.00  0.00  0.00
```

C2: Chloro acetate: freq rb3lyp/6-311+g scrf=(iefpcm,solvent=water) geom=connectivity
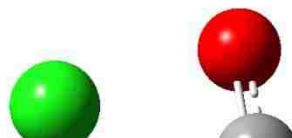
Atomic charges with hydrogens summed into heavy atoms:

1 C -0.064796
2 H   0.000000
3 H   0.000000
4 C   0.217579
5 O -0.604262
6 O -0.573730
7 Cl 0.025209

Sum of Mulliken charges= -1.00000
Electronic spatial extent (au): **<R**2>= 596.1884**
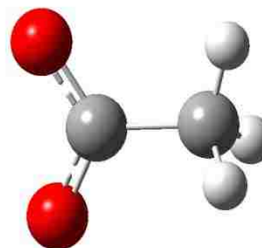Charge=   -1.0000 electrons

	1			2			3		
	A				AA				
Frequencies --	69.6079			222.0076			393.2553		
Red.masses --	3.6811			15.5835			14.5726		
Frcconsts --	0.0105			0.4525			1.3278		
IR Inten --	21.8907			0.6111			1.2269		
Atom AN	X	Y	Z	X	Y	Z	X	Y	Z
1 6	0.01	0.00	0.03	0.20	-0.17	0.02	0.27	0.22	0.02
2 6	0.01	0.04	0.31	0.04	-0.31	0.06	0.09	0.15	-0.07
3 1	0.05	0.41	0.48	0.07	-0.30	0.07	-0.15	-0.09	-0.18
4 1	-0.03	-0.25	0.59	0.09	-0.31	0.06	-0.23	0.27	-0.18
5 8	-0.02	0.00	0.15	0.62	-0.21	-0.04	-0.11	0.28	0.00
6 8	0.04	0.00	-0.24	0.00	0.16	-0.02	0.58	-0.23	0.03
7 17	-0.01	-0.02	-0.10	-0.37	0.20	0.00	-0.33	-0.16	0.02

	4			5			6		
	A				AA				
Frequencies --	565.0566			634.6385			678.6609		
Red. masses --	2.6873			8.1834			6.4523		
Frcconsts --	0.5055			1.9420			1.7509		
IR Inten --	18.8162			175.3932			124.1551		
Atom AN	X	Y	Z	X	Y	Z	X	Y	Z
1 6	-0.01	0.01	0.30	0.18	-0.12	-0.04	-0.12	-0.07	0.17
2 6	-0.02	-0.10	0.10	0.49	-0.10	-0.02	0.27	0.49	-0.02
3 1	0.20	-0.69	-0.18	0.41	-0.04	0.02	0.30	0.12	-0.20
4 1	-0.16	0.38	-0.38	0.45	-0.26	0.12	0.13	0.61	-0.14
5 8	-0.05	0.03	-0.11	-0.33	-0.07	-0.02	0.16	-0.11	-0.04
6 8	0.02	0.03	-0.11	-0.06	0.35	0.02	-0.16	-0.08	-0.07
7 17	0.02	0.01	-0.02	-0.08	-0.05	0.01	-0.06	-0.08	0.01

	7			8			9		
	A				AA				
Frequencies --	895.2255			941.4949			1184.0051		
Red. masses --	7.2861			1.9890			1.1030		
Frcconsts --	3.4404			1.0388			0.9111		
IR Inten --	0.1968			8.4757			5.7957		
Atom AN	X	Y	Z	X	Y	Z	X	Y	Z
1 6	-0.23	0.15	-0.01	-0.01	-0.01	0.21	-0.02	-0.01	0.08
2 6	0.33	-0.26	-0.01	-0.03	-0.02	-0.19	0.00	0.00	-0.03
3 1	0.42	-0.12	0.06	0.24	0.64	0.10	-0.69	0.04	0.04
4 1	0.34	-0.43	0.13	-0.25	-0.53	0.31	0.71	-0.04	0.03
5 8	0.11	0.36	0.02	0.00	-0.01	-0.04	0.00	0.01	-0.01
6 8	-0.19	-0.23	-0.03	0.03	0.01	-0.04	0.01	0.01	-0.01
7 17	-0.02	-0.01	0.01	0.00	0.00	0.02	0.00	0.00	-0.01

	10			11			12		
	A				AA				
Frequencies --	1268.3007			1320.1654			1445.1105		
Red. masses --	1.4620			4.0675			1.2631		
Frcconsts --	1.3856			4.1767			1.5541		
IR Inten --	294.9450			210.9956			207.5757		
Atom AN	X	Y	Z	X	Y	Z	X	Y	Z
1 6	-0.13	0.02	-0.03	0.36	-0.15	0.03	0.03	0.09	0.01
2 6	-0.08	-0.01	0.01	-0.18	0.04	-0.01	0.03	-0.09	0.01

```
3  1    0.71  0.06  -0.01     0.54  0.16  0.00    -0.03  0.63  0.32
4  1    0.67  0.06  -0.05     0.63  0.14  -0.08   -0.01  0.47  -0.51
5  8    0.01  -0.03  0.00    -0.02  0.16  0.00     0.00  -0.05  0.00
6  8    0.09  0.04  0.01     -0.18  -0.08  -0.02  -0.02  -0.02  0.00
7  17  -0.01  -0.01  0.00    -0.01  -0.01  0.00    0.00  0.00  0.00
              13                14                15
               A                AA
Frequencies --  1490.6317        3085.3018        3165.4923
 Red. masses --    4.5262          1.0575           1.1095
Frcconsts  --    5.9255          5.9311           6.5501
 IR Inten   --  771.8884          2.6495           0.2149
```

C3: Dichloro acetate:freq rb3lyp/6-311+g scrf=(iefpcm,solvent=water) geom=connectivity

Atomic charges with hydrogens summed into heavy atoms:

```
1 C  -0.040048
2 H   0.000000
3 C   0.062019
4 O  -0.512416
5 O  -0.558363
6 Cl  0.023993
7 Cl  0.024816
```
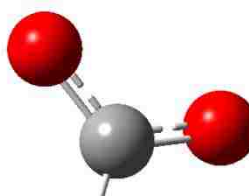
Sum of Mulliken charges= -1.00000
Electronic spatial extent (au): **<R**2>= 886.9113**
Charge= -1.0000 electrons

```
      1              2              3
?A             ?A             ?A
 Frequencies --  24.1633       175.4607       209.7466
Red.masses --   16.8288        21.0603        15.8325
Frcconsts  --   0.0058         0.3820         0.4104
 IR Inten   --   0.4469         3.8523         0.0843
 Raman Activ --  0.0000         0.0000         0.0000
Depolar   --    0.0000         0.0000         0.0000
Atom AN   X    Y    Z      X    Y    Z     X    Y    Z
  1  6   0.00 -0.12 0.00   0.00 -0.29 0.00   0.16 0.00 0.21
  2  1   0.00 -0.25 0.00   0.00 -0.33 0.00   0.38 0.00 0.20
  3  6   0.00 -0.02 0.00   0.00  0.12 0.00   0.31 0.00 0.16
  4  8   0.00  0.69 0.00   0.00  0.34 0.00   0.08 0.00 -0.03
  5  8   0.00 -0.60 0.00   0.00  0.55 0.00   0.65 0.00 0.11
  6 17   0.08  0.01 -0.20  0.39 -0.17 0.08  -0.25 -0.13 -0.09
  7 17  -0.08  0.01 0.20  -0.39 -0.17 -0.08 -0.25 0.13 -0.09
           4              5              6
?A             ?A             ?A
Frequencies -- 256.6263       387.3969       603.6597
 Red. masses -- 20.2904        16.3996        12.1916
Frcconsts  --   0.7873         1.4501         2.6175
 IR Inten   --   0.9504         0.9492       211.8919
 Raman Activ --  0.0000         0.0000         0.0000
Depolar   --    0.0000         0.0000         0.0000
Atom AN   X    Y    Z      X    Y    Z     X    Y    Z
  1  6  -0.12 0.00 0.33  -0.05 0.00 -0.09   0.00 0.79 0.00
  2  1   0.02 0.00 0.34  -0.46 0.00 -0.09   0.00 0.37 0.00
  3  6  -0.10 0.00 0.23   0.28 0.00 -0.20   0.00 0.38 0.00
  4  8  -0.45 0.00 -0.07  0.62 0.00 0.10    0.00 -0.11 0.00
  5  8   0.34 0.00 0.17  -0.05 0.00 -0.18   0.00 -0.13 0.00
  6 17   0.06 0.40 -0.12 -0.16 0.28 0.07    0.09 -0.15 -0.06
  7 17   0.06 -0.40 -0.12 -0.16 -0.28 0.07 -0.09 -0.15 0.06
           7              8              9
?A             ?A             ?A
Frequencies -- 679.9218       717.7715       811.4815
 Red. masses --  9.3963         7.1397        10.1709
Frcconsts  --   2.5593         2.1672         3.9461
 IR Inten   --  58.2707        61.4328        27.2552
 Raman Activ --  0.0000         0.0000         0.0000
Depolar   --    0.0000         0.0000         0.0000
Atom AN   X    Y    Z      X    Y    Z     X    Y    Z
  1  6   0.48 0.00 0.31  -0.30 0.00 0.58    0.00 -0.39 0.00
  2  1   0.49 0.00 0.32  -0.37 0.00 0.60    0.00 -0.44 0.00
  3  6   0.25 0.00 0.00  -0.02 0.00 -0.13   0.00 0.76 0.00
  4  8  -0.04 0.00 -0.35  0.15 0.00 0.02    0.00 -0.18 0.00
  5  8  -0.35 0.00 0.11  -0.06 0.00 -0.13   0.00 -0.18 0.00
  6 17  -0.04 0.03 0.00   0.04 -0.05 -0.06  0.01 0.03 0.02
  7 17  -0.04 -0.03 0.00  0.04 0.05 -0.06  -0.01 0.03 -0.02
          10             11             12
?A             ?A             ?A
```

Frequencies --   849.7815   1190.7248   1262.2001
 Red. masses --   7.6490   1.1964   1.0674
Frcconsts --   3.2544   0.9994   1.0019
 IR Inten   -- 31.2831   35.0198   38.6156
 Raman Activ --   0.0000   0.0000   0.0000
Depolar   --   0.0000   0.0000   0.0000
Atom AN   X   Y   Z   X   Y   Z   X   Y   Z
  1   6   0.43 0.00 0.14   -0.11 0.00 0.00   0.00 -0.06 0.00
  2   1   0.66 0.00 0.15   0.99 0.00 -0.04   0.00 1.00 0.00
  3   6   -0.41 0.00 -0.14   -0.02 0.00 0.00   0.00 0.02 0.00
  4   8   -0.01 0.00 0.24   0.04 0.00 -0.04   0.00 0.00 0.00
  5   8   0.08 0.00 -0.29   -0.01 0.00 0.01   0.00 0.00 0.00
  6 17   -0.03 0.02 0.01   0.00 0.01 0.01   0.00 -0.01 -0.01
  7 17   -0.03 -0.02 0.01   0.00 -0.01 0.01   0.00 -0.01 0.01
                13   14   15
?A   ?A   ?A
Frequencies -- 1325.4142   1746.3259   3191.8667
 Red. masses --   10.9093   11.9649   1.0891
Frcconsts --   11.2915   21.4987   6.5373
 IR Inten   -- 249.9842   527.2573   4.2740
 Raman Activ --   0.0000   0.0000   0.0000
Depolar   --   0.0000   0.0000   0.0000
Atom AN   X   Y   Z   X   Y   Z   X   Y   Z
  1   6   -0.06 0.00 0.00   -0.01 0.00 -0.02   0.00 0.00 -0.09
  2   1   0.49 0.00 -0.03   -0.29 0.00 0.02   0.04 0.00 1.00
  3   6   0.59 0.00 0.12   -0.19 0.00 0.82   0.00 0.00 0.00
  4   8   -0.33 0.00 0.32   0.19 0.00 -0.23   0.00 0.00 0.00
  5   8   -0.11 0.00 -0.42   -0.04 0.00 -0.36   0.00 0.00 0.00
  6 17   0.00 0.00 0.00   0.00 0.00 0.00   0.00 0.00 0.00
  7 17   0.00 0.00 0.00   0.00 0.00 0.00   0.00 0.00 0.00

C4: Trichloro acetate :freq rb3lyp/6-311+g scrf=(iefpcm,solvent=water) geom=connectivity
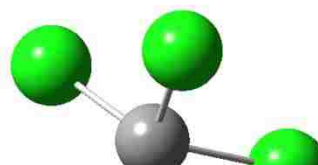
Atomic charges with hydrogens summed into heavy atoms:

1 C   0.536524
  2 C   -0.164107
  3 O   -0.525691
  4 O   -0.472405
  5 Cl -0.161479
  6 Cl -0.051053
  7 Cl -0.161788

Sum of Mulliken charges= -1.00000
Electronic spatial extent (au): **\<R**2\>= 1187.0136**
Charge=   -1.0000 electrons

```
            1                  2                  3
?A                 ?A                 ?A
 Frequencies --   21.3206           174.8098           174.8919
Red.masses --   17.2641            24.6527            24.7157
Frcconsts  --    0.0046             0.4439             0.4454
IR Inten   --    0.2755             2.2556             1.0619
 Raman Activ --   0.0000             0.0000             0.0000
Depolar    --   0.0000             0.0000             0.0000
 Atom AN    X     Y     Z      X     Y     Z      X     Y     Z
 1  6   0.00  0.00  0.05   0.01  0.06 -0.15  -0.01 -0.10 -0.10
 2  6   0.00  0.00 -0.01   0.03 -0.09  0.17  -0.05  0.14  0.11
 3  8   0.00  0.00  0.61   0.22 -0.19  0.51  -0.35  0.31  0.32
 4  8   0.00  0.00 -0.74  -0.17 -0.15  0.27   0.27  0.24  0.17
 5 17  -0.05  0.12 -0.06   0.24  0.15 -0.16   0.46 -0.15  0.05
 6 17   0.00  0.00  0.16   0.24 -0.05 -0.17  -0.39  0.08 -0.11
 7 17   0.05 -0.12 -0.06  -0.52  0.07 -0.03  -0.02 -0.20 -0.17
            4                  5                  6
?A                 ?A                 ?A
Frequencies --  250.2210           258.3347           269.3821
 Red. masses --  18.4637            27.6966            31.9460
Frcconsts  --    0.6811             1.0890             1.3659
IR Inten   --    1.4670             1.1848             0.2484
 Raman Activ --   0.0000             0.0000             0.0000
Depolar    --   0.0000             0.0000             0.0000
Atom AN    X     Y     Z      X     Y     Z      X     Y     Z
 1  6   0.11 -0.05  0.00   0.05  0.25  0.00   0.00  0.00  0.30
 2  6   0.53 -0.06  0.00   0.09  0.14  0.00   0.00  0.00  0.06
 3  8   0.43 -0.03  0.00   0.44 -0.05  0.00   0.00  0.00 -0.17
 4  8   0.57 -0.02  0.00  -0.28  0.03  0.00   0.00  0.00 -0.13
 5 17  -0.20 -0.02 -0.11  -0.12 -0.26  0.39  -0.01  0.46  0.27
 6 17  -0.29  0.10  0.00   0.11  0.40  0.00   0.00  0.00 -0.53
 7 17  -0.20 -0.02  0.11  -0.12 -0.26 -0.39   0.01 -0.46  0.28
            7                  8                  9
?A                 ?A                 ?A
Frequencies --  374.3019           398.8375           624.4360
 Red. masses --  31.4110            18.2261            13.3893
Frcconsts  --    2.5928             1.7082             3.0760
IR Inten   --   12.9983             6.2873           205.2224
 Raman Activ --   0.0000             0.0000             0.0000
Depolar    --   0.0000             0.0000             0.0000
Atom AN    X     Y     Z      X     Y     Z      X     Y     Z
 1  6   0.21 -0.03  0.00   0.02  0.14  0.00   0.00  0.00  0.85
 2  6  -0.23 -0.01  0.00   0.03  0.41  0.00   0.00  0.00  0.43
 3  8  -0.22  0.02  0.00   0.54  0.17  0.00   0.00  0.00 -0.15
 4  8  -0.14 -0.02  0.00  -0.51  0.28  0.00   0.00  0.00 -0.12
 5 17   0.00 -0.27 -0.43   0.08 -0.08 -0.15   0.05 -0.07 -0.14
 6 17   0.16  0.54  0.00  -0.18 -0.23  0.00   0.00  0.00 -0.04
 7 17   0.00 -0.26  0.44   0.08 -0.08  0.15  -0.05  0.07 -0.14
           10                 11                 12
?A                 ?A                 ?A
```

Frequencies --   713.0781   738.9071   771.4069
 Red. masses -- 13.5241   12.6491   12.9708
Frcconsts --   4.0517   4.0690   4.5476
 IR Inten   -- 109.3518   208.1660   106.9012
 Raman Activ --   0.0000   0.0000   0.0000
Depolar   --   0.0000   0.0000   0.0000
Atom AN   X   Y   Z   X   Y   Z   X   Y   Z
  1   6   0.73 -0.05 0.00   0.26 0.90 0.00   0.62 -0.34 0.00
  2   6   0.36 -0.04 0.00 -0.19 -0.11 0.00 -0.56 0.09 0.00
  3   8 -0.21 0.33 0.00 -0.09 -0.14 0.00   0.13 -0.26 0.00
  4   8 -0.28 -0.28 0.00   0.16 -0.01 0.00   0.11 0.28 0.00
  5 17 -0.05 0.02 0.03 -0.01 -0.05 -0.02 -0.04 0.04 0.04
  6 17 -0.05 -0.04 0.00 -0.05 -0.10 0.00 -0.04 -0.01 0.00
  7 17 -0.05 0.02 -0.03 -0.01 -0.05 0.02 -0.04 0.04 -0.04
              13   14   15
?A   ?A   ?A
Frequencies --   814.9394   1290.4114   1804.0921
 Red. masses -- 12.3749   14.6442   12.9522
Frcconsts --   4.8422   14.3672   24.8376
 IR Inten   --   30.8800   324.4109   472.1584
 Raman Activ --   0.0000   0.0000   0.0000
Depolar   --   0.0000   0.0000   0.0000
Atom AN   X   Y   Z   X   Y   Z   X   Y   Z
  1   6   0.00 0.00 -0.48 -0.06 0.00 0.00   0.00 0.01 0.00
  2   6   0.00 0.00 0.83 -0.58 0.05 0.00   0.08 0.87 0.00
  3   8   0.00 0.00 -0.20   0.30 0.49 0.00 -0.16 -0.30 0.00
  4   8   0.00 0.00 -0.21   0.19 -0.54 0.00   0.09 -0.34 0.00
  5 17   0.01 0.00 0.02   0.00 0.00 0.00   0.00 0.00 0.00
  6 17   0.00 0.00 0.02   0.00 0.00 0.00   0.00 -0.01 0.00
  7 17 -0.01 0.00 0.02   0.00 0.00 0.00   0.00 0.00 0.00

C5: NITRATE # optfreq ub3lyp/6-311+g scrf=(iefpcm,solvent=water) geom=connectivity
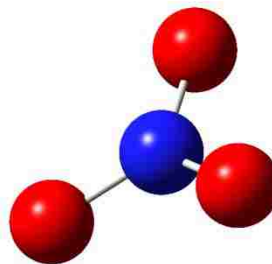
Initial Z matrix
```
N
O          1        B1
O          1        B2    2        A1
O          1        B3    2        A2    3        D1

    B1        1.36000000
    B2        1.36000000
    B3        1.36000000
    A1       109.47125080
    A2       109.47120255
D1          119.99998525
```

APT Atomic charges with hydrogens summed into heavy atoms:

```
1 N    0.318501
  2 O   -0.439500
  3 O   -0.439500
  4 O   -0.439500
```

Sum of Mulliken charges= -1.00000
Electronic spatial extent (au): **<R**2>= 205.0774**
Charge=   -1.0000 electrons

Dipole moment (field-independent basis, Debye):
   X=   0.0000   Y=   0.0003   Z=   0.0023 Tot=   0.0023

and normal coordinates:
```
1                  2                  3
?A                ?A                A1
Frequencies --   653.8016          654.2385          756.4421
 Red. masses --   15.8612           15.8610           14.4084
Frcconsts  --    3.9947            3.9999            4.8576
 IR Inten   --    0.2413            0.2405            14.7432
Atom AN    X     Y     Z      X     Y     Z      X     Y     Z
 1  7   0.00  0.26  0.00  -0.26  0.00  0.00   0.00  0.00  0.89
 2  8   0.00  0.48  0.00   0.63  0.00  0.00   0.00  0.00 -0.26
 3  8   0.48 -0.35  0.00  -0.20 -0.48  0.00   0.00  0.00 -0.26
 4  8  -0.48 -0.35  0.00  -0.20  0.48  0.00   0.00  0.00 -0.26
            4                  5                  6
?A                ?A                ?A
Frequencies --   971.8235          1213.9815         1214.1454
 Red. masses --   15.9949           14.5186           14.5188
Frcconsts  --    8.9003            12.6067           12.6103
 IR Inten   --    0.0006            896.2349          895.2269
Atom AN    X     Y     Z      X     Y     Z      X     Y     Z
1  7   0.00  0.00  0.00   0.00  0.86  0.00   0.86  0.00  0.00
 2  8   0.00 -0.58  0.00   0.00 -0.40  0.00  -0.10  0.00  0.00
 3  8   0.50  0.29  0.00  -0.13 -0.18  0.00  -0.33 -0.13  0.00
 4  8  -0.50  0.29  0.00   0.13 -0.18  0.00  -0.33  0.13  0.00
```

D. 1.0. Search results from the Nicolet TGAlibrary data base.

Tue Apr 23 16:37:48 2013 (GMT-05:00)
SEARCH:
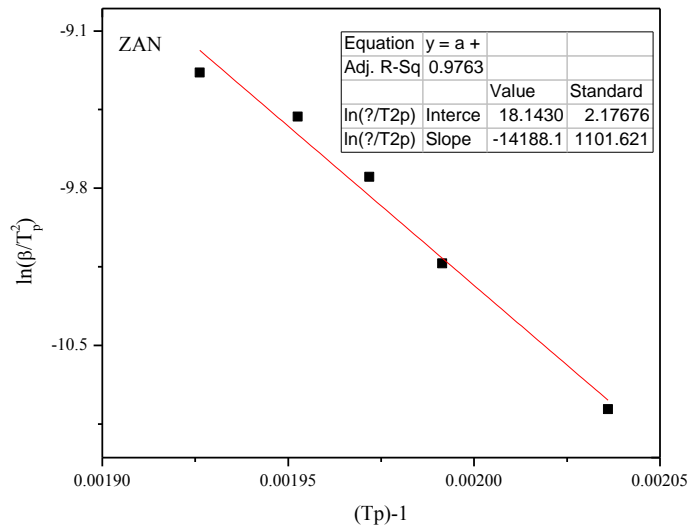   Spectrum: Subtraction Result:**ZnAlN2.1010**
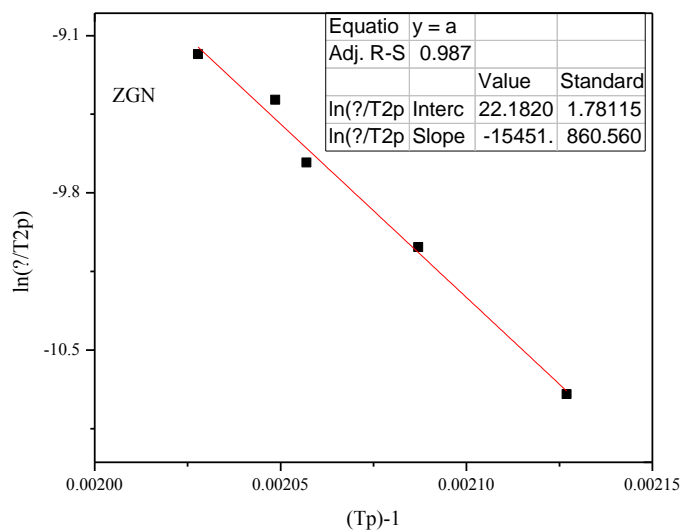   Region: 3495.26-649.91
        Search type: Correlation
        Hit List:

Index	Match	Compound name	Library
452	85.63	Nitrogen dioxide	Nicolet TGA Vapor Phase

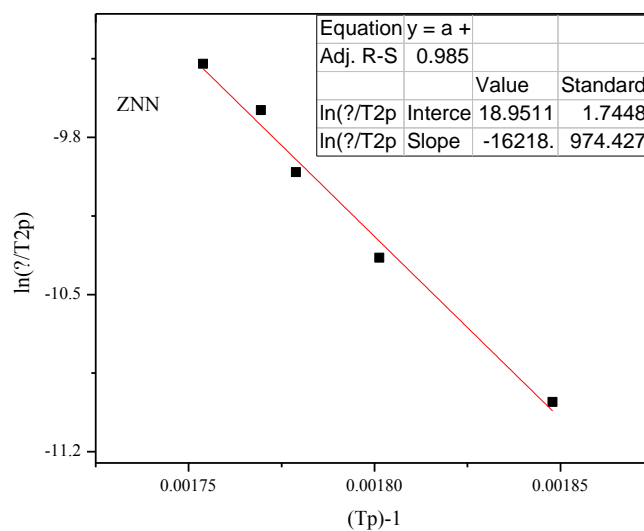**D.2.0.** Plots of $\ln(\beta/T2)$ against $1/T$ for determination of Ea using thermal decomposition of ZAN.
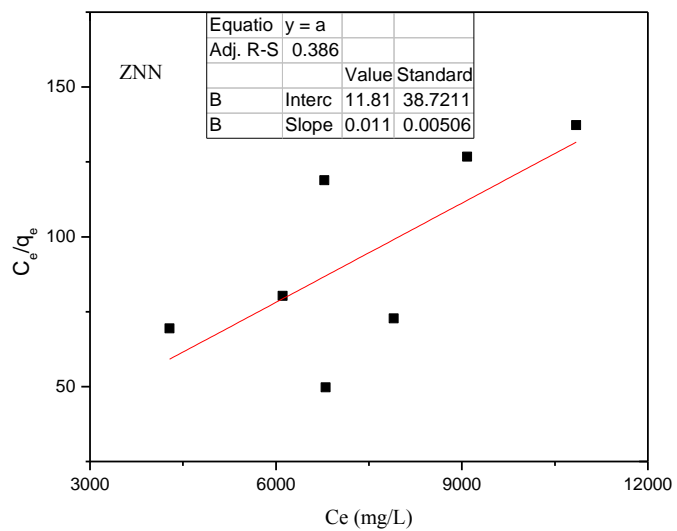
D. 3.0 Plots of ln(β/T2) against 1/T for determination of Ea using thermal decomposition of ZGN

Equatio	y = a		
Adj. R-S	0.987		
		Value	Standard
ln(?/T2p Interc	22.1820	1.78115
ln(?/T2p Slope	-15451.	860.560

ZGN

ln(?/T2p)

(Tp)-1

D. 4.0. Plots of ln(β/T2) against 1/T for determination of Ea using thermal decomposition of ZNN

Equation	y = a +		
Adj. R-S	0.985		
		Value	Standard
ln(?/T2p Interce	18.9511	1.7448
ln(?/T2p Slope	-16218.	974.427

ZNN

ln(?/T2p)

(Tp)-1

D. 5.0. Langmuir plots for tClAc uptake using ZNN.

E. 1.0 Methyl Orange Calibration curve